ISSN 0503-1540

Tome 31 *Mai 1993* Numéro 2

La mer

うみ

1993 年 5 月

日 仏 海 洋 学 会

La Société franco-japonaise
d'océanographie
Tokyo, Japon

Note pour la présentation des manuscrits

La mer, organe de la Société franco-japonaise d'océanographie, publie des articles et notes originaux, des articles de synthèse, des analyses d'ouvrages et des informations intéressant les membres de la société. Les sujets traités doivent avoir un rapport direct avec l'océanographie générale, ainsi qu'avec les sciences halieutiques.

Les manuscrits doivent être présentés avec un double, et dactylographiés, en *double interligne*, et au recto exclusivement, sur du papier blanc de format A4 (21×29,7 cm). Les tableaux et les légendes des figures seront regroupés respectivement sur des feuilles séparées à la fin du manuscrit.

Le manuscrit devra être présenté sous la forme suivante:

1° Il sera écrit en japonais, français ou anglais. Dans le cadre des articles originaux, il comprendra toujours le résumé en anglais ou français de *200 mots* environs. Pour les textes en langues européennes, il faudra joindre en plus le résumé en japonais de *500 lettres* environs. Si le manuscrit est envoyé par un non-japonophone, le comité sera responsable de la rédaction de ce résumé.

2° La présentation des articles devra être la même que dans les numéros récents; le nom de l'auteur précédé du prénom *en entier*, en minuscules; les symboles et abréviations standards autorisés par le comité; les citations bibliographiques seront faites selon le mode de publication: article dans une revue, partie d'un livre, livre entier, etc.

3° Les figures ou dessins originaux devront être parfaitement nettes en vue de la réduction nécessaire. La réduction sera faite dans le format 14,5×20,0 cm.

La première épreuve seule sera envoyée à l'auteur pour la correction.

Les membres de la Société peuvent publier 7 pages imprimées sans frais d'impression dans la mesure à leur manuscrit qui ne demande pas de frais d'impression excessifs (pour des photos couleurs, par exemple). Dans les autres cas, y compris la présentation d'un non-membre, tous les frais seront à la charge de l'auteur.

Cinquante tirés-à-part peuvent être fournis par article aux auteurs à titre gratuit. On peut en fournir aussi un plus grand nombre sur demande, par 50 exemplaires.

Les manuscrits devront être adressés directement au directeur de publication de la Société: M. MURANO, Université des Pêches de Tokyo, Konan 4-5-7, Minato-ku, Tokyo, 108 Japon; ou bien au rédacteur étranger le plus proche: H. J. CECCALDI, EPHE, Station marine d'Endoume, rue Batterie-des-Lions, 13007 Marseille, France; E. D. GOLDBERG, Scripps Institution of Oceanography, La Jolla, California 92093, Etats-Unis; T. ICHIYE, Department of Oceanography, Texas A & M University, College Station, Texas 77843, Etats-Unis; ou T. R. PARSONS, Department of Oceanography, University of British Columbia, Vancouver, B. C. V6T 1W5, Canada.

La mer 31: 49–57, 1993
Société franco-japonaise d'océanographie, Tokyo

Distributions of underwater spectral irradiance and optical environments of tuna fishing grounds in the three oceans*

Tsutomu MORINAGA**, Akihiro IMAZEKI** and Yoshitaka MORIKAWA**

Abstract: During the two winter seasons from 1990 to 1992, the survey of the underwater irradiance was carried on by the R/T Umitaka-maru of Tokyo University of Fisheries, covering the global-scale wide range waters.

By the aid of high-efficiency spectral irradiance meter, the authors measured the irradiance values from the surface to 30m deep for 8 spectral lights of which respective wave length was 443, 481, 513, 554, 599, 664, 683, and 709 nm. Simultaneously with those optical surveys, experimental tuna longlining operations were conducted in the same regional waters.

The underwater spectral light of which wave length is 481nm has the best light transmittance, and that of 709nm has the worst one. So far as the spectral lights of which wave lengths between 443nm and 683nm are concerned, they decrease the values in light transmittance according to the order of wave lengths from the short to the long one. The shorter wave length of 481nm has wider differences in light transmittance than those of the longer one of 709nm. The water mass of the Coral Sea in the Pacific Ocean is the very clean water which comes under the water type IA according to Jerlov's optical classification. In those regions the turbidity does not change with a secular variation. It is common to every fishing ground between 50m and 150m deep and locating from Lat. 20° to 40° N. that the blue light among all the spectral ones is most predominant; that the absolute and relative values of irradiances are in constant ranges of 50 to 320 μw/cm^2, and 0.2 to 1.2%, respectively. This suggests a possibility to use these optical data as a clue for locating the tuna fishing ground.

I. Introduction

Oceanographic observations of underwater spectral irradiance were carried out approximately 40 years ago by JERLOV, Swedish optical-oceanographer, covering a globally wide areas (1951). He measured light transmittances in water by the use of a simple underwater irradiance-meter attached with broad band filters, and, based on the light transmittance distributions for 16 wavelength spectral lights within the spectrum range from 310nm to 700nm, established a classification of such 5 water types as I, IA, IB, II, and III which are arranged in the order of better light transmittances. (1964, 1968) The well-known map that he captioned "Regional Distribution of Optical Water Types" were referred to the various scientific fields. (JERLOV, 1976) MATSUIKE (1973) intended to grasp the solar energy distribution throughout all the space from the sky to the depths of the sea, employing the same type of instrument as that of Jerlov, and measured the underwater spectral irradiance so far in the Kuroshio of the Pacific Ocean, the Indian Ocean, and the Antarctic Ocean. He determined quantitatively seasonal solar energies in the different oceans based on regionally different optical properties of the sea waters in each oceans, and connected those with rough estimates of productivities in the ocean. Thereafter, with the rapid advance of electronic equipments and the substantial progress in

* Received December 8, 1992
** Tokyo University of Fisheries, 5-7 Konan 4-chome, Minato-ku Tokyo, 108 Japan

technologies, a number of high-performance submersible spectroradiometers were developed one after another by many scientists such as TYLER and SMITH (1966), BAUER and IVANOFF (1970), SUGIHARA and INOUE (1976) and OKAMI *et al.*(1981); and the accumulation of data in respect to all the spectral lights was made possible.

Water temperatures, salinities, dissolved oxygen and so far as the environmental elements required for tuna distributions or establishments of tuna fishing grounds have been investigated since quite a long time. (UDA, 1960; KAWAI, 1969; INGHAM, 1977; HANAMOTO, 1985; KURITA *et al.*, 1991) In addition to these elements, optical and audio properties in the water, osmotic pressures, intensitie of magnetic fields can be also considered as the other elements. CAREY *et al.* (1981) report that the movement of the species of boardbill swordfish, *Xiphias galdius* is traced by the use of a bio-telemetry system, finding that this species live in the very deep waters during the daytime and move up in the shallow waters during the nighttime. Thus, it comes to be understood that optical elements in the water are closely related to their distributions and movements as described above. On the other hand, SAKAMOTO (1985) informs that the living sphere of boardbill swordfish is obtained from the locus of their movements mentioned above, and the underwater irradiance values distributed there are trially calculated, finding that the irradiance value in their living depth during the daytime seems to be equal to that during the nighttime. But, there still remains many problems related to the distributions of spectral irradiance and those variations in the different oceanic waters for future studies.

Through the optical observations extended for a two-year period in the three oceans of the world such as the Pacific, the Indian, and the Atlantic Ocean and their adjacent seas, the authors collected the measurements for this study, keeping the identification of instrument, in respect to the irradiance values for 8 different wavelength spectral lights in the waters from the surface to 30m deep. Simultaneously with those optical observations, experimental tuna longlining operations were carried out also in the same regional waters. Based on the collected measurements, such the subjects as (1) the distributions of underwater relative irradiances and spectral light energies in different regional waters, (2) the optical classification of different water masses, and (3) the optical environment of the tuna living sphere are investigated as described hereinafter.

2. Method and Instruments

A series of optical observation was carried out twice–one was in the winter from 13th December 1990 to 3rd March, 1991 (This period will be abbreviated to "in the first period" hereinafter.) and other was also in the winter from 3rd December, 1991 to lst March, 1992 ("in the second period" hereinafter) – during each long-distance cruise of the Umitaka-maru, Research and Training Boat of Tokyo University of Fisheries. Fig. 1 shows the locations of observation stations distributed in different oceans. As seen in Fig. 1 the observation statios count 9 in the first period and 18 in the second period, counting up 27 stations in total. All the stations in the first period lie from east to west in the Pacific, the Atlantic Ocean, and Mediterranean Sea of the northern hemisphere and those in the second period extend from north to south in the Pacific Ocean, the Bay of Bengal in the Indian Ocean, and South China Sea of the both hemispheres. Accordingly, it can be said that distribution of the observation stations covers the global wide-range oceanic waters.

Experimental tuna-longlining operation during the first period were carried on in the offshore water of the Hawaiian Is. in the North Pacific Ocean, and those during the second period were operated in the Bay of Bengal in the Indian Ocean. The positions of those experimental operations are also shown in Fig. 1.

Measurements of underwater irradiance were carried on by the use of the spectral irradiance meter, type SR-8, manifuctured Ishikawa Sangyo Co., Ltd. This meter was incorporated with 8 pieces of built-in interference filters, each of which enables to pass the specific wavelength light among those of 443, 481, 513, 554, 599, 664, 683, and 709nm. Each of the bandpass (50% points) is about 10nm. Besides, the photodiode having an excellent photosensitivity was employed as many as 8 pieces for the light

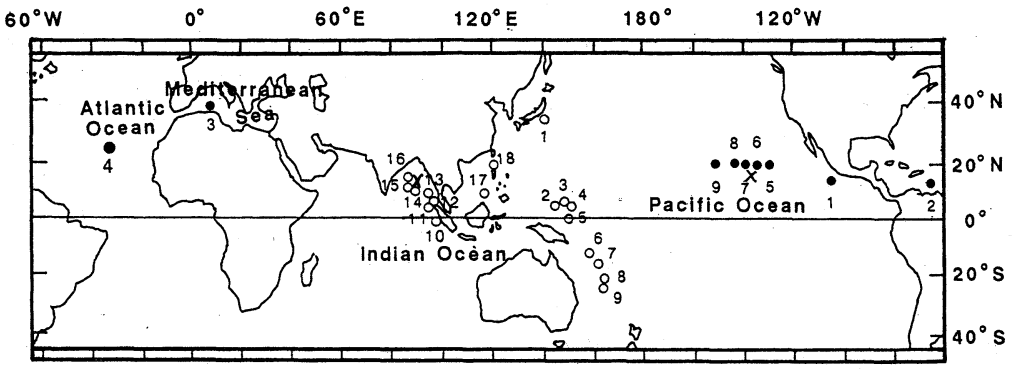

Fig. 1. Regional distribution of the observation stations.
Solid circles show the observation stations in the first period (from 1990 to 1991), and open ones in the second period (from 1991 to 1992). Symbol X indicates the position of tuna long-lining operation in each period.

sensation elements of this meter. The calibration of the meter was corrected under the standard light source of DXW120V/100W every time before the ship's departure for the navigation. The observation of underwater irradiances was generally conducted around the time of sun's meridian passage when it came up to the maximum altitude. Each measurement was fundamentally carried out at 7 spots arranged at every depth of 5m in the water between the sea surface (practically from the surface to lm) and the depth of 30m. As a matter of fact, however, the distribution of underwater irradiance in the water more than the depth of 30m was also investigated, extending up to the euphotic zone where the value of irradiance was reduced to 1% of its surface value. (JERLOV, 1976)

The conventional tuna longline gear was employed for the experimental fishing operation, setting the gear early in the morning and hauling in the afternoon. The depth of water, in which tuna was caught, was calculated from the depth of the hook attached at the end of the leader(shelf-recorded depth meters were hung on the leader).

3. Results and Discussion

3-1 Distributions of relative irradiance and spectral light energy in the oceans and their adjacent seas

Figs. 2(a) to 2(d) show each distribution of relative irradiance in the different regions such as the Coral Sea in the Pacific Ocean (Stn. 52-9), the central area in the Atlantic Ocean (Stn. 49-4), the western area in the Mediterranean Sea (Stn. 49-3) and the Andaman Sea in the Indian Ocean (stn. 52-12). Each solid line exhibited in those Figures stands for the wave length of the respective spectral light transmitted. It is a phenomenon in common to those sea regions that the wave length of 481nm has the best light transmittance and that of 709nm has the worst one. It is also common in those regions except the Andaman Sea that the wave lengths so far between 443nm and 683nm constantly keep the same order of descending light transmittance. Such a tendency is traced at 25 stations out of all the observation stations. In respect to the wave lengths of 481, 554, and 709nm, the depth in each ocean of which the irradiance value is reduced to 10% of its surface value is listed in Table 1. It is understood through this talbe that the shorter wave length of 481nm has wider differences in light transmittance than those of the longer wave length of 709nm in each ocean.

Fig. 3 exhibits the distributions of spectral light energies both in the Coral Sea of the Pacific Ocean where its water mass shows the best light transmittance and in the Andaman Sea of the Indian Ocean where its water mass constantly indicates the worst one throughout all the surveyed regions. In comparison of the relative irradiance values in both regional waters, the differential gaps are large on the shorter wavelength side of the border, 550nm, while those the longer wavelength side are very small. The cause of such phenomena can be concluded that the attenuation of the longer wavelength

Table 1. Depth in each ocean which the irradiance values is reduced to 10% of its surface value.

Region Light	Pacific Ocean (Stn. 52-9)	Atlantic Ocean (Stn. 49-4)	Mediterranean Sea (Stn. 49-3)	Indian Ocean (Stn. 52-12)
481 nm	90 m	88 m	52 m	25 m
554 nm	34	33	28	21
709 nm	4.0	3.7	3.5	3.2

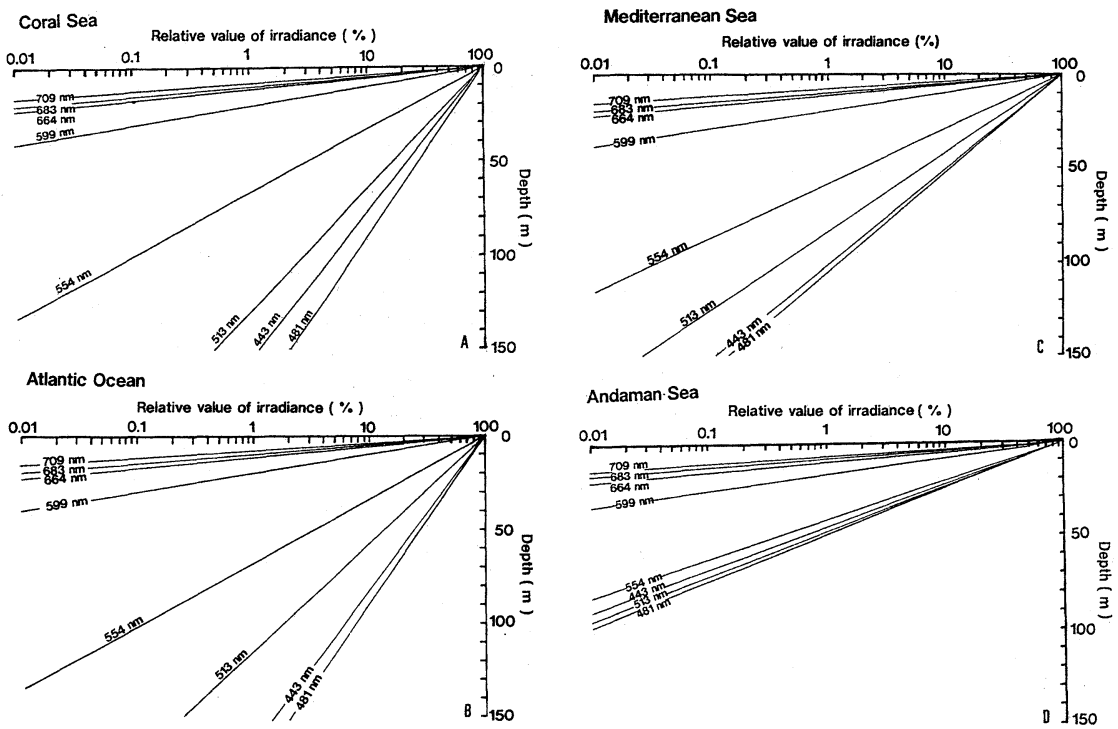

Fig. 2. Depth distribution of spectral relative irradiance in four sea regions.
(A) Pacific Ocean (Stn. 52-9) (B) Atlantic Ocean (Stn. 49-4)
(C) Mediterranean Sea (Stn. 49-3) (D) Indian Sea (Stn. 52-12)

lights mainly depends on the light absorption by sea water itself while that of the shorter wavelength lights is due to the light absorption and scattering by suspended matters and dissolved substances in sea water. This suggests that there is a wide difference in concentration of suspended matters and dissolved substances between both regional waters. Such a result of this study agrees with the achievements made by TYLER and SMITH (1970), MATSUIKE (1973), MOREL *et al.* (1974), and OKAMI *et al.* (1978).

3-2 Classification of optical water types in all the surveyed regions

An optical water type classification in all the observation stations is shown in Table 2. This classification is achieved according to the system of JERLOV (1951;1976). As listed in the Table, each water mass in the offshore region of the Hawaiian Is. and the Coral Sea region in the Pacific Ocean corresponds to the water type IA, respectively; each one in the Kuroshio, the Caribbean Sea, and the western region of the Mediterranean Sea comes under the water type IB; each water mass of Mexican offshore region in the Pacific Ocean, the Andaman Sea in the Indian Ocean and the South China Sea agrees with a water type between II and III. Since 4 to 5 observation stations are particularly assigned to

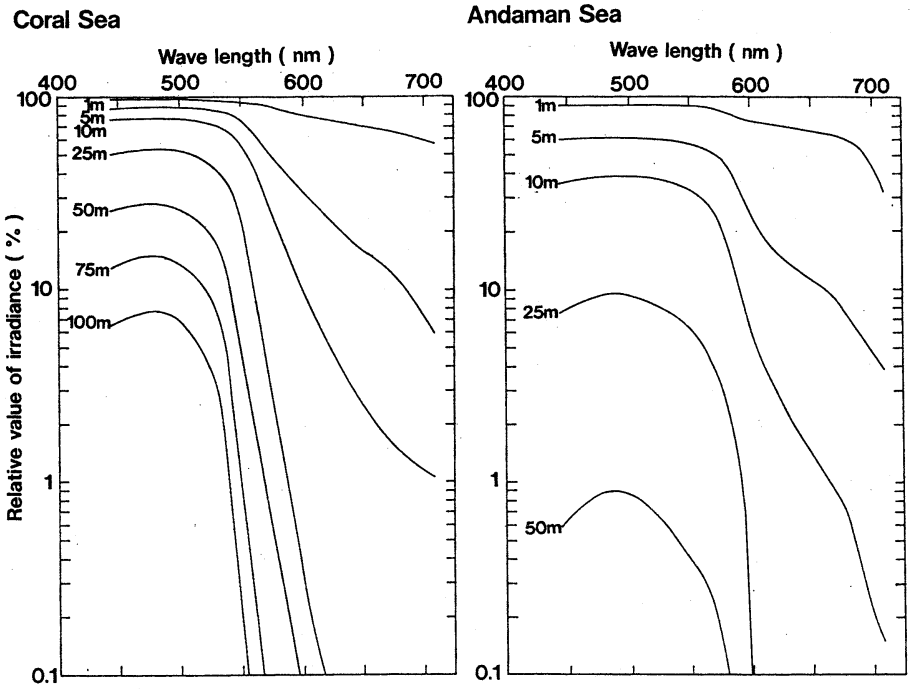

Fig. 3. Distributions of spectral light energies by depth in two sea regions.

Table 2. An optical water type classification in all the observation stations. Asterisk* stands for a dominant type.

Ocean	Sea region	Number of station	Optical water type
Pacific O.	Kuroshio reg.	1	IB
	Off Hawaii reg.	5	IA*-IB
	Off Mexico reg.	1	II-III
	Equatorial reg.	4	IB-II*
	Coral Sea reg.	4	IA*-IB
Atlantic O.	Caribbean Sea reg.	1	IB
	Central reg.	1	IA
Indian O.	Bay of Bengal reg.	3	IB*-II
	Andaman Sea reg.	2	II-III
	Off Sumatora Is. reg.	2	IB-II
Mediterranean Sea	Western sea reg.	1	IB
South China Sea	Northern and southern sea reg.	2	II-III

each of the offshore region of the Hawaiian Is., the equatorial region off New Guinea, and the Coral Sea in the Pacific Ocean, the water types in those regions are considered as a result of the mean optical measurements. Anyhow, it is interesting that those water types agree with the classification achieved by Jerlov almost 25 years ago. This means that the turbidity in those regions scarcely change with a secular variation. On the other hand, each water mass

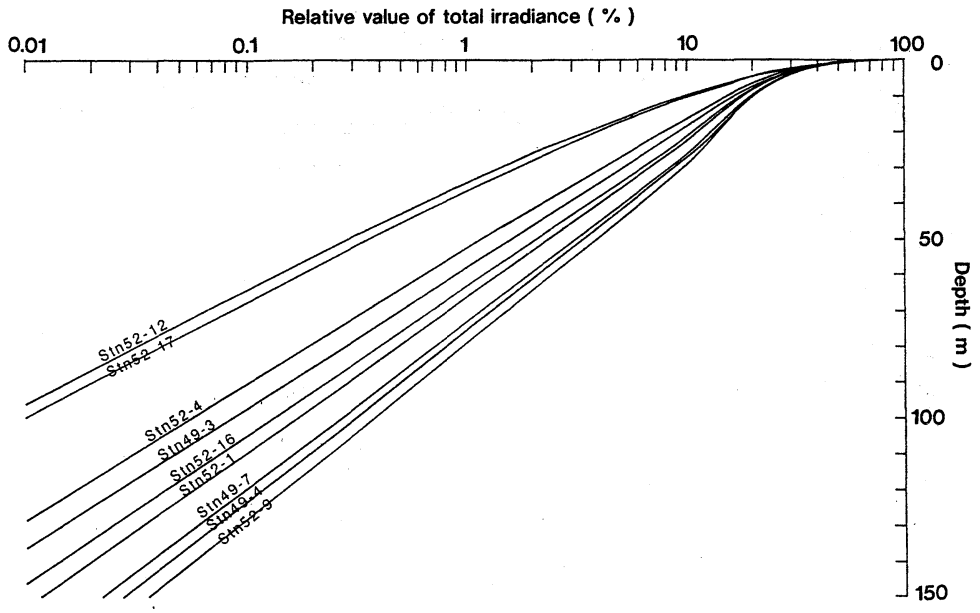

Fig. 4. Depth distribution of relative total irradiance in each sea region.

of the region located not far from the continents or the islands comes under one of other water types of which light transmittances are inferior to those in the regions mentioned above. It can be reasonably said that such a phenomenon is due to the effect of muddy water run out of the land into the sea.

Fig. 4 is prepared on the basis of Table 2, showing the distribution of underwater energies of all the spectral lights in the major regions. In those regions, the depth, in which underwater irradiace is reduced to 1% of its surface value, varies considerably with the different regions. For example, such the water exists in 79m deep in the Coral Sea (Stn. 52-9), 66m deep in the Kuroshio(Stn. 52-1), 59m deep in the Mediterranean Sea (Stn. 49-3) and 34m deep in the Andaman Sea (Stn. 52-12), respectively. Besides, the respective irradiace value (i. e. the percentage of the surface irradiance value) in 50m deep is 4.8%, 2.3%, 1.6% and 0.28% according to the order of the regions stated in the preceding paragraph.

3-3 Optical environment in the tuna fishing ground

The oceanic regions, in which experimental tuna longlining operations for this study were carried out, are the offshore water of the Hawaiian Is. in the Pacific Ocean and the Bay of Bengal in the Indian Ocean. And, most of the regions surveyed for this study agree with those of major tuna fishing grounds of the world (TAYAMA, 1980). Based on such an assumption that the fished depth of tuna is equal to the range of living sphere, the optical environments of tuna fishing grounds in the Pacific, the Indian, the Atlantic Ocean and the Mediterranean Sea are investigated. The fished depths of tuna are between 65m and 110m deep in the offshore water of the Hwaiian Is., which are resulted from experimental operations carried out in the first period, and between 60m and 120m deep in the Bay of Bengal conducted in the second period. Thus, these ranges in depth in the two regions resemble each other. Fished depths in other fishing grounds are obtained on referring to the relevant records and literatures or through the vertical configurations of physical properties in the different oceans. The results are between 150m and 380m deep in the Coral Sea in the Pacific Ocean (SAITO, 1992), between 50m and 150m deep in the central region of the Atlantic Ocean (KAWAI, 1969), and between 50m and 100m deep in the western region of the Mediterranean Sea (YAMADA, private information), respectively. Under the circumstances, it

Table 3. Absolute and relative values of underwater total light in the tuna maneuvering spheres of the every fishing ground. Tuna maneuvering spheres shown by asterisks* were obtained on referring to the literatures.

Item \ Fishing ground	Bay of Bengal	Off Hawaii reg.	Coral Sea	Atlantic O.	Mediterranean S.
Tuna maneuvering sphere (m)	60-120	65-110	150-380*[1]	50-150*[2]	50-100Z*[3]
Total light Absolute value (μw/cm^2)	12-360	42-315	0.02-13	8-891	17.6-336
Relative value (%)	4-120 $\times10^{-2}$	2-15 $\times10^{-1}$	6.9 $\times10^{-7}$ ~ 3.6 $\times10^{-2}$	3-330 $\times10^{-2}$	8.4-160 $\times10^{-2}$

can be said that the fished depths of tuna in the objective fishing grounds for this study is in the range from 50m to 150m deep.

The values of underwater spectral light energy in the depth of 50m to 100m are little on the longer wavelength side while those are large on the shorter wavelength side as shown in Fig. 2. This means that the spectral blue light transmitted there is more predominant than any other spectral lights. This agrees with the fact discovered by KOBAYASHI (1962) and KAWAMURA *et al.*(1981) that the best luminous efficiency wavelength band of tuna's eye is more or less than 490nm which is the major wave length of the blue light. Such a phenomenon that the responsive wave length of tuna's light sensing organ agrees with the most predominant wave length in the water of maneuvering sphere gives us a great deal of interest.

In Table 3, the absolute and relative values of underwater total irradiances in the tuna maneuvering spheres of the every fishing ground are tabulated. In this case, the practical measurements of 2.1 to 3.6×10^4 μw/cm^2, of which mean value is 2.7×10^4 μw/cm^2, are used for the irradiance values in the surface water (i.e. practically from the surface 0 m to 1 m) and the percentages with which the underwater irradiance values reduced in accordance with the depths of water are quoted from Fig. 4. As seen in the Table, the underwater irradiance values of the tuna maneuvering sphere differ according to each fishing ground, and their differential ranges are very wide indicating 2×10^{-2} to 8.9×10^2 μw/cm^2. The cause of this wide differential gaps can be attributed to such a fact that tuna in the Coral Sea of the Pacific Ocean is able to move up to the very deep water in which underwater irradiance shows an extremely small value. This small irradiance value of 2×10^{-2} to 1.3×10 μw/cm^2 can stand in comparison with 3×10^{-1} μw/cm^2 which is reported to be the irradiance value in the surface water during the full moon night (WATERMAN, 1974). It might be considered, therefore, that, so far as the daytime around the sun's meridian passage is concerned, the tuna species inhabit in the dark environment (SAKAMOTO, 1985). Besides, it can be found out also from Table 3 that the irradiance in the tuna maneuvering sphere of every fishing ground except that of the Coral Sea is within a certain range of around 5×10 to 3.2×10^2 μw/cm^2.

The practical underwater irradiance value fluctuates according to its value in the sky which changes every season and every moment. Under the circumstances, the further discussion about the underwater irradiance in the tuna maneuvering sphere will be proceeded by the use of its relative value. As seen in Table 3, the relative irradiance value considerably varies according to the different fishing grounds as same as the case of its absolute value; the relative irradiance value except that of the Coral Sea is within the range of 0.2 to 1.2%. These values are very small comparing with those of 2.2 to 8.2% found in the Bay of Bengal (MORINAGA *et al.*, 1992). The reason can be considered that because the minimum concentration layer of dissolved oxygen located in the Bay of Bengal comes up to the subsurface layer, the tuna living sphere moves up to the extremely shallow water of which depth is from 38m to 69m. Accordingly, the underwater irradiance in the tuna

maneuvering sphere is common to every fishing ground which is located from Lat. 20° to 40° N., keeping a constant brightness equivalent to approximately 1% of the surface irradiance value. This suggests a possibility to use the knowledge of the regional irradiance distribution in the ocean for locating the tuna fishing ground.

Aknowledgements

The authors express their sincere thanks to Dr. K. MATSUIKE, Professor of Tokyo Univ. of Fisheries for his valuable comments on this paper. Also, thanks are due to Prof. Y. SAOTOME, Captain of the R/T Umitaka-maru of Tokyo Univ. of Fish., and the crew for their support during the observations.

This study was partially supported by a grant from the academic foundation of 100th anniversary of Tokyo Univ. of Fish.

References

BAUER, D. and A. IVANOFF (1970): Spectro-irradiance-meter. Cah. Oceanogr., **22**, 477–482.

CAREY, F. G. and B. H. ROBISON (1981): Daily pattern in the activities of swardfish, *Xiphias gladius*, observed by acoustic telemetry. Fish. Bull., **79**, 277–292.

HANAMOTO, E. (1986): Effect of oceanographic environment on bigeye tuna distribution. Spe. Rep. Kanagawa Pref. Fish. Exp. Sta. 2. (in Japanese)

INGHAM, M. C., S. K. COOK and T. A. HAUSKNECHT (1977): Oxyclines characteristics and Skipjack tuna distribution in the southeastern tropical Atlantic. Fish. Bull., **75**, 857–865.

JERLOV, N. G. (1951): Optical studies of ocean water. Rep. Swedish Deep-Sea Exped., **3**, 1–59.

JERLOV, N. G. (1964): Optical classification of ocean water. *In* : Physical Aspects of Light in the Sea. Univ. Hawaii Press, Honolulu, Hawaii, 45–49.

JERLOV, N. G. (1968): Optical Oceanography. Els. Oceanogr. Ser., 5 Els., Amsterdam.

JERLOV, N. G. (1976): Marine Optics. Els. Oceanogr. Ser., 14 Els., Amsterdam.

KAWAI, H. (1969): On the relationship between thermal structure and distribution of long-line fishing-grounds of tunas in the Intertropical Atlantic-I. Analysis based on isotherms on level surface, topographies of thermocline, etc. Bull. Far. Seas Fish. Res. Lab., No. 2.

KAWAMURA, G., W. NISHIMURA, S. UEDA and T. NISHI (1981): Vision in Tunas and Marlins. Mem. Kagoshima Univ. Res. Center S. Pac., ol. 1, No. 2.

KOBAYASHI, H. (1962): A comparative study on electroretinogram in fish with special reference to ecological aspects. J. Shimonoseki Coll. Fish., **11**, 407–538.

KURITA, Y., Y. SAOTOME, I. KASUGA and T. HAYASHI (1991): Relation between tuna-catches and oceanic condition in Bengal Bay. Bull. Japan Soc. Fish. Oceanogr., **55**, 18–24. (in Japanese)

MATSUIKE, K. (1973): A study on opticl nature in oceanic waters. La mer, **11**, 1–44.

MOREL, A. and L. CALOUMENOS (1974): Variabilite de la repartition spectrale de l'energie photosynthetique. In: Upwelling Ecosystem, Analysis Conf. Proc., Marseille, 1973. Tethys, **6**, 93–104.

MORINAGA, T., A. IMAZEKI, S. TAKEDA and H. ARAKAWA (1992): The physical chemical and optical environment of the tuna's maneuvering sphere in the Bay of Bengal. La mer, **30**, 5–16.

OKAMI, N., M. KISHINO and S. SUGIHARA (1978): Measurements of spectral irradiance in the sea around the Japanese Islands. Tech. Rep. Phy. Oceanogr. Lab., Inst. Phys. Chem. Res., **2**, 1–130.

OKAMI, N., M. KISHINO, S. SUGIHARA and S. UNOKI (1981): Measurements of spectral irradiance in Tokyo Bay. Tech. Rep. Phy. Oceanogr. Lab., Inst. Phys. Chem. Res., **5**, 1–75.

SAITO, S. (1992): The Swimming layer of tuna and fishing method for longlining. Seizando-shoten, Tokyo (in Japanese).

SAKAMOTO, W. (1985): Environment of fishing ground and light. *In*: Marine environmental optics, SUGIMORI and SAKAMOTO eds. Toukaidaigaku-shuppankai, Tokyo. (in Japanese)

SUGIHARA, S. and N. INOUE (1976): Measurements of spectral energy distribution in the sea. Sci. Pap. Inst. Phys. Chem. Res. **70**, 8–15.

TAYAMA, J. (1980): Maguro no hanashi. Kyoritu-kagaku-books, Tokyo. (in Japanese)

TYLER, J. E. and R. C. SMITH (1966): Submersible spectroradiometer. J. Opt. Soc. Am., **56**, 1390–1396.

TYLER, J. E. and R. C. SMITH (1970): Measurements of spectral irradiance under water. Ocean Series. I. Gordon and Breach, New York 1–103.

UDA, M. (1960): Kaiyo-gyojyo-gaku. Kouseisha-

kouseikaku, Tokyo. 1–347. (in Japanese)
WATERMAN, T. H. (1974): Underwater light and the orientation of animals. *In*: Optical aspects of oceanography, JERLOV and NIELSEN eds., Academic press., 415–443.

三大洋における海中分光照度分布とまぐろ漁場の光環境

森永　勤・今関　昭博・森川　由隆

要旨：1990年から1992年までの間の二回の冬期に、東京水産大学研究練習船海鷹丸で地球規模の広範囲な海域において、著者等は高性能な水中放射照度計を用い、各海域の表層から水深30mまで八波長（波長；443, 481, 513, 554, 599, 664, 683, 709nm）の分光照度を測定した。同時に、まぐろ延縄による釣獲試験をも実施した。

海中光の透過が最も良い波長及び悪い波長はそれぞれ481nmと709nmである。透過の悪くなる波長の序列はほとんどの海域で、短い波長443nmから長い波長683nmへの移行である。光透過の深度の海域別相違は短波長側で大きく、長波長側で小さい。太平洋珊瑚海の水塊は JERLOV（1976）の光学的水塊分類の oceanic type IA に該当し、非常に清澄な海水である。この海域の濁りの永年変化は少ないものと考えられる。太平洋、インド洋、大西洋及び地中海における北緯20度から40度付近のまぐろ漁場に共通して、生息領域（水深50～150m）の分光分布では青色光が卓越している。又、そこにおける海中照度（全光）の絶対値及び相対値は、それぞれ 50～320 μ w/cm^2 及び 0.2～1.2%と一定範囲にある。このことはまぐろ漁場探査の一つの手掛りを示唆している。

La mer 31: 59–78, 1993
Société franco-japonaise d'océanographie, Tokyo

Dispersion of passive tracers in an oceanic mesoscale eddy field*

Keiko YOKOYAMA**, *** and Kenzo TAKANO**

Abstract: Numerical experiments are carried out for estimating the effect of the mesoscale eddies on the dispersion of dynamically passive tracers in a model ocean. Tracers are dispersed by advection and diffusion. The velocity field is supplied as a function of time from a prognostic, four-level, eddy resolving ocean circulation model. The model ocean extending from 25.0°N to 50.5°N in latitude and over 24.8° in longitude may be considered as a portion of the northwestern Pacific Ocean of simplified geometry. Its depth is 4000m except at a ridge 1900m high. The grid size is 0.375° in latitude and 0.43° in longitude. The substance concentration is calculated at depths of 80, 400, 1600 and 2600m by integrating in time a three-dimensional advection-diffusion equation.

The large scale dispersion over the whole ocean basin is shown in two cases; one is the dispersion from an instantaneous plane source distributed over the whole ocean surface, and the other is the dispersion from an instantaneous point source on the bottom. The coefficient of horizontal diffusion is $10^3 m^2/s$. The coefficient of vertical diffusion is $10^{-4} m^2/s$. The complete dispersion defined by the uniform distribution of tracers over the whole ocean basin is achieved in about 30 years in both cases. If the time-average velocity field is used instead of the eddy field, it is achieved in about 50 years. The dispersion is significantly enhanced by mesoscale eddies. Since the time required for the complete dispersion depends on the volume of the ocean basin, and the volume of the model ocean is $1.77 \times 10^7 km^3$ compared with $72.4 \times 10^7 km^3$ of the Pacific Ocean and $137 \times 10^7 km^3$ of the world ocean, a simulated period of 30 years should be equivalent to 1250 years in the Pacific Ocean and 2310 years in the world ocean. Both figures surprisingly agree with the turnover time estimated from ^{14}C and others.

1. Introduction

The ocean interior is filled with velocity fluctuations having horizontal scales of some hundreds of kilometers, vertical scales approximately equal to the water depth and time scales of several weeks, which are commonly referred to as mesoscale eddies. Their typical phase velocity is about 10cm/s. The typical particle velocity is also about 10cm/s. Since the time-average is about 1cm/s or less, the eddy kinetic energy is predominant in the mid-ocean kinetic energy.

The eddy-induced dispersion has important oceanographic consequences in a wide range of fields. It is linked to the general circulation through the transport of momentum, heat and salt and to the ocean-atmosphere system through the transport of heat, water (salt) and carbon dioxide, to biological productivity through the transport of nutrients, phytoplankton and fish larvae, and to the distribution of geochemical tracers such as tritium, oxygen, chlorofluorocarbons and ^{14}C.

In addition, it is closely linked to the disposal of industrial wastes and the dispersion of various pollutants, which is the motivation of the present study.

In these regards, not a few works, either observational or theoretical, have been done for understanding to what extent the eddy-induced dispersion affects physical, chemical and biological processes in the mid-ocean (for instance, HAIDVOGEL *et al.*, 1983).

* Received March 1, 1993
** School of Environmental Sciences, University of Tsukuba, Tsukuba, Ibaraki-ken 305 Japan
*** Present affiliation: NTT Data Communications Systems Corporation, Toranomon, Tokyo 105 Japan

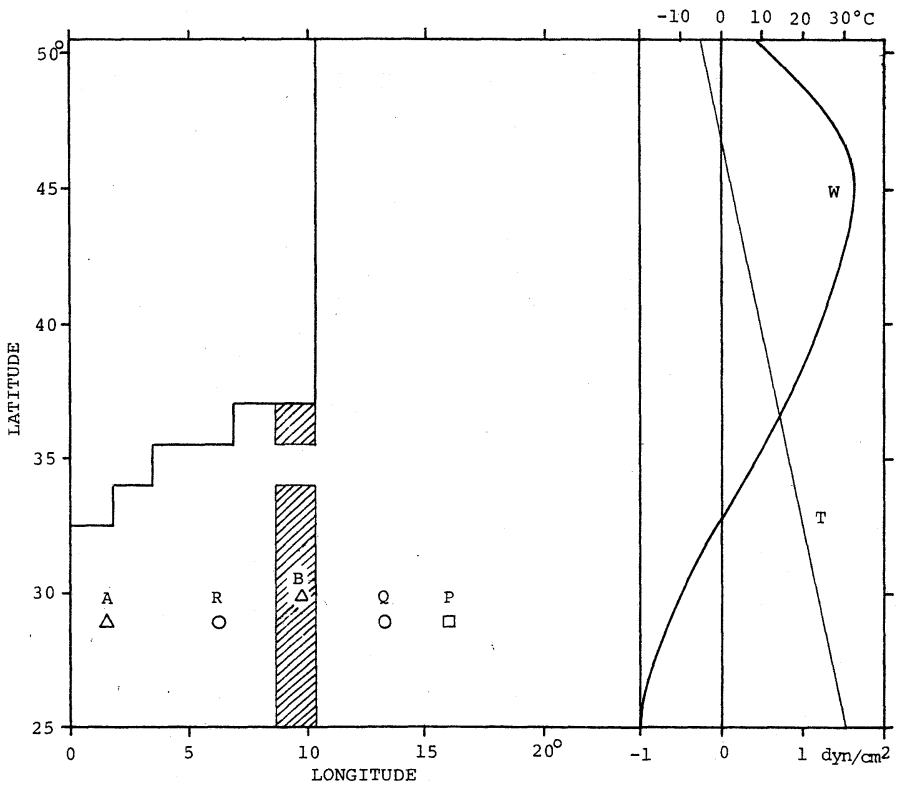

Fig. 1. Geometry of the ocean basin, wind stress (W) and reference atmospheric temperature (T). A ridge with a gap is shaded. A point source is located at P. Stick diagrams will be shown at Points A and B, and power spectra at Q and R.

However, our understanding still remains poor. The present study is concerned with dispersion of dynamically passive tracers, as a part of a preoperational survey of an area at 30°N, 147°E for ocean bottom disposal of radioactive wastes planned by Science and Technology Agency of Japan. A finite difference advection-diffusion equation for the tracers, initially distributed to the whole ocean surface and to a limited area on the ocean floor, is solved in a model ocean. The velocity field is supplied from a prognostic, four-level, eddy resolving ocean circulation model.

2. Eddy resolving circulation model

Quality of the numerical experiments on the tracer dispersion depends on the quality of the mesoscale eddy field to be used, which in turn depends on the eddy resolving ocean circulation model. Therefore, the ocean circulation model is briefly described first. The model ocean extends over 24.8° in longitude and from 25°N to 50.5°N in latitude as shown in Fig.1. The grid size is 0.43° in longitude and 0.375° in latitude. Four levels are set up in the vertical; the horizontal components of velocity, temperature and pressure are defined at depths of 80, 400, 1600 and 2600m, and the vertical component of velocity is defined at depths of 240, 1000 and 2100m. The bottom is 4000m deep except at a ridge the top of which is 2100m deep. A narrow gap 1.5° wide in latitude divides the ridge into a northern and southern branch. The ocean geometry is somewhat similar to a portion of the western North Pacific Ocean.

The conventional Laplacian form is used for the subgrid scale diffusion of momentum and heat. The salinity is made constant (35‰) everywhere. The density is calculated by a formula of FRIEDRICH and LEVITUS (1972).

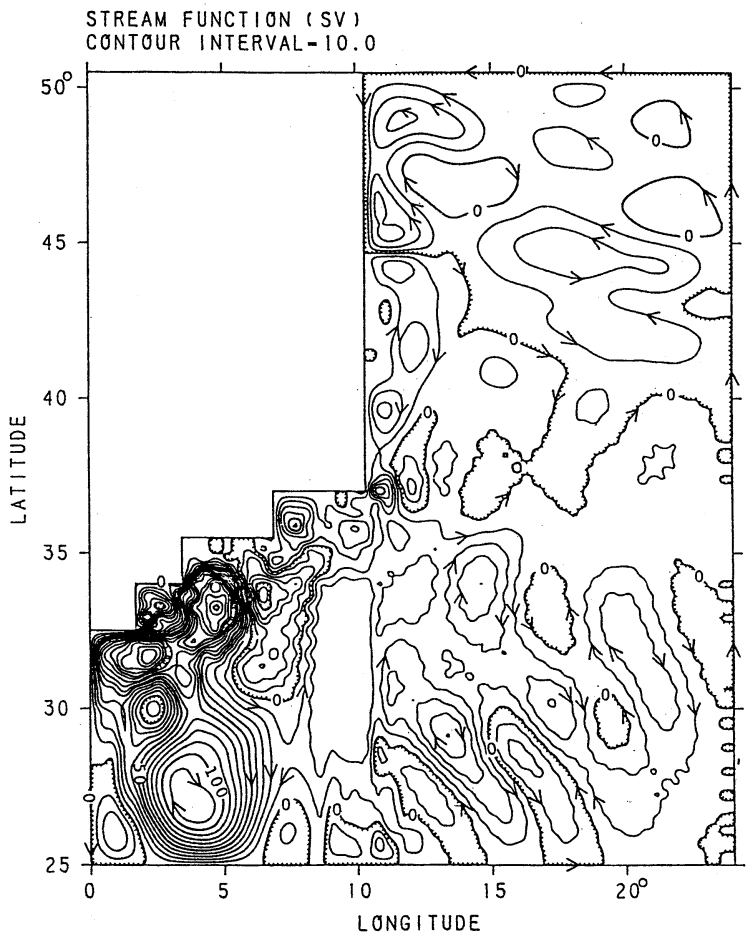

Fig. 2. A snapshot of the transport in terms of stream lines (units: Sv).

The circulation is driven by a prescribed wind stress and a prescribed reference atmospheric temperature shown in Fig.1. The wind stress has no meridional component. The surface heat flux is made proportional to the difference between the predicted surface temperature and the reference atmospheric temperature. The constant of proportionality is assumed to be 21W/m^2K (=50cal/cm^2 s K). There is no friction along the lower and lateral boundary. The vertical component of velocity vanishes at the surface (rigid-lid approximation). There is no heat flux across the lateral and lower boundary.

The finite differencing scheme is the same as that described in previous papers (TAKANO, 1974; Atomic Energy Management Center, 1986).

The coefficient of subgrid scale diffusion is $10^2 m^2/s$ for momentum and $10^3 m^2/s$ for heat. The coefficient of vertical diffusion is $10^{-4} m^2/s$ for momentum and heat. The time step is 30min.

In the initial state, the temperature is a function of depth and latitude only, the planetary vorticity advection for the barotropic component of velocity is balanced with the specified wind stress curl, and the shear current (baroclinic component of velocity) is determined from the given temperature distribution. Time integration is forwarded for about 230 years. For the last 80 years, the three components of velocity and temperature are saved every 2.5 days for analysis. The average temperature change rate is -2.1×10^{-3}°C/year if the

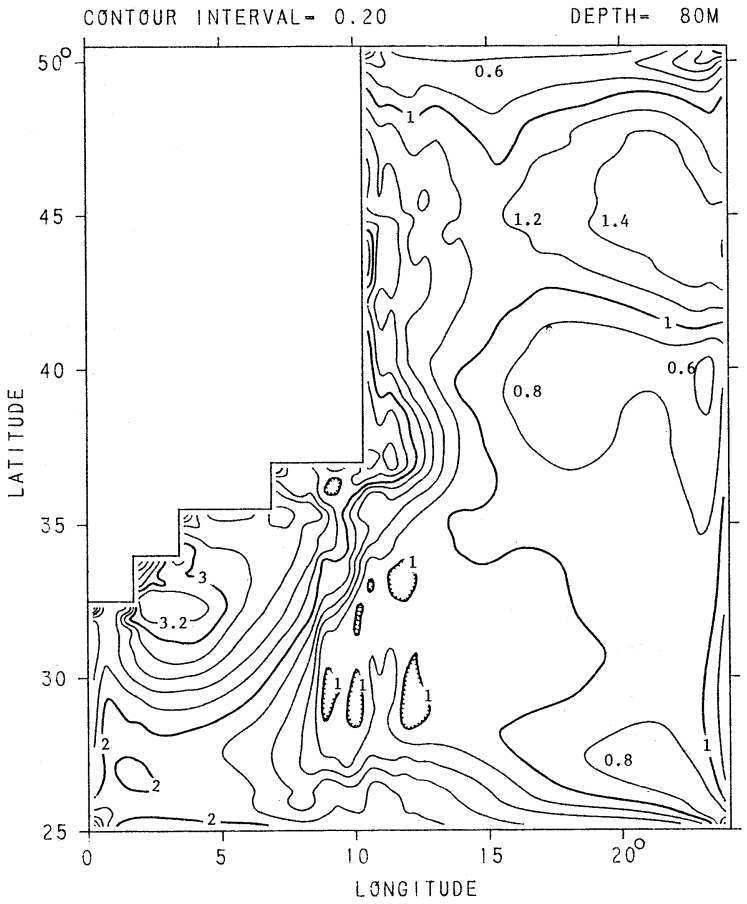

Fig. 3. Distribution of logarithms to the base ten of eddy kinetic energy (erg/cm^3) at a depth of 80m.

surface heat flux is calculated from the reference atmospheric temperature and surface temperature averaged over these 80 years, and then divided by the total water mass.

As a measure of the performance of the ocean model used here, Fig.2 shows a snapshot of the volume transport (vertical integral of the horizontal velocity from the bottom to the surface) in terms of the stream function. Mesoscale eddies are pronounced in and near the western boundary current flowing northeastward, while they are weaker in regions far apart from the western boundry current and on the ridge. There are, on the time-average (not shown), a subtropical gyre which transports 101Sv and a subarctic gyre which transports 41 Sv, but both gyres are veiled in strong mesoscale eddies in the snapshot.

Eddy activity distribution is described in Figs. 3 and 4 showing logarithms to the base ten of the eddy kinetic energy (erg/cm^3) at depths of 80 m and 2600 m. The maximum energy is found around 32.5°N, 3°E at both depths. It is four times greater at 80m than at 2600 m depth.

The mean kinetic energy is of almost the same order of magnitude as the eddy kinetic energy at a depth of 80m, but more than five orders of magnitude less in the greater part of the ocean basin at a depth of 2600 m except at the western boundary region where it is slightly less than the eddy kinetic energy.

Figure 5 gives examples of the velocity fluctuations in stick diagrams of the barotropic and baroclinic components of velocity at points A and B in Fig.1 for a period of 2580 days arbitrarily chosen. The deviations from the time-

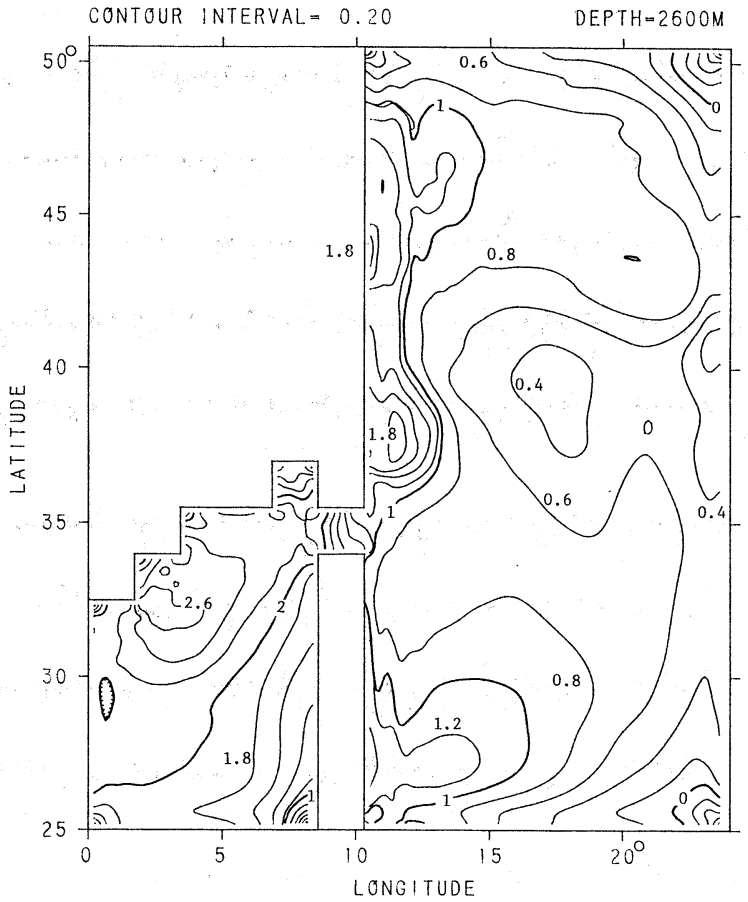

Fig. 4. Same as Fig. 3 except for a depth of 2600m.

average are shown. The average eastward and norhward barotropic components are −3.7 cm/s, −1.1 cm/s at A, and 0.073 cm/s, −1.4 cm/s at B, which are much smaller than the deviations. At A, the average eastward and northward baroclinic components of velocity are −0.96 cm/s, 3.6 cm/s at 80 m depth, −1.0 cm/s, 1.7 cm/s at 400 m depth, −0.17cm/s, −0.29 cm/s at 1600 m depth, 0.62 cm/s, −0.95 cm/s at 2600 m depth; at B, 3.8 cm/s, 1.3 cm/s at 80 m depth, 0.10 cm/s, 0.40 cm/s at 400 m depth, −0.90 cm/s, −0.55 cm/s at 1600 m depth, which are also much smaller than the deviations. Fluctuations of periods of about 100 days are apparent. The deviations of the barotropic com-ponent are much larger than those of the baroclinic components at most grid points throughout this period and any other period, but the formers are comparable with the latters at 400m depth at B.

The baroclinic components are well correlated between 80m and 400m depths. It is also the case between 1600m and 2600m, but the correlation is poor between 400m and 1600m depths. The barotropic components is correlated with the baroclinic components at 80m and 400m depths rather than at 1600m and 2600m depths.

Figure 6 shows stream lines for the meridional circulation calculated from the meridional and vertical component of velocity integrated over the parallel of latitude. If the velocity components are integrated, there appears no deep downwelling reaching to the bottom in high latitudes. Moreover, reflecting the limited size of the ocean basin, the meridional circulation is rather weak: the downward transport at high

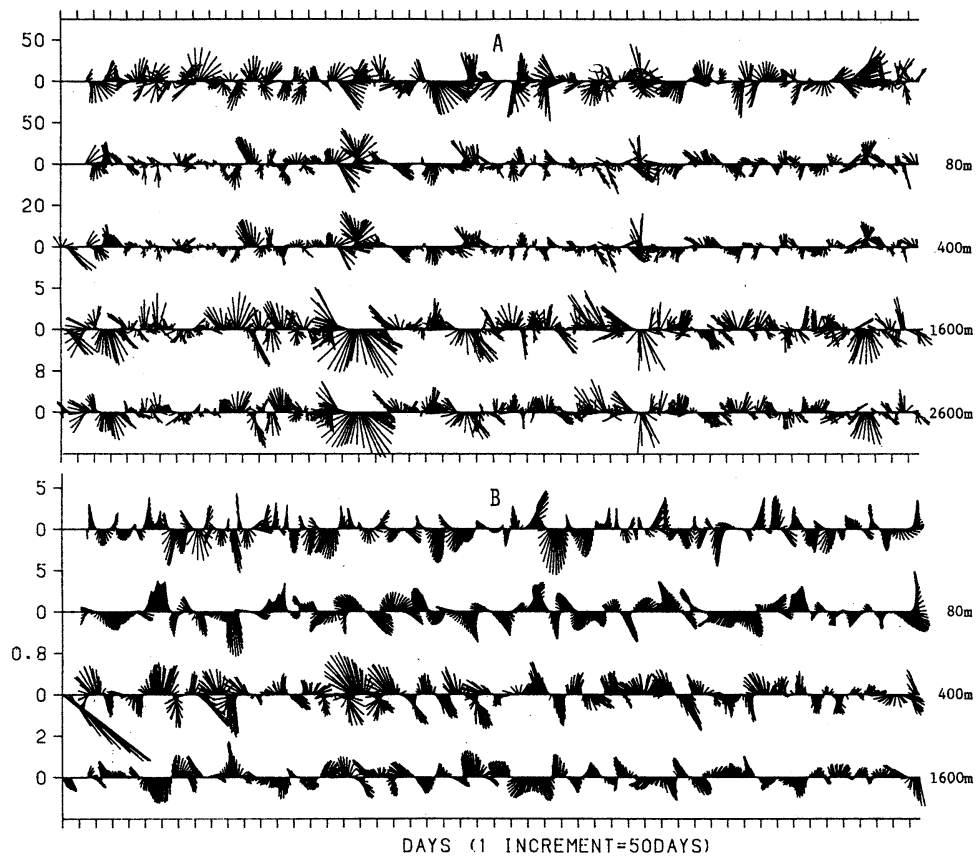

Fig. 5. Stick diagrams at Points A (upper panel) and B (lower panel). The top diagram of each panel is the deviation of the barotropic component from its time-average. The lower diagrams are the deviations of the baroclinic components from their time-averages. One increment in abscissa is 50 days. The scale in ordinate (cm/s) is variable.

latitudes is only 5 Sv. As to the velocity itself, the deviation from the time-average is much stronger than the time-average in most grid points, but the average meridional circulation calculated from the deviation is weak compared with that calculated from the time-average, because the effect of mesoscale eddies is almost canceled each other if integrated over the parallel of latitude.

Power spectra of the eastward and northward components of velocity are shown in Figs.7 and 8 at two points Q and R (Fig.1) arbitrarily chosen. Clearly appear mesoscale fluctuations of periods of some hundreds of days. For comparison, power spectra are calculated (not shown here) from observed 7-year current velocity data at a depth of 5000m at 30°N, 147°E (IMAWAKI and TAKANO, 1982), which was done also in the framework of the preoperational survey for ocean bottom disposal of radioactive wastes. Although the numerical simulation is successful in generating mesoscale fluctuations, energy decay in high frequencies is much sharper than that with the observed data. This sharp decay in the simulation could be attributed to neglect of the tidal currents and to a grid size of about 40 km which is too coarse to resolve small scale motions in high frequencies. Because the shortest resolvable wavelength is two times the grid size, the model cannot resolve fluctuations of wavelengths shorter than 80km, so that the kinetic energy in higher frequencies is more or less

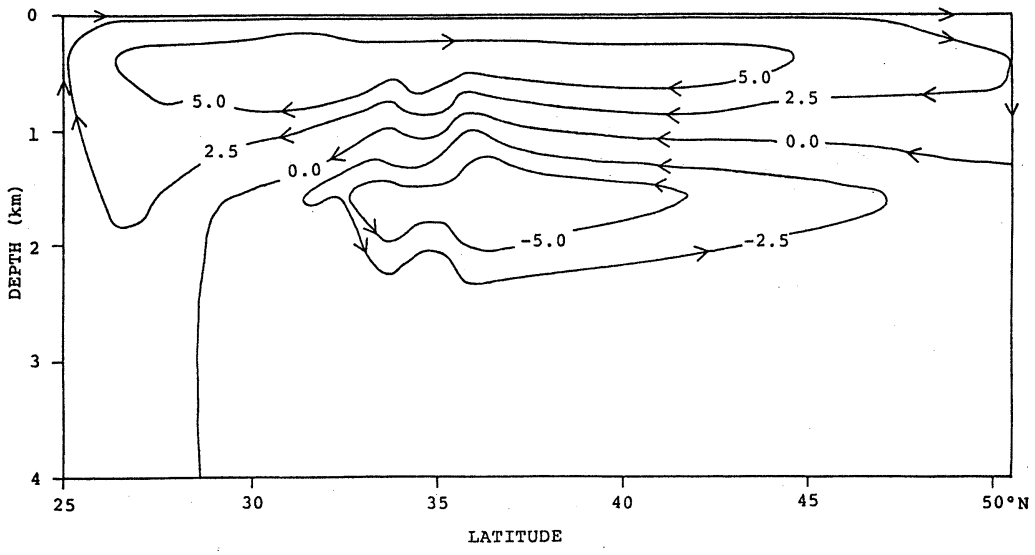

Fig. 6. Steam lines for the time-average of the meridional circulation (units: Sv)

cut off. Inertia oscillations are not resolved, either; their scales are too small. In short, the simulated velocity field is simpler than the observed one.

3. Numerical experiments on large scale dispersion

An advection-diffusion equation for concentration C of any dynamically passive tracer is solved as an initial-boundary value problem. The conventional Laplacian form is used for the subgrid scale diffusion. The coefficient of horizontal diffusion is $10^3 m^2/s$. The coefficient of vertical diffusion is $10^{-4} m^2/s$. A much more scale selective biharmoic formulation is useful for suppressing computational noise arising from advection and diffusion terms (YOKOYAMA and TAKANO, 1986), but is put aside on account of complicated finite difference analog of the lateral boundary condition.

Although the centered differncing (leap-frog) scheme is used basically for time integration, the Euler-Matsuno backward differencing scheme is used every ten time steps for suppressing computational noise and separation of the solutions. The centered differencing scheme is also used for space differencing except for both horizontal and vertical advection, which are calculated by the upcurrent scheme.

The velocity field is supplied from the ocean circulation model described above. Since the velocity data are available at intervals of 2.5 days, the velocity field at a given time necessary to time integration is calculated by linear interpolation of the two nearest data.

An additional term $-\alpha C$ appears in the equation if a radioactive substance with decay constant α is dealt with. However, the solution with $\alpha = 0$ also holds good for a radioactive substance provided that it is multiplied by a factor of $\exp(-\alpha t)$ (t: time), so that α is put as 0 in the present study.

Two cases are studied; dispersion from the surface (Case 1), and dispersion from the bottom (Case 2). In Case 1, a concentration of 50 in arbitrary units is uniformly given, as an initial condition, to each of all the grid points at the surface layer 240m thick. In Case 2, a concentration of 5000 in arbitrary units is given to Point P in Fig.1 at the bottom layer 1900m thick as an initial condition. The location of point P in Fig.1 might correspond with the location of a proposed area for the ocean bottom disposal of low-level radioactive wastes at 30° N, 147° E, about 400km east of the Izu-Ogasawara Ridge and about 500km south of the Kuroshio Extension. In both cases, there is no flux of C across the lateral, upper and lower boundaries.

Since the primary objective is to understand the effet of the mesoscale eddies, two runs are

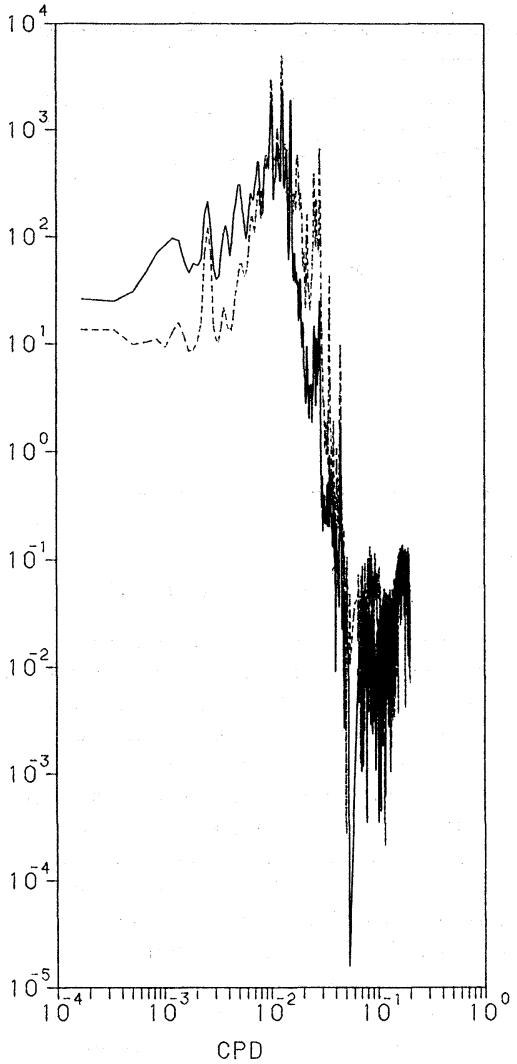

Fig. 7 Power spectra of the eastward (full line) and northward (broken line) components of velocity at 2600m depth at Point Q.

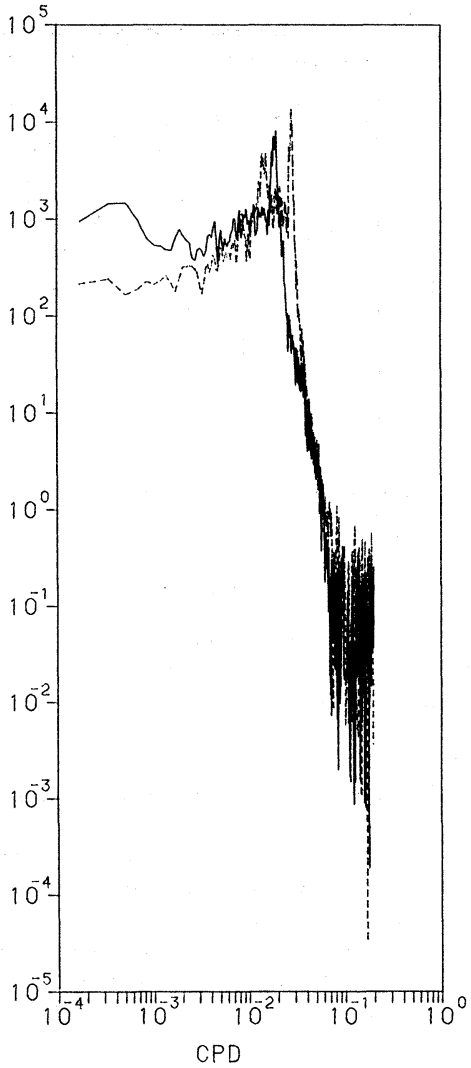

Fig. 8. Same as Fig.7 except for Point R.

achieved in each case; one is by using the velocity field comprising mesoscale eddies and the other by using the velocity field averaged over 80 years. Hereafter, the former is referred to as Case 1e and Case 2e, and the latter as Case 1a and Case 2a.

Time integration is forwarded by a time step of 1.5 hours in Cases 1e and 2e, and a time step of 2 hours in Cases 1a and 2a until a steady state is reached where the initially given substance is completely dispersed and its concentration becomes constant in space and time. Theoretically, this constant is 3.06 in Case 1 and 0.936 in Case 2, because the total amount of C, 5.43 $\times 10^7$ units in Case 1 and 1.66×10^7 units in Case 2, is initially given into a total water volume of $1.77 \times 10^7 km^3$. However, the value finally reached by time integration is 3.02 in Case 1e, 2.98 in Case 1a, 0.923 in Case 2e and 0.918 in Case 2a. The small discrepancies between these values and theoretical values (3.06 or 0.936) result from loss of C due to round-off and truncation in the course of time integration, which usually happens to such calculations on the computer.

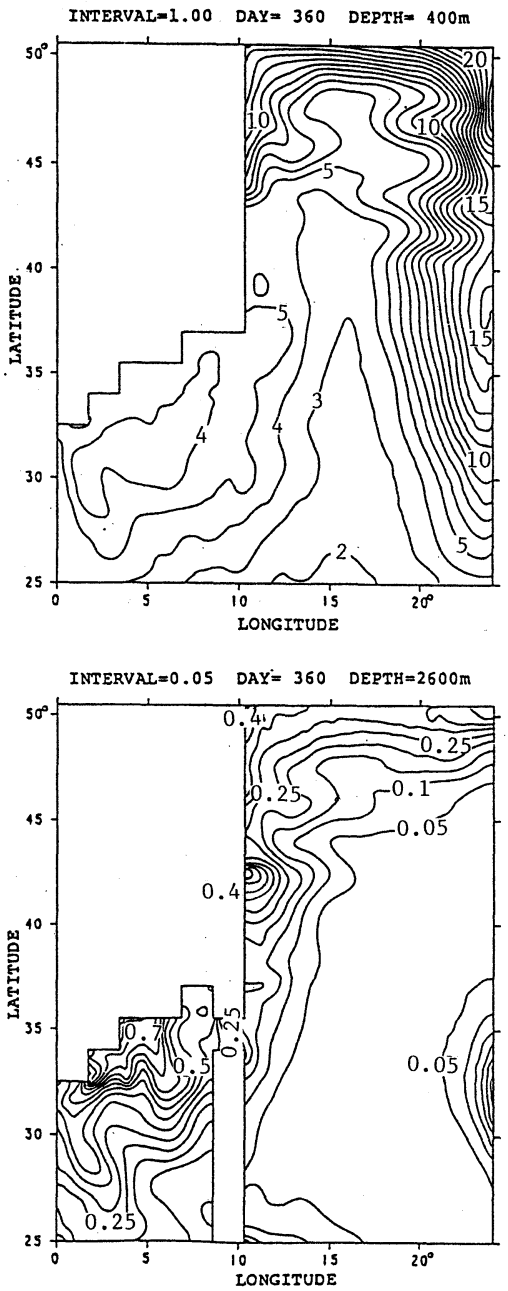

Fig. 9. Isopleths at depths of 400m and 2600m at day 360 in Case 1e.

4. Dispersion from the surface

4.1 Case 1e

Figure 9 shows isopleths of C at depths of 400m and 2600m at day 360 after setting in dispersion. Due to a strong sinking of surface water near the northern boundary, the concentration in lower layers increases first in the northern part of the basin and then disperses southward. At the surface, there are a convergence region near the western boundary around 42°N and another broad convergence region near the eastern boundary around 41°N, which are also sources of C for the lower layers, though not so strong as near the northern boundary. Isopleths at 400m depth do not suggest the presence of the ridge.

The averages over the parallel of latitude at days 360, 720 and 1440 are shown in Fig. 10. Near the northern boundary, there is a downward dispersion associated with a strong sinking. In the other surface regions there is no such a strong downward dispersion, which leads to a sharp vertical gradient of C between the surface layer and the underlying layer, in particular, in the southern region at the early stages (days 360 and 720). These features qualitatively agree with an observed distribution of anthropogenic tritium penetrating into deep waters (OSTLUND and BRESCHER, 1982). The sharp vertical gradient almost vanishes at day 1440, though the southward dispersion from the northern region is still persistent. Small spikes and a dome rising from the bottom in the isopleths at day 1440 are fictitious due to peculiarities of the computer plotting program.

The gap 1.5° wide in latitute of the ridge is not an effective pathway from the east to the west of the ridge in the bottom layer; the tracer sinking to lower layers from the northern boundary region and the surface convergence areas at the eastern boundary region at about 41°N and at the western boundary region does not come to the west of the ridge through the gap. In the bottom layer west of the ridge, C increases due to sinking from the upper layers where C is transported from the central and eastern regions by the subtropical gyre. Then, C at a depth of 2600m is higher on the western side than on the eastern side of the ridge.

Mesoscale fluctuations of isopleths due to the mesoscale eddies are seen throughout time integration until a steady state is reached.

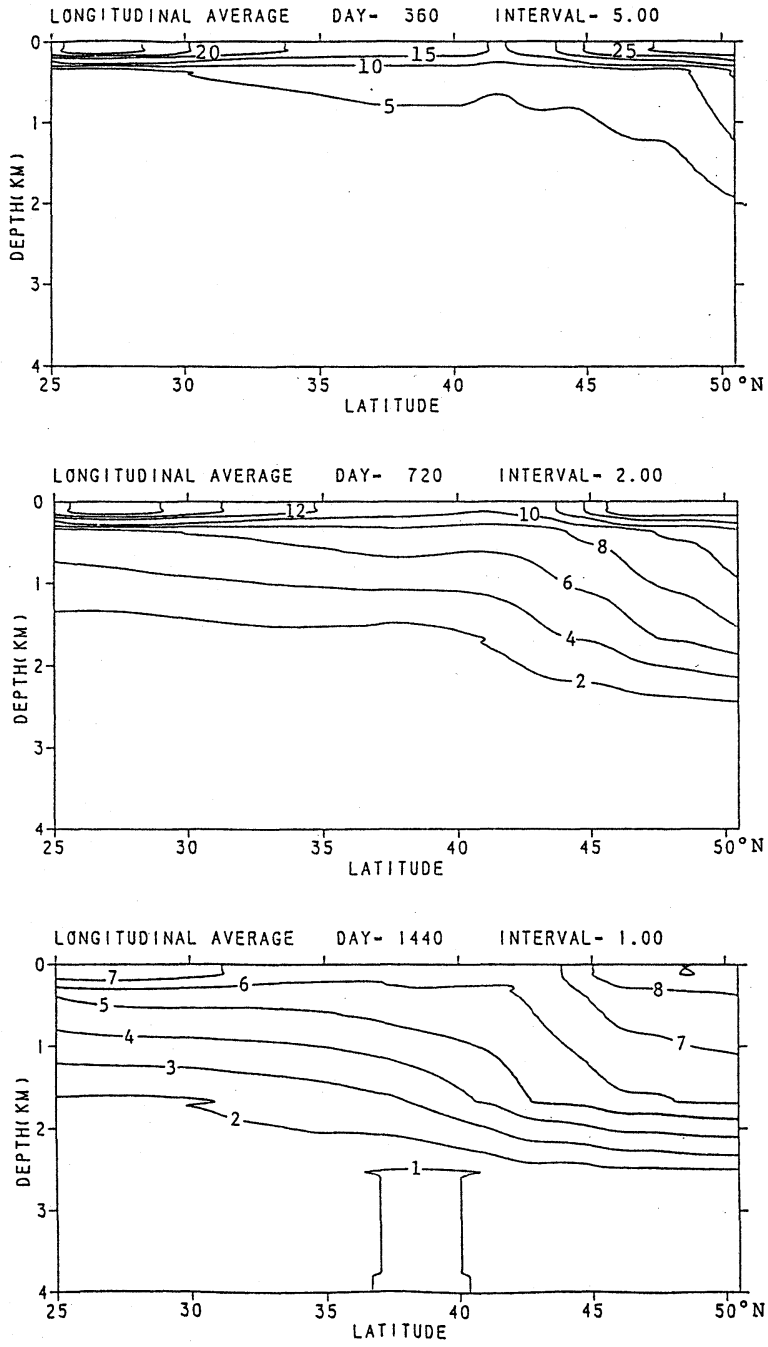

Fig. 10. Vertical-latitude distribution at days 360 (top), 720 (middle) and 1440 (bottom) in Case 1e.

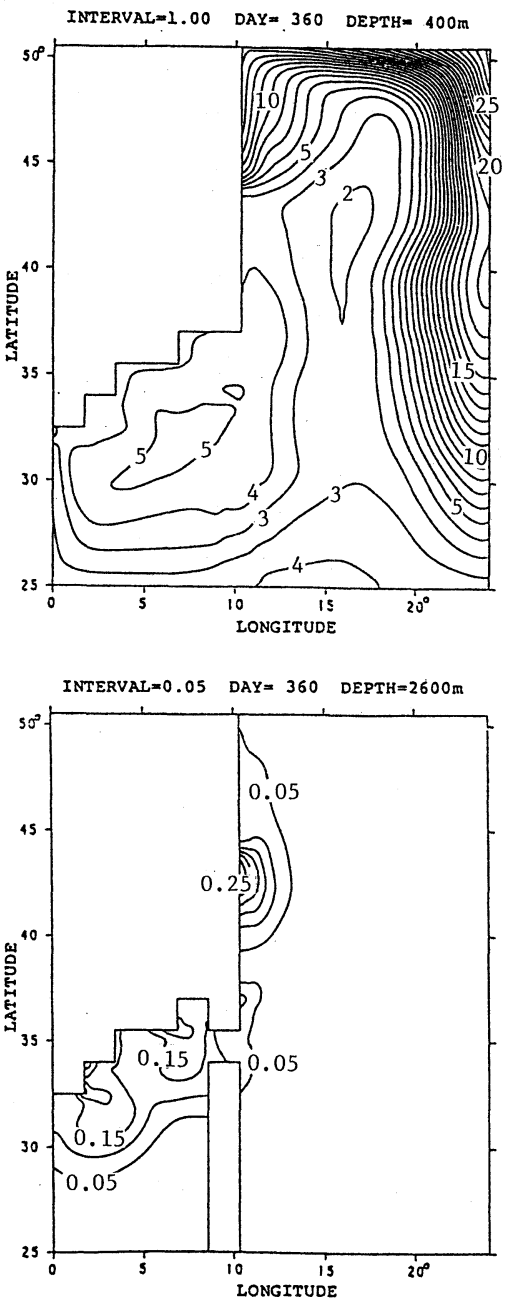

Fig. 11. Isopleths at depths of 400m and 2600m at day 360 in Case 1a.

4.2 case 1a

In this case, the advection is calculated with the time-average velocity field. Figure 11 shows isopleths at depths of 400m and 2600m at day 360. The isopleths become smoother without mesoscale eddies. Although the principal features of dispersion at 400m are similar to those in Case 1e, the concentration is higher, particularly near the northeastern corner and most of the eastern boundary areas, except in most areas between about 35° N and 45° N. At a depth of 2600m, the concentraion is everywhere lower than in Case 1e.

At a depth of 80m, the concentration near the northern boundary is about 34 in Case 1e and about 40 in Case 1a. Near the southern boundary, it is about 27 in Case 1e and about 37 in Case 1a, which indicates slower downward dispersion from the surface in Case 1a because of absence of mesoscale eddies. In the northern boundary region at a depth of 400m, the amount of C coming from the surface is smaller in Case 1a than in Case 1e, but the downward and southward dispersion from there are not strong, so that C stagnates to be higher than in Case 1e. This point will be again discussed later.

Figure 12 shows the average over the parallel of latitude at days 360, 720 and 1439. There is qualitatively no significant difference between Cases 1a and 1e (Fig.10), but the concentration at the surface layer is higher in Case 1a because of slower downward despersion.

5. Dispersion from the bottom

A concentration of 5000 in arbitrary units is initially given to the bottom layer at P, i. e., to a vertical pillar 1900m high of which the trapezoidal horizontal section is 41.7km in meridional side length and 41.9km in mean zonal side length.

5.1 Case 2e

At day 360 no dispersed substance practically reaches to the surface layer. The maximum surface concentration appears off the western coast from 33° N to 37° N, but is less than 0.01. Due to westward currents in the subtropical gyre at the upper two layers, the westward dispersion is more prominent than the northward dispersion at depths of 400m and 1600m (not shown here).

At day 720 the maximum surface concentration reaches to 0.19 at a coastal point (34° N, 1.92° E) and the maximum concentration at the bottom layer decreases to 5.5 which is located near Point P. The maximum concentration is

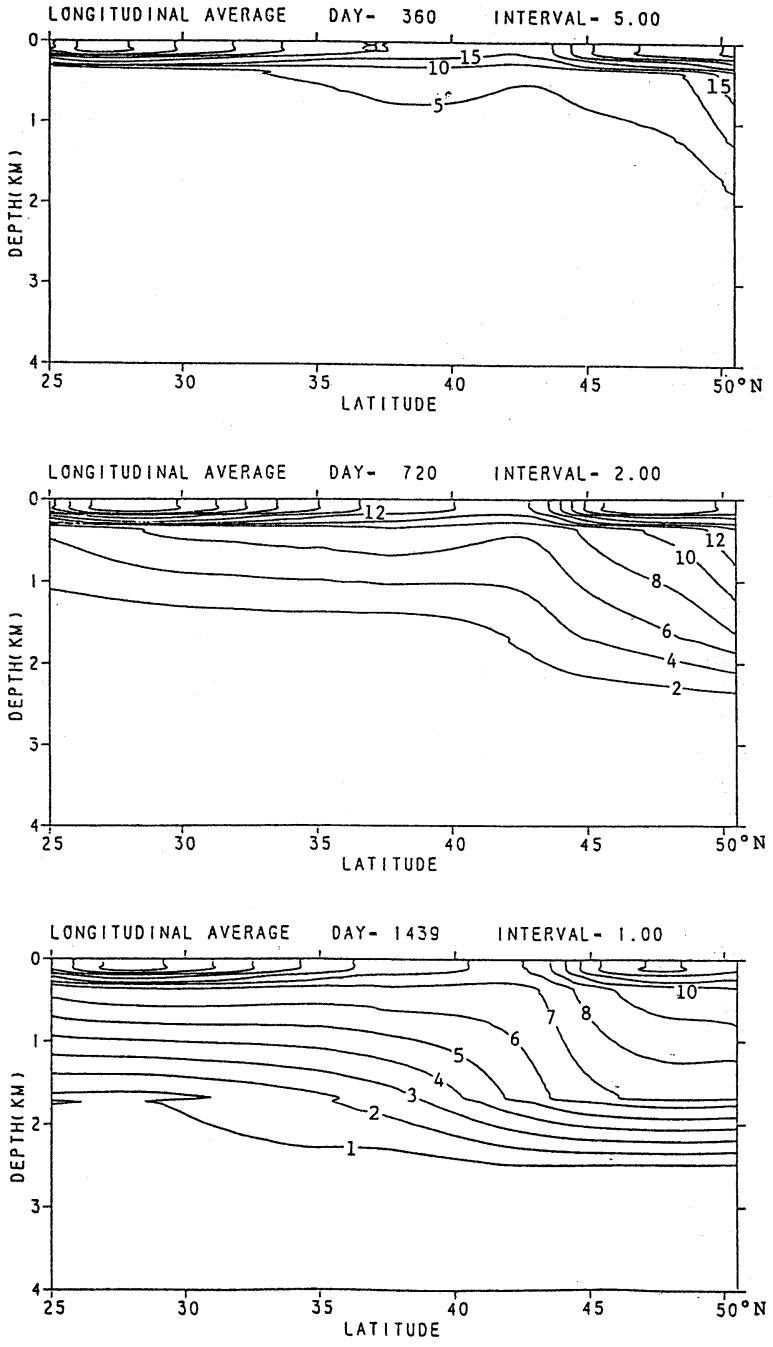

Fig. 12. Vertical-latitude distribution at days 360 (top), 720 (middle) and 1440m (bottom) in Case 1a.

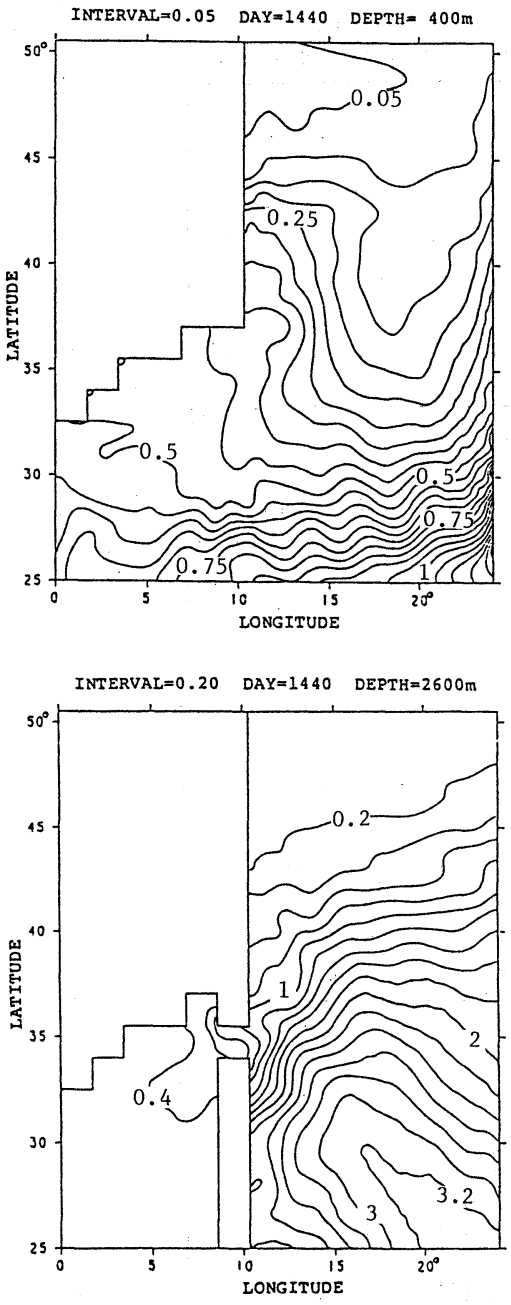

Fig. 13. Isopleths at depths of 400m and 1600m at day 1440 in Case 2e.

3.05 at a depth of 1600m. It is located at 26°N, 20°E, southeast of P. At a depth of 400m, it appears far east, at the southeastern corner. The pattern of isopleths at each layer is not very different from that at day 1440 shown in Fig.13.

The distribution at day 1440 shows that the ridge almost blocks the westward dispersion in the bottom layer. Because there is no strong sinking along the western side of the ridge, dispersion into the deep layer west of the ridge takes place only through a gap between the northern and southern branches of the ridge, but the gap is not an effective pathway.

The maximum concentration is not seen at the location of P anymore at a depth of 2600m, but it is at the southeastern corner at depths of 400m, 1600m and 2600m, and near the western coast at a depth of 80m as at day 720.

Figure 14 shows the longitudinal average at days 360, 720 and 1440. Upwellling in low latitudes gives rise to the upward dispersion from the bottom source. Then, northward flows in upper layers, particularly in the western boundary region, give rise to the northward dispersion. In addition to this pathway, a direct northward pathway is effective in the bottom layer.

5.2 Case 2a

At day 720, the maximum concentration is 9.0 at a depth of 2600m and 1.15 at a depth of 1600m, 0.18 at a depth of 400m and 0.05 at a depth of 80m to be compared with 5.5, 3.05, 0.84 and 0.18, respectively, in Case 2e. Because the upward dispersion is slower in Case 2a, the concentration remains higher in the source region, and lower in the upper layers.

Figure 15 shows isopleths at day 1440. Although the isopleths are smooth, free from mesoscale fluctuations compared with Case 2e, the general pattern of them are similar to each other except at the source region at the bottom layer. Isopleths are mostly closed curves in Case 2a, but not so in Case 2e. The maximum concentration is 4.8 at 2600m, 1.5 at 1600m, 0.45 at 400m and 0.16 at 80m to be compared with 3.2, 2.7, 1.2 and 0.46, respectively, in Case 2e. This confirms slower upward dispersion than in Case 2e. Figure 16 shows the average over the parallel of latitude at days 360, 720 and 1440. Comparison with Case 2e (Fig.14) shows that the mesoscale eddies enhance the vertical dispersion rather than the horizontal dispersion. Slow upward dispersion in Case 2a brings about a sharper vertical gradient of concentration

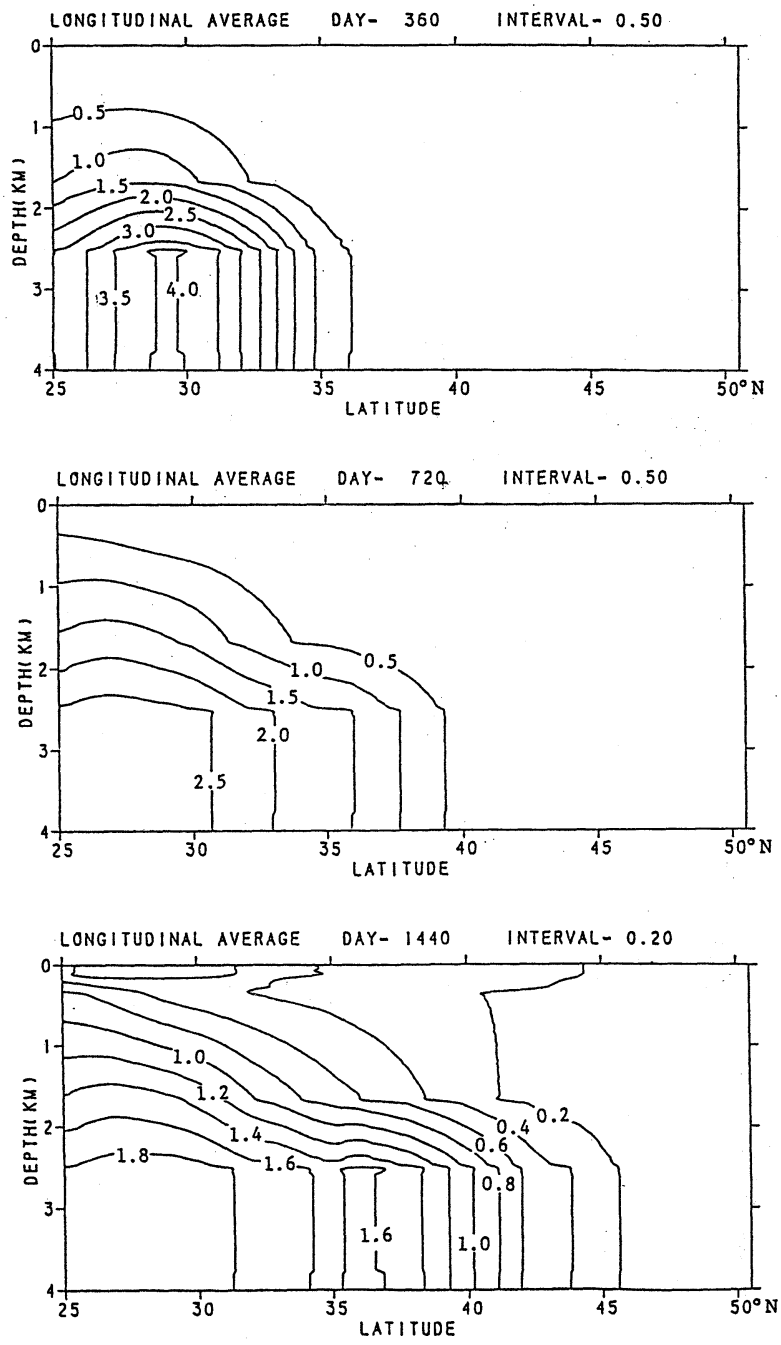

Fig. 14. Vertical-latitude distribution at days 360 (top), 720 (middle) and 1440 (bottom) in Case 2e.

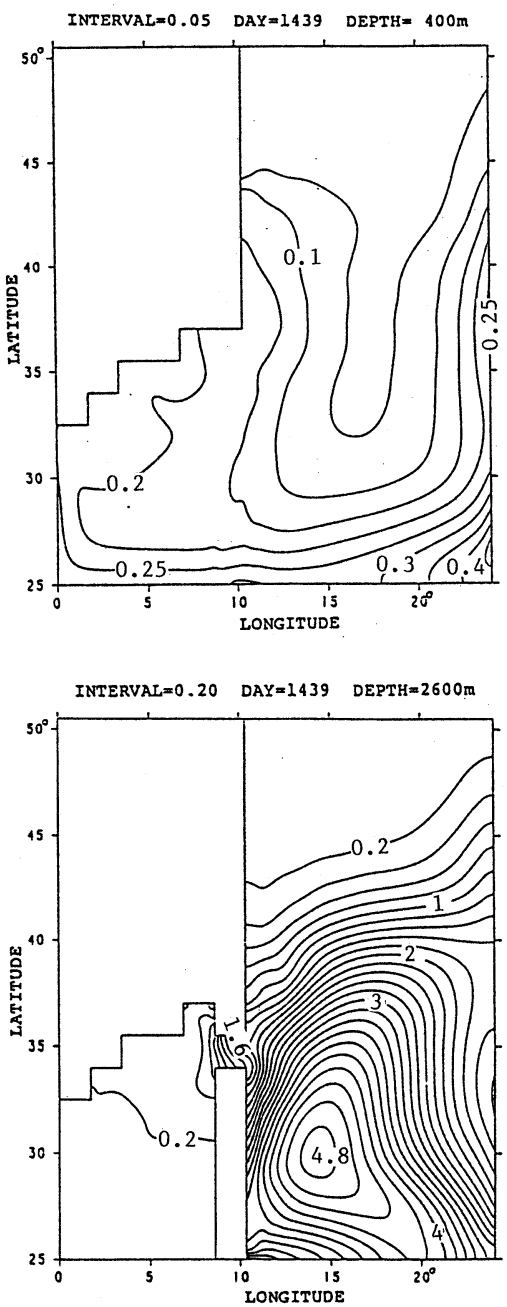

Fig. 15. Isopleths at depths of 400m and 2600m at day 1440 in Case 2a.

between the bottom and upper layers than in Case 2e.

6. Layer-average downward and upward dispersion

The downward dispersion in Cases 1e and 1a is shown in Figs.17 and 18 in terms of the average and total amount of C in each layer. Layer 1, the uppermost layer, is 240m thick, layer 2 is 760m thick, layer 3 is 1100m thick and layer 4 is 1900m thick. In both cases, the average and the total amout in the surface layer monotonically decrease with time and those in the bottom layer monotonically increase with time, whereas those in layers 2 and 3 first increase and then decrease with time. This implies that C becomes excessive in a sense in thin layers 2 and 3 in a transition stage before the dispersion into the thick bottom layer is fully developed.

Apparently the final steady state is reached in shorter time in Case 1e than in Case 1a. Table 1 tabulates the time required for the average concentration in each layer to reach 95 or 105% of the final uniform value (3.02 in Case 1e and 2.98 in Case 1a), and the ratio of the time in Case 1a to that in Case 1e. The mean ratio 2.11 confirms the striking effect of the mesoscale eddies.

Figures 19 and 20 show the upward dispersion in Cases 2e and 2a in the same way. In both cases, both average and total amount in each of the three upper layers monotonically increase with time. Contrary to Cases 1e and 1a, there is no stagnation in layers 2 and 3, because the thickness of the layer decreases upward, the advection is stronger in the upper layers and the source is located in the bottom layer.

Table 2 gives the time required for the average of C to reach to 95 or 105% of the final value (0.923 in Case 2e and 0.918 in Case 2a), and the ratio of the time in Case 2a to that in Case 2e. The mean ratio is 1.85. In these cases, too, the time for the complete dispersion is reduced by about half by the effect of mesoscale eddies.

It takes about 15 years in Cases 1e and 2e, and about 30 years in Cases 1a and 2a to reach the almost complete dispersion where the concentration ranges between 95 and 105% of the final value. The complete dispersion requires, however, about 30 years in the former cases and about 50 years in the latter cases as shown in Figs.17 to 20.

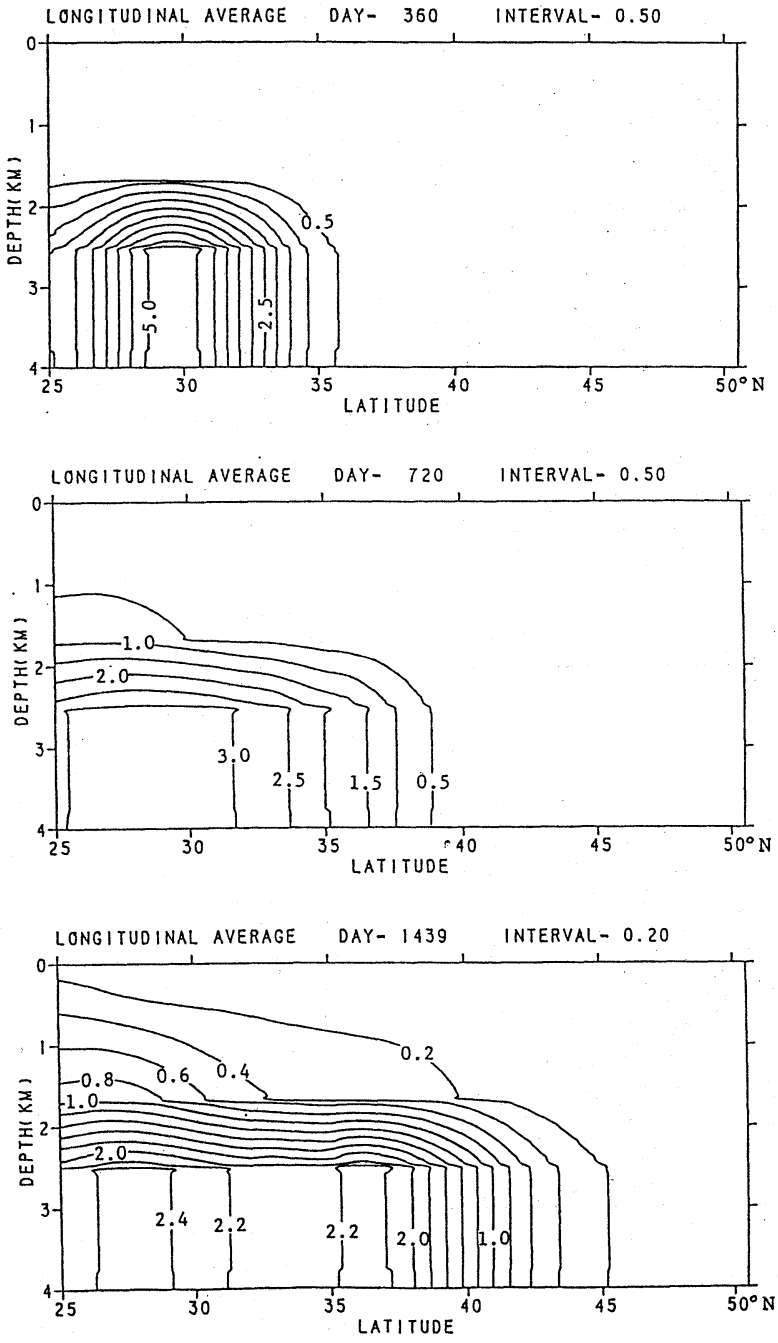

Fig. 16. Vertical-latitude distribution at days 360 (top), 720 (middle) and 1440m (bottom) in Case 2a.

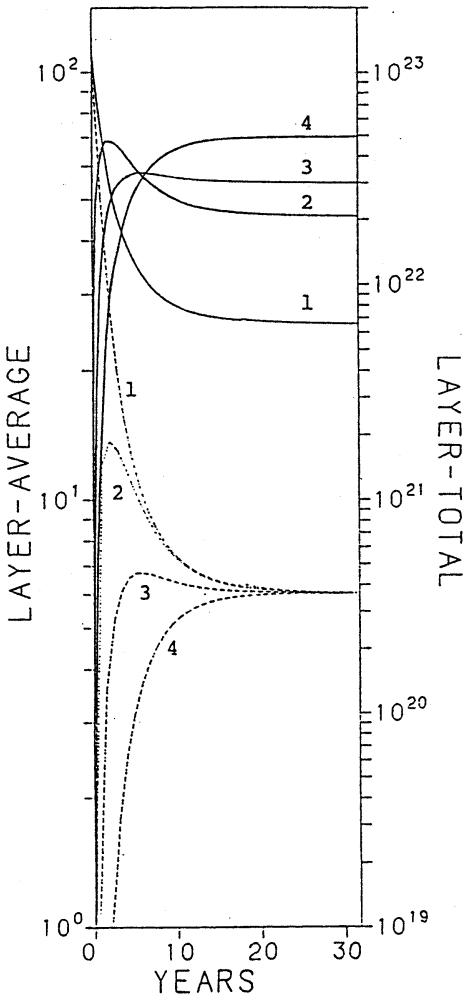

Fig. 17. Average and total amount of C in each layer as a function of time in Case 1e. Solid curve for the total amount, and broken curve for the average. Numerals alongside the curves refer to the layer numbers; 1 to the uppermost layer and 4 to the lowermost layer.

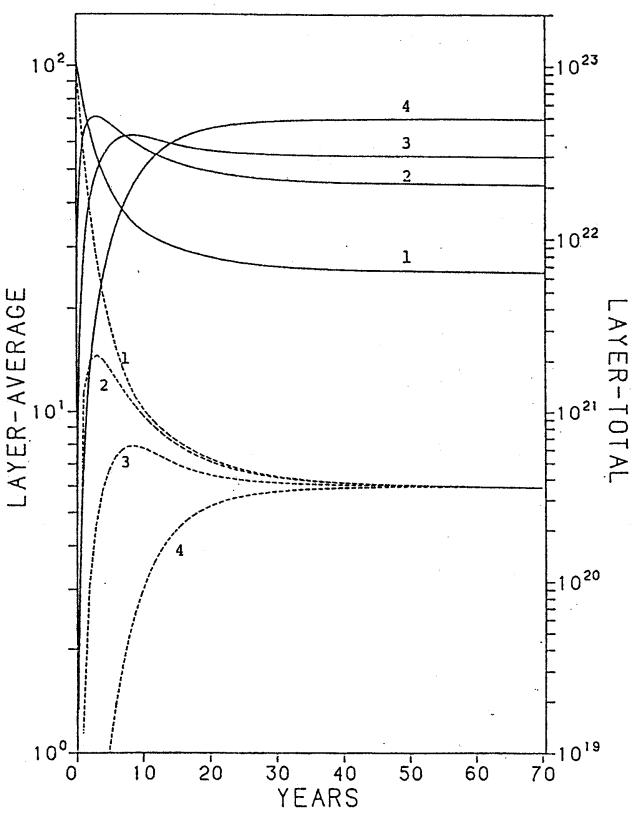

Fig. 18. Same as Fig.17 except for Case 1a.

7. Concluding remarks

The above results are summarized as follows.

(1) Tracers initially given to the whole surface of the model ocean are transported by the general circulation first northward in surface waters and then downward at high latitudes, which is in qualitative agreement with observations.

(2) Tracers initially given to a bottom area east of the meridional ridge are dispersed in both horizontal and vertical direction. Its westward dispersion in the bottom layer is obstructed by the ridge, while the isopleths of tracer concentration in upper layers west, above and east of the ridge do not seem to reflect the presence of the ridge. The mesoscale eddies enhance the vertical dispersion rather than the horizontal dispersion in the bottom layer. Although the discussion on the mesoscale eddies themselves is out of the scope of the present study, it might be remarked that, approaching the ridge, the mesoscale eddies do not shrink vertically to get over it.

(3) To reach the complete dispersion in both cases (downward dispersion from the surface source, and upward dispersion from the bottom source), it takes about 30 years in the mesoscale eddy field and about 50 years in the time-average field. The mesoscale eddies significantly enhance the dispersion over the whole ocean basin.

It might be parenthetically noted that, as to

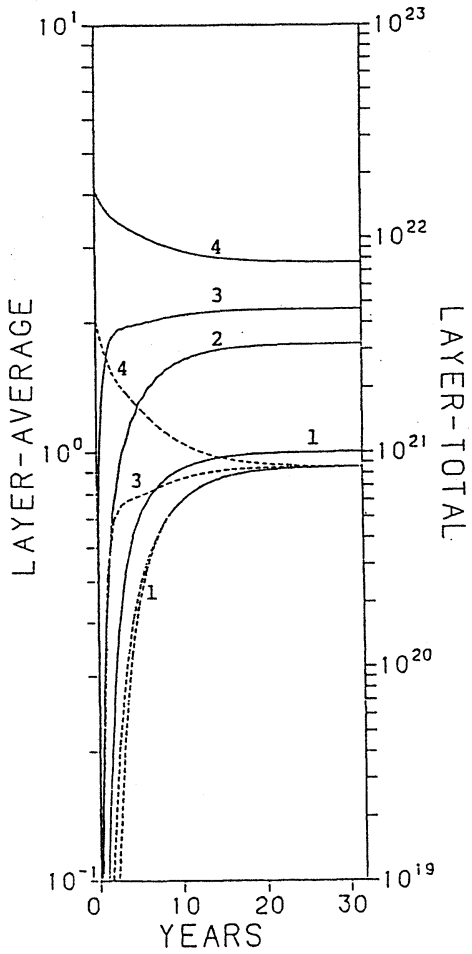

Fig. 19 Same as Fig. 17 except for Case 2e.

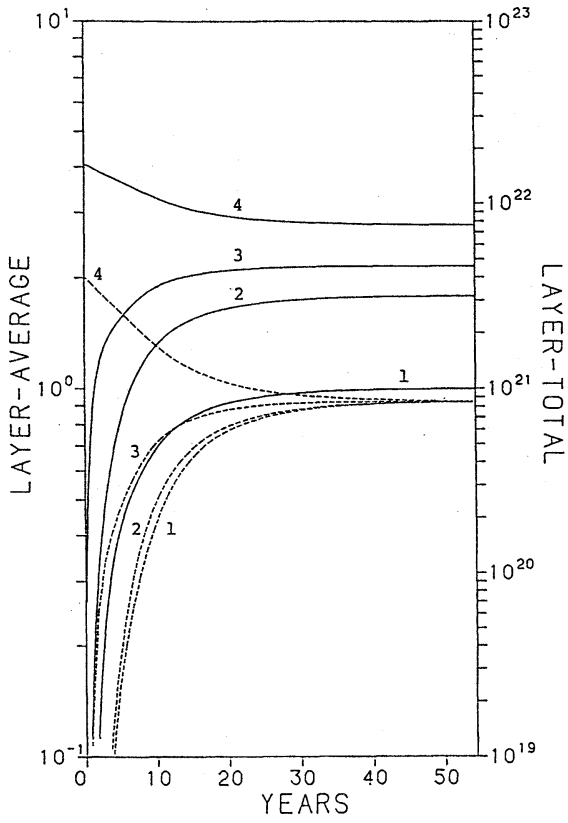

Fig. 20 Same as Fig. 17 except for Case 2a.

Table 1. Time (in years) required for the average concentration in each layer to reach to 95 or 105% of the final value in Case 1e (E) and 1a (A), and the ratio A/E.

Layer	1	2	3	4	mean
E (Case 1e)	16.4	15.9	11.0	13.4	
A (Case 1a)	34.7	33.5	25.0	26.0	
A/E	2.12	2.11	2.27	1.94	2.11

Table 2. Same as Table 1 except for Case 2e and Case 2a.

Layer	1	2	3	4	mean
E (Case 2e)	15.5	15.5	11.0	14.6	
A (Case 2a)	29.9	28.4	19.7	26.9	
A/E	1.93	1.83	1.79	1.84	1.85

dynamically active tracers, both horizontal and vertical heat transport are, if averaged over the vertical or horizontal cross-ocean section, little affected by mesoscale eddy activity (HAN, 1975; TAKANO, 1982).

A shortcoming of the present study is that the model ocean basin is very small; its volume is 1.77×10^7km^3, only 1.3% of the volume of the world ocean and 2.4% of the volume of the Pacific Ocean (72.4×10^7km^3). The time required for the complete dispersion in the model ocean is about 30 years (Figs.17 and 19), while the turnover time inferred from ^{14}C and others in the real ocean is a thousand of years or longer. The time scale of three-dimensional dispersion might be nearly proportional to the volume of the ocean basin, so that a period of 30 years in the model ocean should be equivalent to 2308 (=30/0.013) years for the world ocean and to 1250 (=30/0.024) years for the Pacific Ocean. These values, about 2300 and 1250 years, are reasonable compared with observations. This is somewhat surprising because the short longitudinal extent of the model ocean may increase the relative importance of the western boundary region where the eddy activity is high, which should turn out to exaggerate the eddy activity and eddy-induced dispersion in the small model ocean compared with the actual large ocean basin. As far as the eddy activity at point P in the simulation is compard with that by observed data, the eddy kinetic energy is at least one order of magnitude stronger than the observed one.

The poor vertical resolution is not capable of simulating the thermocline as sharply as observed, so that the vertical dispersion through the thermocline may not be correctly simulated. Therefore, the dispersion might be unrealistically strong in the numerical model. In addition, the bottom topography cannot be realistically set up, either.

A limited zonal extent of the model ocean might more or less distort high frequency, long Rossby waves, which affects the simulated mesoscale eddy properties.

In these regards, eddy resolving circulation models and dispersion models in larger ocean basins with finer vertical resolution are expected to run in the near future.

Other numerical experiments are carried out by using current velocities obtained with the non-slip condition instead of free-slip condition along the lateral boundary. The mesoscale eddy properties and tracer dispersion do almost not change.

The coefficients of subgrid scale diffusion are taken as small as possible, if large enough to suppress the computational noise and instabillity. The coefficients of eddy diffusion calculated from the simulated velocity and temperature are useful for evaluating whether 10^3m^2/s are small enough or not. The coefficient of eddy diffusion defined in terms of the gradient of time-averages and the correlation between the deviations from the time-averages of velocity components and temperature are calculated at each grid point for the four depths. They are negative at about half of the grid points. Their magnitudes, whether positive or negative, are much larger than 10^2m^2/s for momentum and 10^3m^2/s for heat, which suggests that the diffusion by the mesoscale eddies explicitly dealt with in the present study is much stronger than the eddy diffusion formulated in conventional Laplacian form with coefficients of 10^2m^2/s and 10^3m^2/s. This is also the case of the coefficient of vertical diffusion.

Another paper (YOKAYAMA and TAKANO, 1993) will present results of tracking of particles continuously or instantaneously released from a point source into the mesoscale eddies, which is another way to understand the effect of mesoscale eddies.

References

Atomic Energy Management Center (1986): Report of a preoperational survey of a proposed area for ocean disposal of radioactive wastes ——low-frequency water motion ——. 270pp. (in Japanese)

FRIEDRICH, H. and S. LEVITUS (1972): An approximation to the equation of state for sea water, suitable for numerical ocean models. J. Phys. Oceanogr., **2**, 514–517.

HAIDVOGEL, D, A.ROBINSON and C. ROOTH (1983): Eddy-induced dispersion and mixing. *in* Eddies in Marine Science (edit. by A. Robinson), 481–489, Springer-Verlag, Berlin, Heidelberg.

HAN, Y.J. (1975): Numerical simulation of mesoscale ocean eddies. Ph. D. thesis, Dept. Mete-

orol., UCLA, 153pp.
IMAWAKI, S. and K.TAKANO (1982): Low-frequency eddy kinetic energy spectrum in the deep western North Pacific. Science, **216**, 1407-1408.
OSTLUND, H. and K. BRESCHER (1982): GEOSECS Tritium. Univ. of Miami, Tritium Lab., Data Rept. No.12.
TAKANO, K. (1974): A general circulation model for the world ocean. Tech. Rept. No.8, Num. Simul. Weather and Climate, Dept. Meteorol., UCLA, 46pp.
TAKANO, K. (1982): Grid-size dependency of the meridional heat transport in a numerical model of an ocean. Atmos.-Ocean, **20**, 258-267.
YOKOYAMA, K. and K. TAKANO (1986): Relationship between the grid size and the coefficient of subgrid-scale diffusion in a finite difference advection-diffusion equation. La mer, **24**, 128-129.
YOKOYAMA, K. and K. TAKANO (1993) : Particle tracking in a mesoscale eddy field in an ocean. La mer, **31**, 75-86.

中規模うずによる受動追跡子の分散

横山恵子・高野健三

要旨：中規模うずが受動追跡子の分散に及ぼす影響を調べるための数値実験を行う。追跡子は移流と拡散によって広がる。流速は，4層の，うず分解大循環モデルから与えられる。海は緯度方向には25.0°Nから50.5°Nまでひろがる。経度方向のひろがりは24.8°である。南北方向に走る海嶺（海底からの高さは1900m）を除いて海の深さは一定（4000m）であり，北西太平洋の一部に似た形になっている。格子間隔は，緯度について0.375°，経度について0.43°である。三次元の移流・拡散方程式を時間積分して，追跡子の分布を80m，400m，1600m，2600mの深さで計算する。初期条件として，(i) 海面全体をおおう均一分布（瞬間面源）と (ii) 海底の一点だけの分布（瞬間点源）を与える。うずを含む流速場と，時間平均をとってうずを除いた平均流速場を使い，結果をくらべる。(i)，(ii) とも分散はうずによっていちじるしく速くなる。海全体に均一にひろがる（完全分散）までの時間は約30年で，平均流速を使うと約50年になる。完全分散に要する時間は海の体積にほぼ比例するだろうから，30年という長さは，世界中の海については約2300年，太平洋については約1250年に相当し，妥当な値になる。

La mer 31: 79–90, 1993
Société franco-japonaise d'océanographie, Tokyo

Particle tracking in a mesoscale eddy field in an ocean*

Keiko YOKOYAMA**,*** and Kenzo TAKANO**

Abstract: Particles released instantaneously or continuously from a point source are tracked in a velocity field simulated with a prognostic, four-level, eddy resolving ocean circulation model. The model ocean extending from 25.0°N to 50.5°N in latitude and over 24.8° in longitude may be considered as a portion of the western North Pacific. Its depth is 4000m except at a ridge 1900m high. The grid size is 0.375° in latitude and 0.43° in longitude. Results with the velocity field comprising mesoscale eddies are compared with those with the time-average velocity field. For tracking over the whole ocean basin, particle trajectories are, in some cases, quite different from those governed by the time-average velocity field. For local tracking, the effect of simulated mesoscale eddies is compared with that obtained with velocity data by arrayed current meters in terms of the time required for a particle to cover a certain distance from a point source. Agreement is good.

1. Introduction

In a previous paper (YOKOYAMA and TAKANO, 1993, hereafter referred to as YT), numerical experiments were carried out on the effect of mesoscale eddies on the passive tracer dispersion in a model ocean by solving an advection-diffusion equation. The velocity data necessary to calculate the advection were supplied from a four-level, eddy resolving general circulation model driven by a surface wind stress and a surface heat flux.

The model ocean extends from 25.0°N to 50.0°N in latitude and over 24.8° in longitude, and is 4000m deep except at a ridge 1900m high. Its geometry is a rough copy of a portion of the western North Pacific. The grid size is 0.43° in longitude and 0.375° in latitude. The horizontal components of velocity are defined at depths of 80, 400, 1600 and 2600m. The vertical component of velocity is defined at depths of 240, 1000 and 2100m. The simulated velocity data are available for about 80 years.

The present paper describes tracking of particles over the whole ocean basin and a local area of limited extent. As YT, this is done in the framework of a preoperational survey for the ocean bottom disposal of low-level radioactive wastes, together with a long term current measurement from 1978 to 1985.

2. Numerical experiments

Three experiments are carried out; one is for the basin-wide tracking, and the others for local tracking over a limited area. Particles released instantaneously or continuously are assumed to move with surrounding water and tracked in the given velocity field.

The particle location $x(t+\Delta t)$ and $y(t+\Delta t)$ is determined from the location $x(t)$, $y(t)$ at time t by an upcurrent scheme as

$$x(t+\Delta t)=x(t)+u(x(t), y(t))\,\Delta t,$$
$$y(t+\Delta t)=y(t)+v(x(t), y(t))\,\Delta t,$$

where Δt is the time step, u and v are the horizontal (x-, y-) components of velocity at time t. Diffusion is neglected.

2.1 Basin-wide tracking

A similar experiment was done in a smaller ocean in a previous paper (TAKANO and MATSUYAMA, 1979).

The particle trajectory is shown by its three projections on the horizontal, vertical-meridional and vertical-zonal plane.

* Received March 1, 1993
** School of Environmental Sciences, University of Tsukuba, Tsukuba, Ibaraki-ken 305 Japan
*** Present affiliation: NTT Data Communications Systems Corporation, Toranomon, Toyo 105 Japan

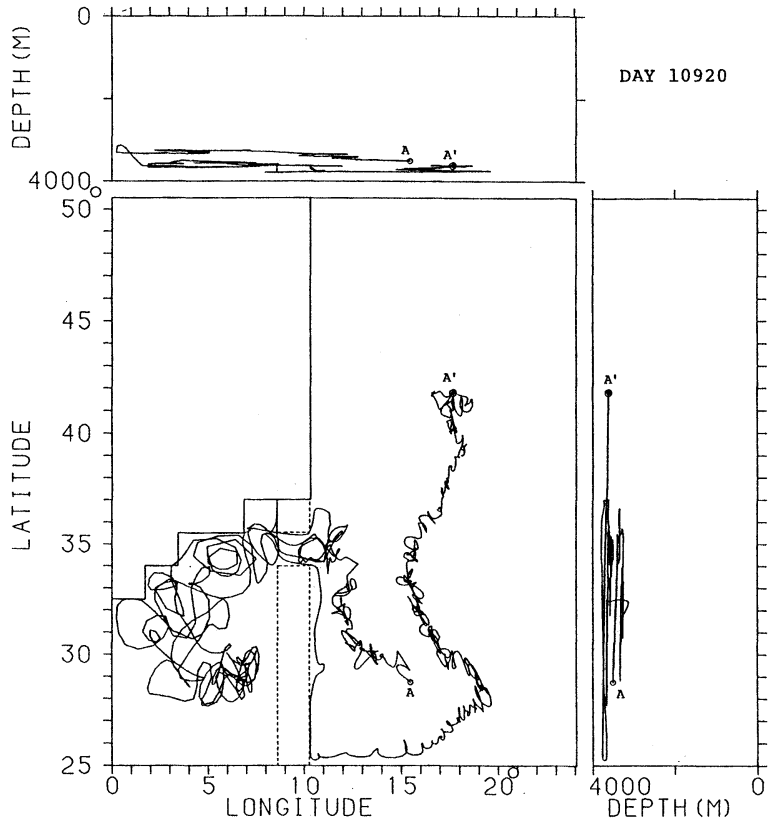

Fig. 1. An example of basin-wide tracking of a particle released from a point source A 3510m deep. The end point is A'. The projection of its trajectory on a horizontal plane is shown on the lower left, the projection on a meridional plane on the lower right, and the projection on a zonal plane on the upper left.

An example is given in Fig.1 for an instantaneous release from a point A. The location of A might correspond with the location of an area proposed by the Japanese government for the ocean bottom disposal of low-level radioactive wastes, which is centered at 30°N, 147°E, about 400km east of the Izu-Ogasawara Ridge and about 500km south of the Kuroshio Extension. One particle released from a point source A at a depth of 3510m is advected in a mesoscale eddy field and reaches a point A' at day 10920 after the release. The successive particle location is calculated by a time step of 12 hours. Since the velocity field supplied from the general circulation model is available every 2.5 days, the velocity field is updated by interpolation every 12 hours. Also linear interpolation in the zonal, meridional and vertical direction applies to get the velocity at a given location. All the successive locations determined at intervals of 5 days are used for plotting.

The particle always remains deeper than 3085m. It goes to the west of the ridge through the gap, and then comes back to the east of the ridge. To the east of the ridge, fluctuations of scales of several tens of kilometers are pronounced, except along the eastern side of the ridge where the mesoscale eddies are not active as shown in YT. To the west of the ridge, such small scale fluctuations are not so remarkable, but scales of 200 to 400km are clearly seen.

Figure 2 gives the trajectory for the same 10920 days in the velocity field averaged over 80 years. Its trajectory is confined into the east of the ridge, where it almost coincides with the trajectory in Fig.1 if the latter is smoothed out. Trajectories of five particles released from A every 25 days are shown in Fig.3 at day 10920

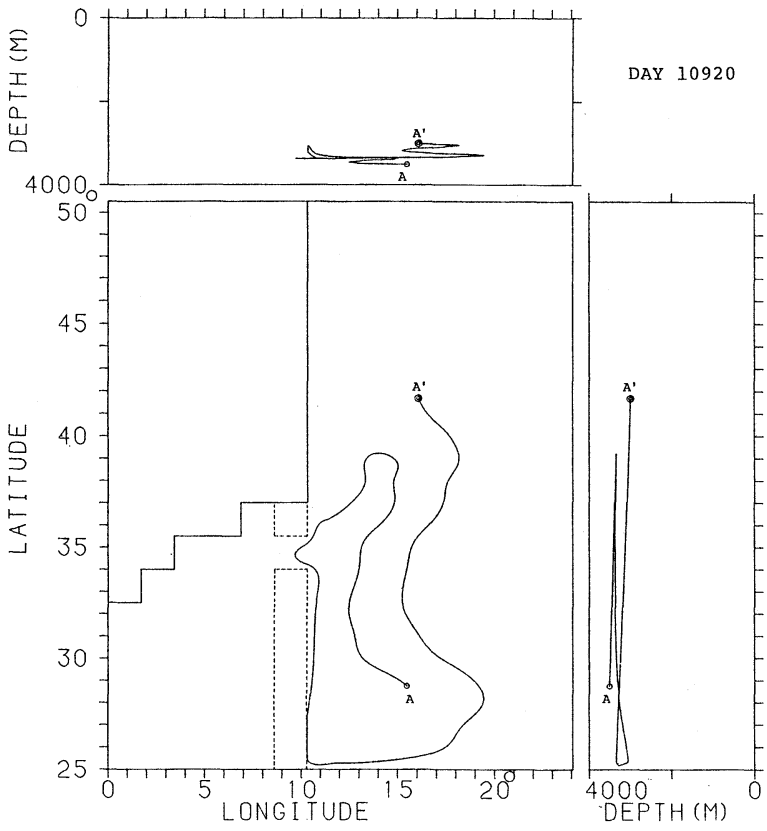

Fig. 2. Same as Fig.1 except for the time-average velocity field.

after the release of the first particle. Two of the five particles including the particle drawn in Fig.1 go to the west of the ridge through the gap. The particle is admitted into the west if mesoscale eddies timely work at the gap. Small scale fluctuations are weak not only in the west of the ridge but also in the notrhern region, which is common to the other experiments of release in the deep layer. Figure 4 shows trajectories of three particles simultaneously released at a depth of 50m. Small scale fluctuations are not so remarkable, because the mesoscale eddies are weaker relatively to the time-average in upper layers than in lower layers, and the greater part of trajectories remain in upper layers. Although they finally penetrate into deeper layers from the northern region, their trajectories are entangled in upper layers, especially in the western region, and not straightforward to the deep layer.

The extent of dispersion depends on the location of the point source, particularly on its depth. If particles are released at a shallower depth, they are dispersed wider, particularly in the vertical, governed by stronger currents. In the case where the source is deeper than the top of the ridge (2100m deep), the ridge effectively obstructs the dispersion between its eastern and western sides; particles approaching the ridge can not get over it and the gap is too narrow.

2.2 Local tracking

Instantaneous release Particles are tracked for an extent of several tens to several hundreds of kilometers. Two-dimensional instead of three-dimensional dispersion is dealt with, because the dispersion takes place in a small area and the horizontal component of the velocity is much greater than its vertical component.

A rectangular frame is set up near the bottom. Particles are released from a point source in this frame, and then advected in either the mesoscale eddy field or the time-average veloc-

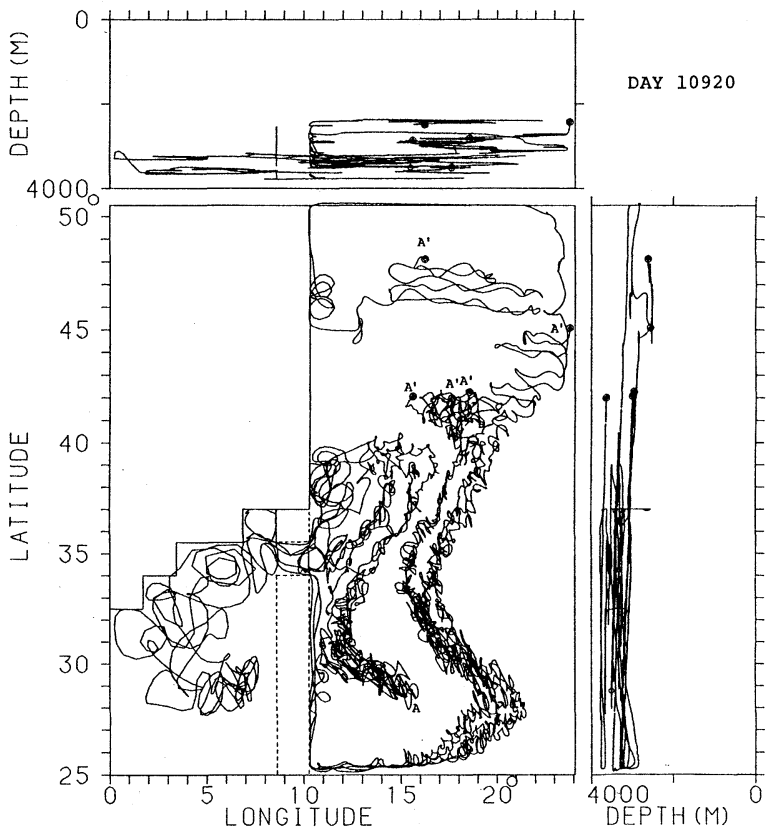

Fig. 3. Trajectories of five particles released from A every 25 days. The locations 10920 days after the release of the first particle are denoted by A'.

ity field, and finally flow out of the frame. The residence time is defined as the time elapsed from the release to flowing out, and denoted by *Re* when the particles are advected in the mesoscale eddy field, and by *Ra* when advected in the time-average velocity field. Particles once flowing out of the frame may flow back into the frame later on, but such a return is ignored in calculating *Re* and *Ra*. The residence time, either *Re* or *Ra*, depends on the frame size as well as the flow velocity. Ten frames of different size are set up at A shown in Fig.1. The side length L is about 42, 84, 167, 250, 290, 330, 380, 420, 470 and 520km.

If the side length of the frame is much longer than the predominant space scale L^* of velocity fluctuations, the velocity fluctuations have no important effect on the residence time, which is determined primarily by the time-average velocity. If the side length is comparable to L^*, the residence time will be approximately proportional to the frame area L^2. If the side length is little shorter, it will be proportional to L^n $(1<n<2)$. If the side length is much shorter, it will be proportional to L. The mesoscale eddies are the most important fluctuation component. Therefore, if the frame size is comparable to the scale of mesoscale eddies, then

$$Re \propto L^2, \quad Ra \propto L, \quad Re/Ra \propto L,$$

and, if the frame size is a little smaller than the scale of mesoscale eddies, then

$$Re/Ra \propto L^{n-1}.$$

Continuous release One particle is released every 25 days for 3.6 years. In total, fifty-one particles are released. The velocity data for these 3.6 years are arbitrarily chosen among the available data for 79.2 years. There is almost no secular variation in the data. For example,

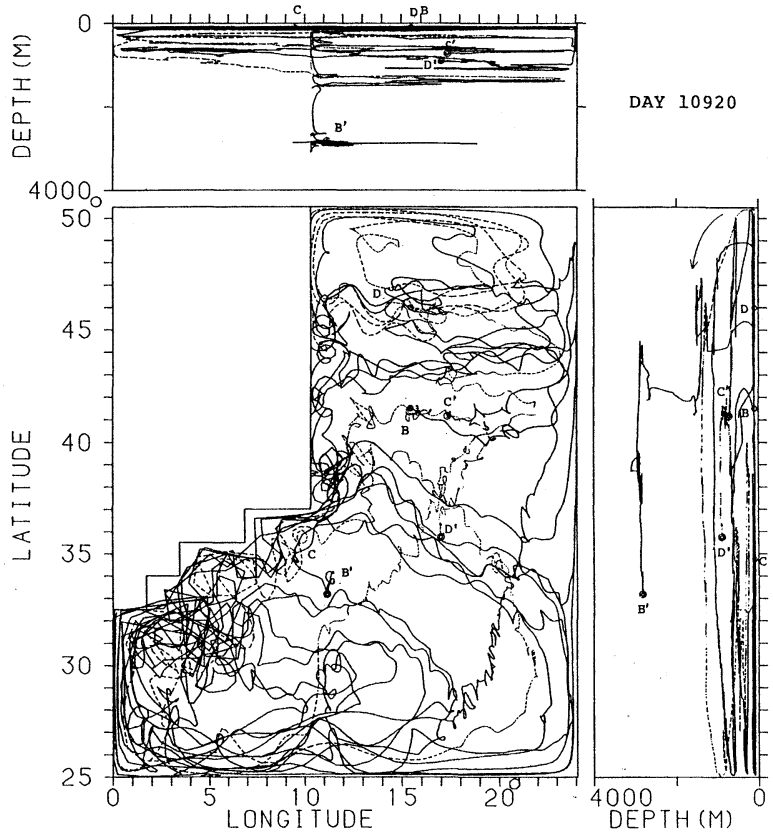

Fig. 4. Trajectories of three particles released from point sources B, C and D (depth: 50m). Double open circles B', C' and D' denote their locations at day 10920.

the simulated data for 79.2 years are divided into three parts for an equal period of 26.4 years. The time-average of u at a depth of 2600 m at Point A in Fig. 1 is −3.7 cm/s for the first part, −4.0 cm/s for the second part and −3.9 cm/sfor the last part. The time-average of v is 2.9 cm/s, 3.0 cm/s and 3.0 cm/s, respectively. There is almost no difference in the power spectra between these three parts, either.

Figure 5 shows stick diagrams of the deviations from the time-averages of the barotropic and baroclinic components at Point A for a period of 2580 days arbitrarily chosen. Although fluctuations of periods of some hundreds of days clearly appear in both components, those of the barotropic component are more energetic. The time-averages of the eastward and northward barotropic component are −0.48 cm/s and −0.23 cm/s, respectively, which are much smaller than the deviations. Those of the baroclinic component are 0.04 cm/s, −2.2 cm/s at a depth of 80 m, −0.50 cm/s, −0.61 cm/s at a depth of 400 m, 0.35 cm/s, −0.05 cm/s at a depth of 1600 m, and −0.01cm/s, 0.55 cm/s at a depth of 2600 m, which are smaller than the deviations. The time scales of the barotropic component are considerably shorter than those of the baroclinic component. The fluctuation of the baroclinic component at a depth of 80 m is well correlated with that at a depth of 400 m. The fluctuation at a depth of 1600 m looks to be correlated with that at a depth of 2600 m, but the correlations between fluctuations at the upper two layers and lower two layers are poor, as already pointed out in YT.

Figure 6 shows power spectra calculated with 79.2-year data at a depth of 2600m at A. There are predominant periods of about 100 days.

An example of the trajectories of 51 particles is shown in Fig. 7 for a frame of about 84km ×

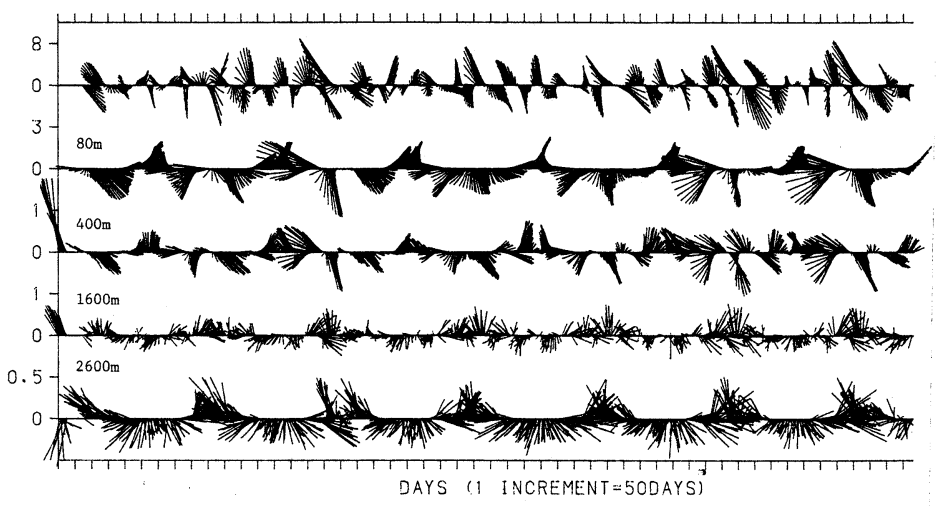

Fig. 5. Stick diagrams of the deviations of the barotropic (top diagram) and baroclinic (lower diagram) components of velocity from their time-averages at A. Units of numbers in ordinate: cm/s.

84km. The velocity data are different from those drawn in Fig. 5. The time elapsed from the first and last particle release is 3.6 years, which is long compared with the time scale of the mesoscale eddies. Trajectories in a larger square are shown in Fig. 8. The velocity data are the same as those used in Fig. 7. As expected, the trajectory has a tendency to be a curve rather than a straight line with increasing frame size.

If the time-average velocity is used, all the trajectories become nearly straight lines irrespective of the frame size.

Figure 9 gives the ratio Re/Ra for ten frames of different size of which the side length is represented in terms of the number of grid boxes N. Since the grid size is 0.375° in latitude and 0.43° in longitude, an increment of N is equivalent to about 40km. Two periods are arbitrarily chosen from 79.2-year time-series of velocity: one is the period used for Fig. 8 and the other is a period 9030 days later. Fifty-one particles are released in each data set. The average of 51 values for Re/Ra in the former are shown by open circles and the averages in the latter by solid circles. The dispersion is indicated by a line segment for each. Two results are should have been exactly at $N=1, 2, , 16, 18$, though both are a little spaced only for the sake of presentation. The upper panel is the result in the velocity field obtained with the free-slip condition at the lateral boundary, and the lower panel the result with the non-slip boundary condition.

For N smaller than 6 (about 240km), the vertical component of the velocity and the variation of the zonal side length with latitude are neglected. Although the dispersion range shown by a line segment is fairly wide, it gets narrower with increasing frame size. The average of the 51 values increases almost in proportion with the frame size for N smaller than 8 or 10 (320km to 400km), and becomes 0.8 to 0.9 irrespective of the frame size for larger frame sizes, as expected from the above simple analysis.

Table 1 summarizes the results shown in Fig. 9. The average residence time Re and Ra are tabulated with the ratio Re/Ra for ten frames of different size. The ratio Re/Ra for a given frame does almost not depend on the dynamical condition at the lateral boundary.

According to the above analysis, we have, with a constant of proportionality, d, for the frames of $N=1$ and 2,

$0.18=d\times 1^{n-1}$, $0.27=d\times 2^{n-1}$, which give
$1.5=2^{n-1}$, so that $n=1.6$ for the free-slip condition, and
$0.17=d\times 1^{n-1}$, $0.22=d\times 2^{n-1}$, which give

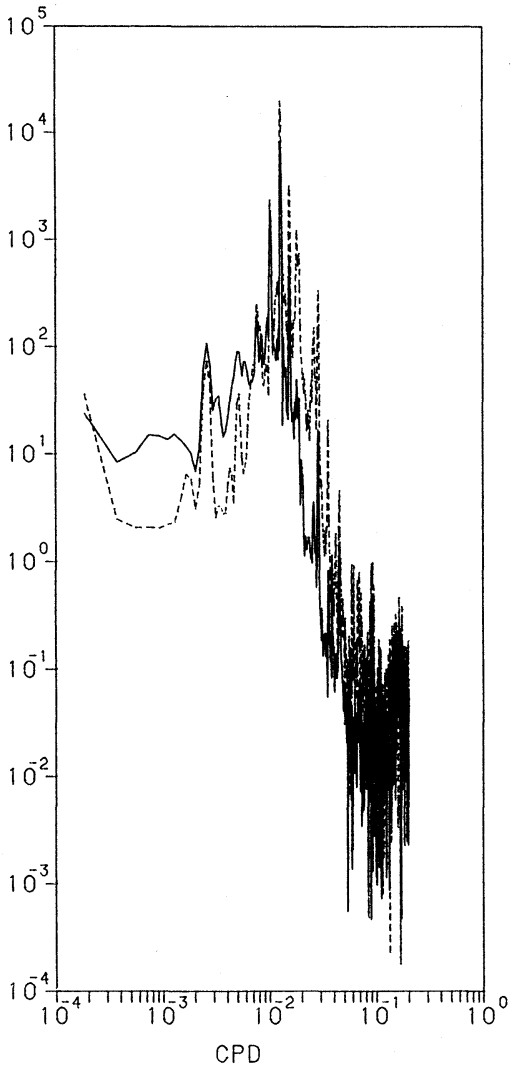

Fig. 6. Power spectra of the eastward (solid curve) and northward (broken curve) component of velocity at a depth of 2600m at A.

$1.3=2^{n-1}$, so that $n=1.4$ for the non-slip condition.

Two values 1.6 and 1.4 will be discussed later in the light of tracking experiment with observed data.

3. Particle tracking by observed velocity data

Seven-year current measurements were done around 30° N, 147° E (IMAWAKI and TAKANO, 1982; Atomic Energy Management Center, 1986).

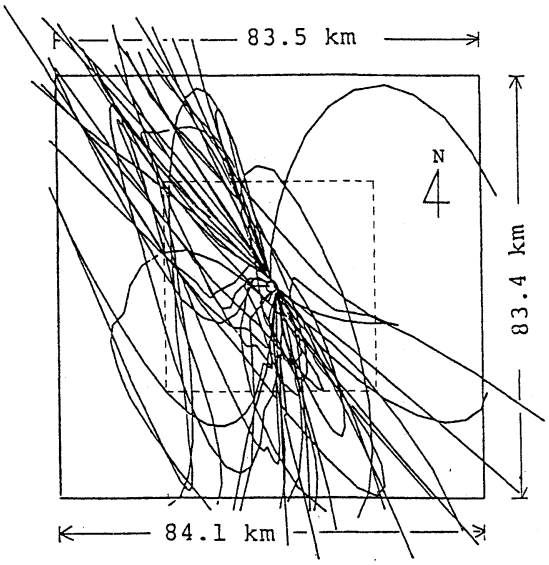

Fig. 7. Trajectories of 51 particles released every 25 days in a frame of about 84km × 83km. The side length of the inner frame is about 42km.

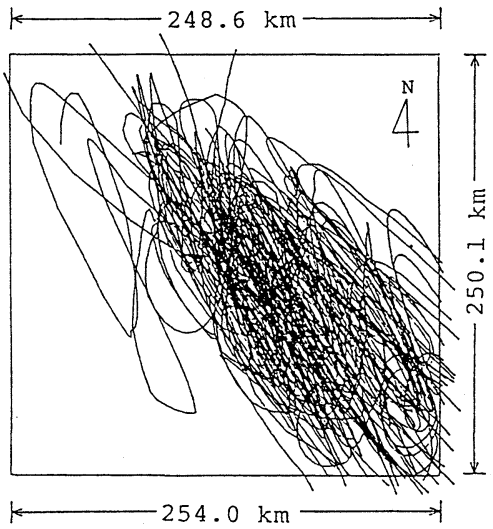

Fig. 8. Same as Fig.7 except for a frame of about 250km × 250km.

Two extensive measurements were done, the first one with a five-current meter array from May 1983 to October 1983 and the second one with an eleven-current meter array from July 1984 to July 1985, of which the locations are shown in Fig.10. Hourly data are obtained in both measurements.

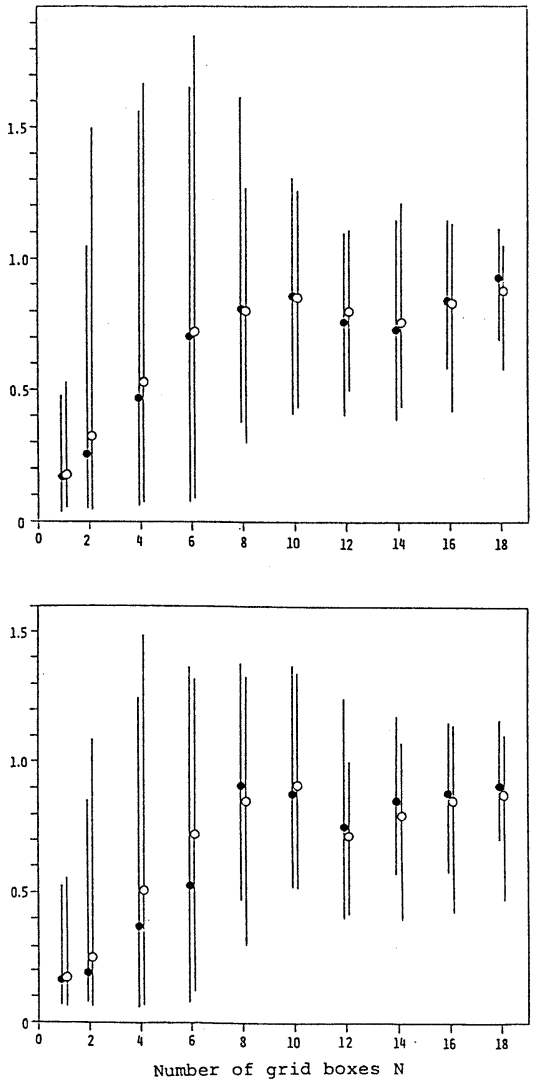

Fig. 9. Ratio Re/Ra. The ranges of dispersion are shown by line segments with the averages denoted by open circles (first period) and solid circles (second period). Velocity field with the free-slip condition (upper panel) and the non-slip condition (lower panel) at the lateral boundary.

Fluctuations of hourly data with periods around one day are apparent at all the stations, but their phases are different from each other, indicating that the scales of these fluctuations are mostly small compared with the spacing between two neighboring stations. This will be also shown later by particle trajectories. Mesoscale eddies clearly appear on the daily average. Contrary to hourly data, fluctuations are almost in phase over all the stations.

The diurnal, semi-diurnal tides and/or inertia oscillations appear in high frequency ranges in power spectra. The theoretical inertia periods at the mooring sites (29°35.2′ N to 30°15.6′ N) are 23.81 to 24.30 hours. The mesoscale eddies are predominant in lower frequencies.

3.1 Tracking with data from July 1984 to July 1985

It is assumed that one particle is released every five days from a point source located at the center of the frame of 70.7km × 70.7km shown by solid lines in Fig.10. Particles are advected by the daily mean velocity at a depth of 4000m. The total number of particles released during the observation period is 67. Letters B, V, N and R at the four corners of the frame in Fig. 11 refer to the stations shown in Fig.10. The trajectories are more scattered than those in Fig. 7. The time elapsed from the release of the first particle to the release of the last particle is 1250 days in Fig. 7, which is much longer than 330 days in Fig. 11. The number of particles released (51 in Fig.7) is only a little less than 67 in Fig.11. The trajectories are, however, much more dispersed in almost all directions than in Fig.7. A possible interpretation of this difference in pattern is that the simulated velocity field has no small scale components; the shortest resolvable wavelength is twice the grid size (about 80km).

Figures 12 and 13 give trajectories of particles instantaneously and simultaneously released. Particles in Fig.12 are released 3840 hours after the beginning of the measurement. Particles in Fig.13 are released 40 days after particles drawn in Fig.12. Hourly data are used instead of daily mean velocities. Small loops showing clockwise rotation reflect diurnal, semidiurnal tides and inertial oscillations, which are clearly seen in stick diagrams by the hourly data and power spectra (not shown here). In Fig. 12 four particles flow to the northeast, while one particle flows to the southwest. In Fig.13, five particles flow almost in the same direction (to the west-northwest). The residence time is much longer in Fig.12 than in Fig.13, which also indicates variability of the current for a period of 40

Table 1. Average residence time *Re*, *Ra* (in days) and ratio *Re*/*Ra* for ten frames of different size. The side length of frame is represented by the number of grid boxes *N*. The velocity fields used for the upper and lower panels (a and b) are obtained with the free-slip and non-slip lateral boundary condition, respectively.

	N	1	2	4	6	8	10	12	14	16	18
	Re	11.0	27.3	95.1	196	304	423	527	690	835	989
(a)	*Ra*	62.5	100.0	190.0	275	377	492	701	927	1000	1093
	Re/*Ra*	0.18	0.27	0.50	0.71	0.81	0.86	0.75	0.74	0.84	0.90
	Re	11.8	22.9	86.2	181	347	461	613	768	885	991
(b)	*Ra*	70.0	105.0	200.0	288	392	511	829	924	1015	1102
	Re/*Ra*	0.17	0.22	0.43	0.63	0.89	0.90	0.74	0.83	0.87	0.90

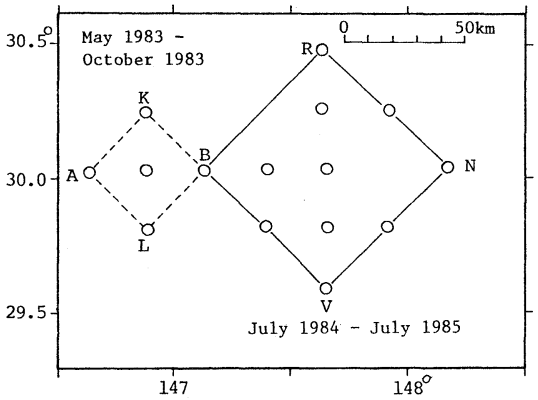

Fig. 10. Five-current meter array and eleven-current meter array at a proposed area for the ocean bottom disposal of low-level radio-active wastes. Also are shown rectangular frames used for particle tracking experiments.

days.

3.2 Tracking with data from May 1983 to October 1983

Figures 14 to 16 are drawn with data from May to October 1983. The period of measurement is shorter, so that only 30 particles are released. The time elapsed from the release of the first particle to the release of the last particle is 145 days, while it is 125 days for the numerical experiments. As in Fig. 11, the trajectories in Fig. 14 are scattered in almost all directions compared with Fig. 7 (inner frame). Since the frame size is much smaller than the mesoscale eddies, most of the trajectories are straight lines rather than curved lines except small loops by tidal and inertia oscillations. These features are also seen in Figs. 15 and 16 for an

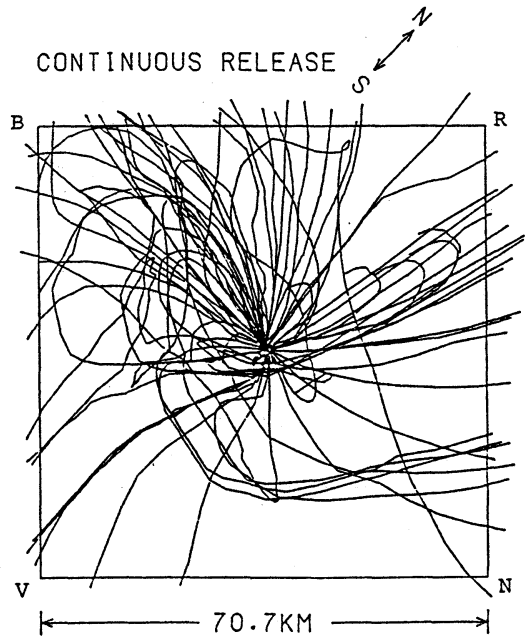

Fig. 11. Trajectories of 67 particles released every five days in the observed velocity field.

instantaneous and simultaneous release. Particles in Fig. 15 are released just at the beginning of the measurement. Patricles in Fig. 16 are released 40 days later. Trajectories in both figures are nearly straight compared with those in Figs. 12 and 13.

The trajectories in the time-average velocity field rotate clockwise from july 1984 to July 1985, but anticlockwise from May to October 1983, which indicates that the velocity field, though averaged over the whole period of the measurement, significantly changes from one measurement to another.

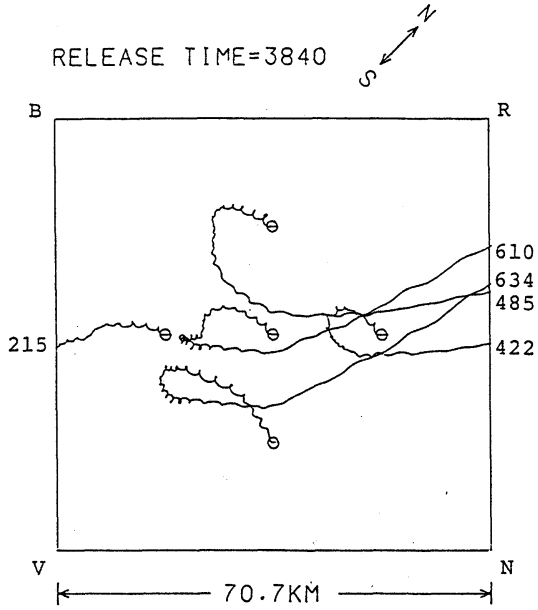

Fig. 12. Trjectories of five particles instantaneously and simultaneously released from five point sources. A numeral at the end of each trajectory denotes the residence time in hours.

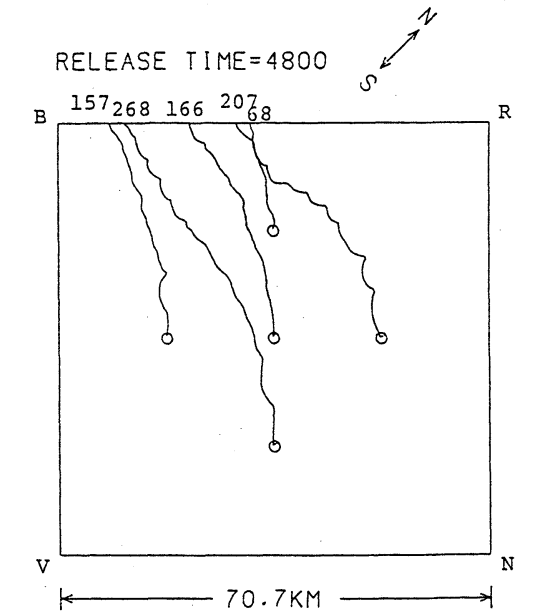

Fig. 13. Same as Fig.12 except for another release time (40 days after those in Fig.12).

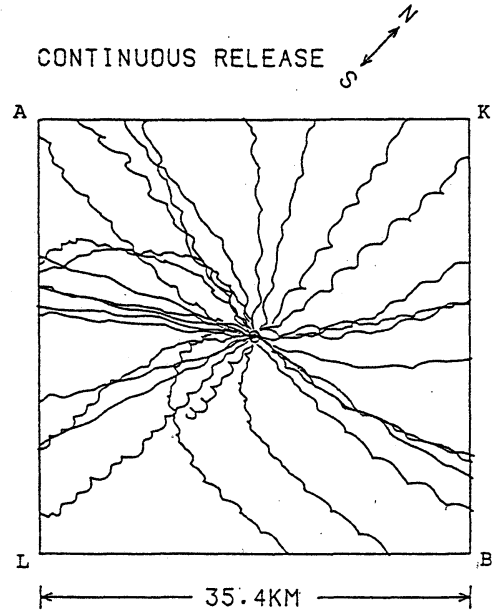

Fig. 14. Trajectories of 31 particles released every five days from May to October 1983.

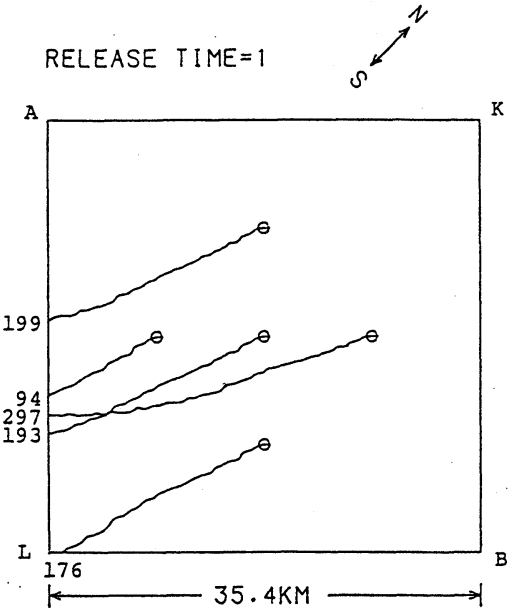

Fig. 15. Trajectories of five particles instantaneously and simultaneously released from five point sources. A numeral at the end of each trajectory denotes the residence time in hours.

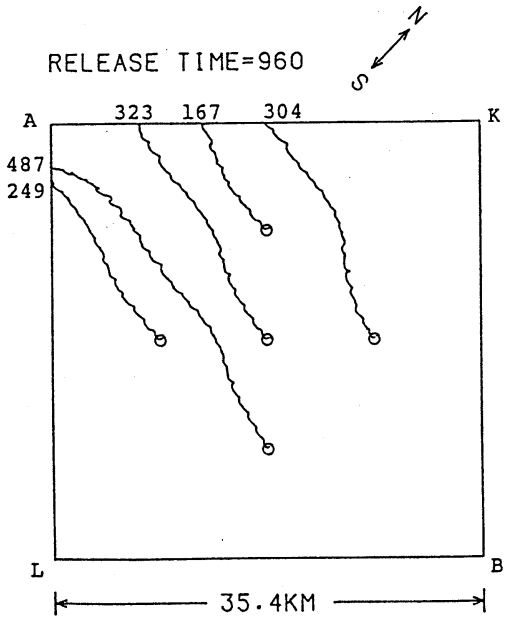

Fig. 16. Same as Fig. 15 except for another release time (40 days after those in Fig.15).

Table 2 tabulates the residence times of 30 and 67 particles. The average of ratio Re/Ra is 0.22 and 0.33, respectively, though the dispersion is fairly large. As mentioned earlier, this ratio should be proportional to L^{n-1}. From $(70.7/35.4)^{n-1}=0.33/0.22$, it follows $n=1.6$, which is equal to the value for interpreting results of the numerical experiment (with the free-slip boundary condition) for frames of size comparable with that set up by the current meter array. The value n depends on both frame size and scale of the velocity field structure, Since the frame size concerned is not so different between the numerical experiment and the observation, the agreement of the n-value indicates the statistical nature of the simulated velocity field is close to the observed one in this aspect.

4. Remarks

A previous paper (YT) shows the mesoscale eddies considerably enhance the basin-wide dispersion, especially in the vertical direction, and a small gap of the ridge cannot be an effective pathway. The present paper shows that timely intervention of the mesoscale eddies at the gap is of importance in determining the basin-wide trajectory of a particle.

Table 2. Maximum, minimum and average of residence time Re in the observed mesoscale eddy field, Ra in the average field and ratio Re/Ra. Both Re and Ra in days.

		May-Oct. 1983	July 1984-July 1985
Square(km^2)		35.4×35.4	70.0×70.0
Re	Max	16.0	41.0
	min	3.0	4.0
	mean	6.5	16.0
Ra		29.9	48.7
Re/Ra		0.22	0.33

As to the relationship between the residence time and the frame size, results of tracking experiments with the observed velocity data agree well with those calculated with the simulated velocity.

Circular frames might be more suitable for the calculation of the residence time than square frames when the point source is located at the center. The latters are, however, chosen for simplicity of calculation. The results will not change much if circular frames are set up.

A short experiment on streakiness was also attempted in the course of the present study for examining whether a spot of dye spreads into a cloud or into a number of streaks separated by clear water. In view of its importance in dispersion process, streakiness has been one of the recent topics (for example, HAIDVOGEL, 1982). No streaks were developed. However, further careful experiments are needed for understanding the behavior of an instantaneous release of dye in a mesoscale eddy field in terms of streakiness, which is of practical importance in ocean disposal of industrial wastes.

References

Atomic Energy Management Center (1985): Report of a preoperational survey of a proposed area for ocean disposal of radioactive wastes ——low-frequency water motion——. 270pp. (in Japanese)

HAIDVOGEL, D. (1982): On the feasibility of particle tracking in Eulerian ocean models. Ocean modelling, (45), 4–9. (unpublished manuscript)

IMAWAKI, S. and K.TAKANO (1982): Low-frequency eddy kinetic energy spectrum in the deep western North Pacific. Science, **216**, 1407–1408.

TAKANO, K. et S. MATSUYAMA (1979): Dispersion de polluants d'une source au fond porfond par des tourbillons â échelle intermédiaire. Radioécologie marine, Compte rendu du troisième Colloque de l'AEN, 117–127.

YOKOYAMA, K. and K.TAKANO (1993): Dispersion of passive tracers in an oceanic mesoscale eddy field. La mer, **31**, 59–78.

中規模うずを含む海での粒子の追跡

横山恵子・高野健三

要旨：中規模うずを含む流れの中の粒子を追跡する。流速は，4層の，うず分解循環モデルから与えられる。海は緯度方向には25.0°Nから50.5°Nまでひろがる。経度方向のひろがりは24.8°である。海の深さは，南北方向に走る海嶺（海底の高さは1900m）を除いて一定（4000m）であり，北西太平洋の一部に似た形になっている。うずを含む流速場と時間平均をとってうずを除いた流速場を使う。(i) 約30年にわたる追跡実験と，(ii) 数日から3年程度までの追跡実験，を行う。(i) では，平均流速を使うと，粒子の軌跡がまったく異なることがある。深層での動きに対して海嶺は大きな障壁となる。(ii) では，点源から一定の距離に達するまでの時間を，平均流速を使う場合とうずを含む流速を使う場合について求めて，その比を実測の流速データを用いた結果とくらべる。両者はよく一致する。

La mer 31: 91–101, 1993
Société franco-japonaise d'océanographie, Tokyo

Sedimentation processes in Tokyo Bay, Japan*

Tetsuo YANAGI** and Manabu SHIMIZU**

Abstract: Sedimentation patterns of riverine material in the surface sediment of Tokyo Bay have been classified into two groups, that is, fan shaped pattern such as pyrene, phosphorus, and copper and circular shaped pattern such as alkylbenzene, carbon and cadmium. Such two patterns are well reproduced by the three-dimensional numerical model experiment. Heavy and light particles are injected from three main rivers at the head of numerical model of Tokyo Bay which reproduces tidal current, residual current and density distribution of the prototype. Three-dimensional movements of injected particles due to currents, turbulence and sinking velocity are tracked by the Euler-Lagrange method including the judgment of settling of particles to the sea bottom by the critical tractive force theory. Heavy particles show the fan shaped sedimentation pattern and light particles the circular one. Calculated sedimentation patterns of riverine material are highly similar to the observed ones.

1. Introduction

It is well known that the sedimentation patterns of riverine material in surface sediment of Tokyo Bay are classified into two types. One is the fan shaped pattern in which the highest concentration is located at the mouth of rivers as shown in Fig. 1 (a). Pyrene, total phosphorus, copper, nickel and chromium take this pattern. Another is the circular shaped pattern in which the highest concentration is located at the central part of the bay as shown in Fig. 1 (b). LAS (Linear Alkyl-benzene Sulfonate), total carbon, biogenic silica, cadmium and zinc take this pattern (ISHIWA-TARI, 1988). ISHIWATARI (1988) pointed out the possibility that the riverine material which adheres to heavy particles takes the fan shaped pattern and that which adheres to light particles the circular shaped pattern.

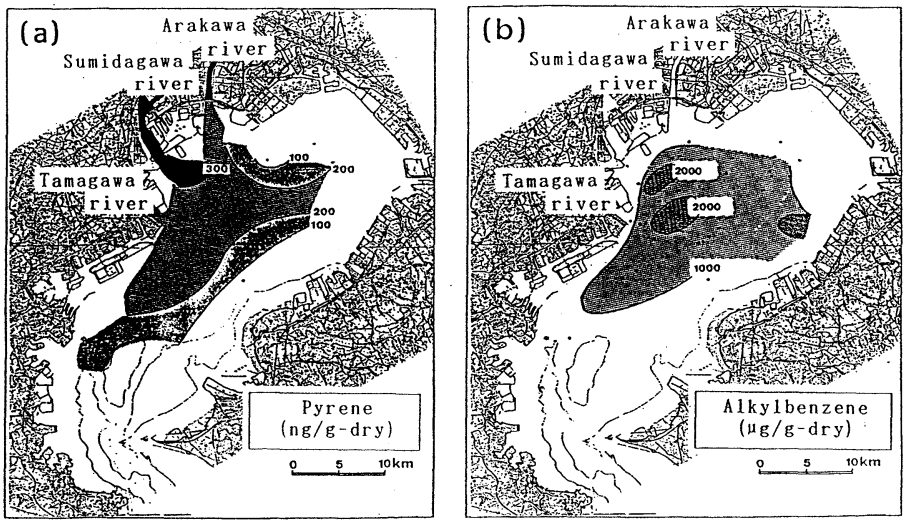

Fig. 1. Fan shaped (a) and circular shaped (b) sedimentation patterns in Tokyo bay (ISHIWATARI, 1988).

In this paper, we try to reproduce such two sedimentation patterns in Tokyo Bay with use

* Received March 19, 1993
** Department of Civil and Ocean Engineering, Ehime University Matsuyama, 790 Japan

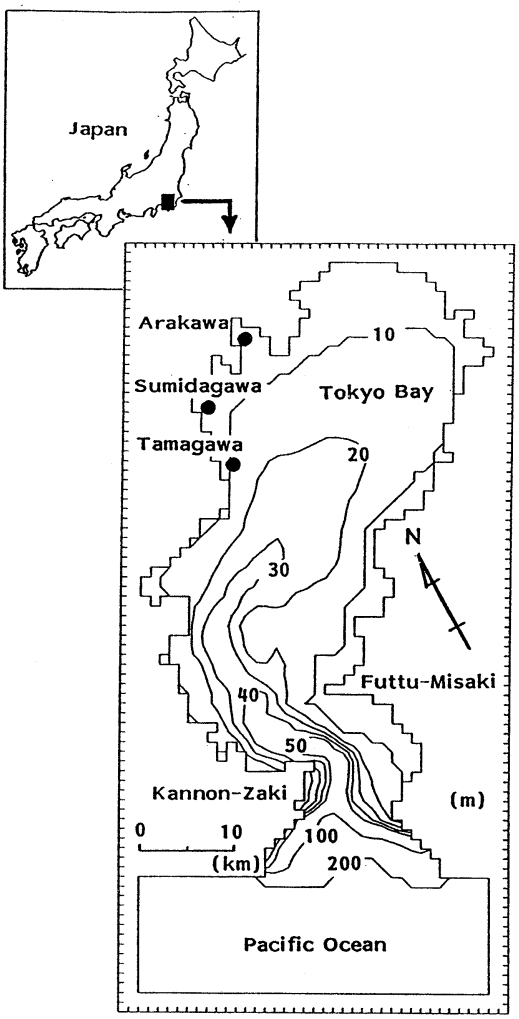

	SUMMER	WINTER
Layer 1	0 ~ 5	0 ~10
Layer 2	5 ~ 20	10 ~ 50
Layer 3	20 ~ 50	50 ~ Bottom
Layer 4	50 ~ Bottom	——

(m)

Fig. 2. Numerical model of Tokyo Bay. Full line denotes the bottom contour and the number the water depth in meter. Black circles de note the river mouths of three main rivers.

of three-dimensional numerical model by tracking the movements of heavy and light particles injected from the mouth of rivers.

2. Numerical experiment

2. 1 Currents and density fields

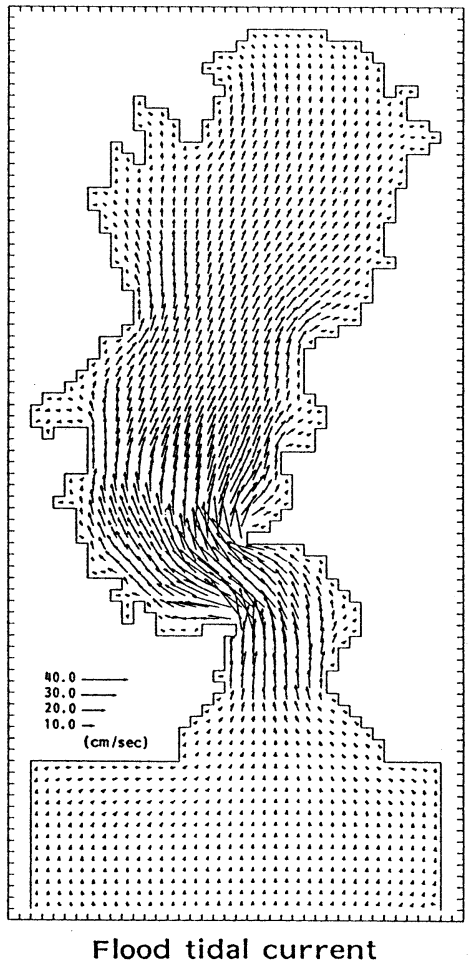

Fig. 3. Calculated maximum flood tidal current in Tokyo Bay.

The movement of riverine particless in Tokyo Bay is governed by currents, turbulence and the sinking velocity of particles. Then we first reproduce the currents of Tokyo Bay by the numerical model. Tokyo Bay is horizontally divided by the square mesh with 1 km length and the water column is vertically divided into four layers in summer and into three layers in winter as shown in Fig. 2.

The most dominant current in Tokyo Bay is the barotropic M_2 tidal current and it is well reproduced in this numerical model with use of usual method (YANAGI *et al.*, 1983). The reproduction of tide and tidal current is confirmed (YANAGI and SHIMIZU, 1991) and the calculated barotropic M_2 flood current is shown in Fig.3.

The maximum flood current of about 50 cm s^{-1} is appeared at the bay mouth and it is about 10 cm s^{-1} near the head of the bay. The ebb current flows in nearly the opposite direction with nearly the same speed. The horizontal forces due to tidal stress F_t (F_{tx}, F_{ty}) is caluculated with M_2 tidal current as follows;

$$F_{tx} = -\left(u\frac{\partial u}{\partial x} + v\frac{\partial u}{\partial y}\right)$$
$$F_{ty} = -\left(u\frac{\partial v}{\partial x} + u\frac{\partial v}{\partial x}\right) \quad (1)$$

where u and v denote the x and y component of M_2 tidal current, respectively, and overbar the average over one tidal cycle. F_t is used when we caluculate the residual flow.

Next we reproduce the residual flow in Tokyo Bay which governs the longterm transport of particles and the density distribution. The density distribution of sea water affects the sinking velocity and the tractive and resistance forces of particle as shown later. Here we try to reproduce residual flows and density distributions of Tokyo Bay in summer and in winter because they are two opposite typical seasons.

The basic equations are the momentum and continuity equations under the Bussinesq and hydrostatic approximations, the advection-dispersion equations of water temperature, salinity and density and the state equation as follows;

$$\frac{\partial V}{\partial t} + (V\cdot\nabla V) + f\mathrm{k}\times V = -\frac{1}{\rho_0}\nabla P + A_h\nabla^2 V + A_v\frac{\partial^2 V}{\partial z^2} + F_t$$
$$\frac{\partial w}{\partial z} = -\nabla V \quad (3)$$
$$P = \rho_0 g\eta + \rho_0\int_{-\eta}^{z} B\,dz \quad (4)$$
$$B = \frac{\rho_0 - \rho}{\rho_0}\,g \quad (5)$$
$$(\rho - 1.0)\times 10^3 = 28.14 - 0.0735T - 0.00469T^2 + (0.0802 - 0.002T)(S-35) \quad (6)$$
$$\frac{\partial T}{\partial t} + V\nabla\cdot T + w\frac{\partial T}{\partial z} = K_h\nabla^2 T + K_v\frac{\partial^2 T}{\partial z^2} \quad (7)$$
$$\frac{\partial S}{\partial t} + V\nabla\cdot S + w\frac{\partial S}{\partial z} = K_h\nabla^2 S + K_v\frac{\partial^2 S}{\partial z^2} \quad (8)$$

where V denotes the horizontal velocity; w, vertical velocity; , horizontal differntial operator; f ($=7.8\times10^{-5}s^{-1}$), Coriolis parameter; k, vertical unit vector; ρ, density; ρ_0, overall mean density; P the pressure; T, water temperature; S, salinity; A_h ($=10^6 cm^2 s^{-1}$) and A_v; horizontal and vertical eddy visosity, respectively; g ($=980 cm\ s^{-2}$), gravitational acceleration; η, sea level height above the mean sea surface; B, the buoyancy; K_h ($=10^6 cm^2 s^{-1}$) and K_v, horizontal and vertical eddy diffusivity, respectively.

Vertical eddy viscosity and vertical eddy diffusivity are parameterized as follows,

$$A_v = K_v = 1 - 10 cm^2 s^{-1} \quad (9)$$

A_v and K_v depends on the amplitude of M_2 tidal current and it is 10 $cm^2 s^{-1}$ at bay mouth where the tidal current is the strongest and 1 $cm^2\ s^{-1}$ at the head of the bay where the tidal current is the weakest.

The boundary conditions are given on the sea surface and at the sea bottom as :

$$\frac{\partial T}{\partial z} = \frac{g\alpha Q}{\rho_0 C_p},\ \frac{\partial S}{\partial z} = 0 \ at\ z=0 \quad (10)$$
$$\frac{\partial T}{\partial t} = \rho_0 C_d |V|V,\ \frac{\partial T}{\partial z} = \frac{\partial S}{\partial z} = 0 \ at\ z=-H \quad (11)$$

where α ($=2.0\times10^{-4}\ ^\circ C^{-1}$) denotes the heat expan-sion coefficient; Q, heat flux through the sea surface; C_p ($=0.932\ cal\ g^{-1}\ ^\circ C^{-1}$), specific heat under the constant pressure; C_d ($=2.6\times10^{-3}$), the drag coefficient at the sea bottom; and H, the water depth.

The salinity efflux from rivers S is given as follows,

$$\Delta S = -SR\frac{t}{hA} \quad (12)$$

where R denotes the river discharge; S, h and A, salinity, water depth and the area of the mesh which the river flows into, t (= 400sec) the time step of calculation. Δ S is subtracted from the calculated S at the mesh which the river flows into at every time step.

The non-slip condition of velocity is given

Table 1. Different parameters in summer and in winter.

	Summer	Winter
Surface heat flux (Q)	150W/m²	−100W/m²
Overall mean density (ρ_0)	1.0239g/cm³	1.0255g/cm³
Freashwater discharge (R)		
Edogawa river	180m³/sec	60m³/sec
Arakawa river	90m³/sec	30m³/sec
Tamagawa river	90m³/sec	30m³/sec

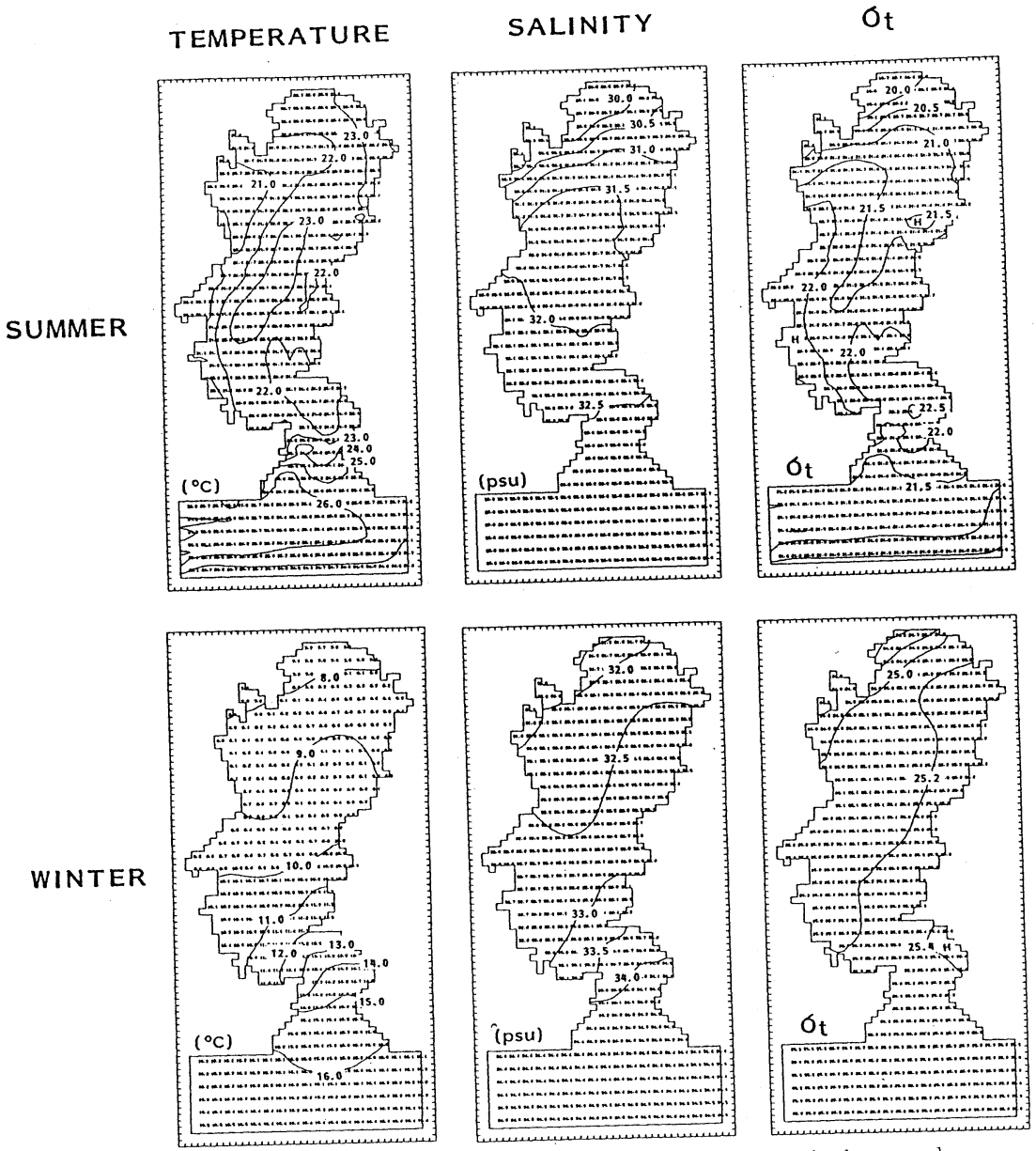

Fig. 4. Calculated water temperature, salinity and density distributions in the upper layer in summer (upper) and in winter (lower).

along the coast. The normal component of velocity to the open boundary is assumed to be zero. The horizontal gradients of water temperature and salinity across the open boundary are assumed to be zero.

Equations (1) to (12) are approximated by the finite difference and solved by the semi-implicit method (OONISHI, 1978). Different parameters in summer and winter are tabulated in Table 1.

The calculated water temperature, salinity and density distributions at the first layer in summer and in winter are shown in Fig.4. The observed water temperature, salinity and density distributions in summer and in winter (Hydrographic Office of Maritime Safety

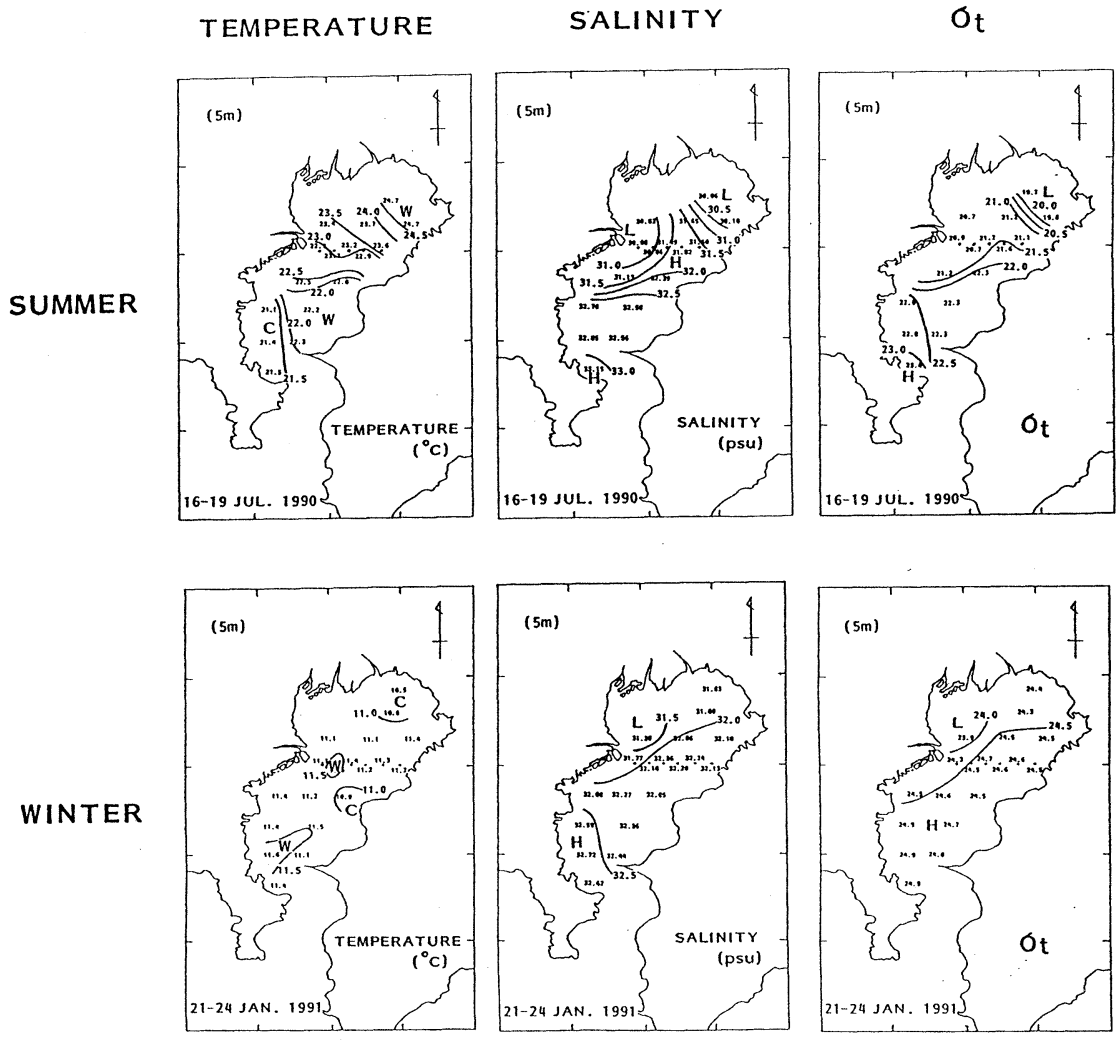

Fig. 5. Observed water temperature, salinity and density distributions in the upper layer in summer (upper) and in winter (lower).

Agency, 1991) are shown in Fig.5. The calculated distributions well reproduce the patterns of observed ones though the absolute values are a little different. The distribution patterns of water temperature, salinity and density in other layers (not shown) are also well reproduced by the numerical experiment.

The residual flows accompanied with calculated density distributions of Fig.4 are shown in Fig.6 (a) and (b). The clockwise residual circulation with the speed of about 10 cm s^{-1} is generated at the first layer in the central part of the bay in summer and the anticlockwise one with the speed of about 5 cm s^{-1} in winter. The residual circulation in the second layer is opposite to that in the first layer in summer but that is the same as the first layer in winter. There is no sufficient observational data on the distributions of residual flows of Tokyo Bay in summer and in winter. However, we may consider the residual flows in Fig.6 as reasonable ones because the distributions of water temperature and salinity are well reproduced as shown in Figs. (4) and (5).

The wind may affect the residual flow in Tokyo Bay but the wind is very variable with

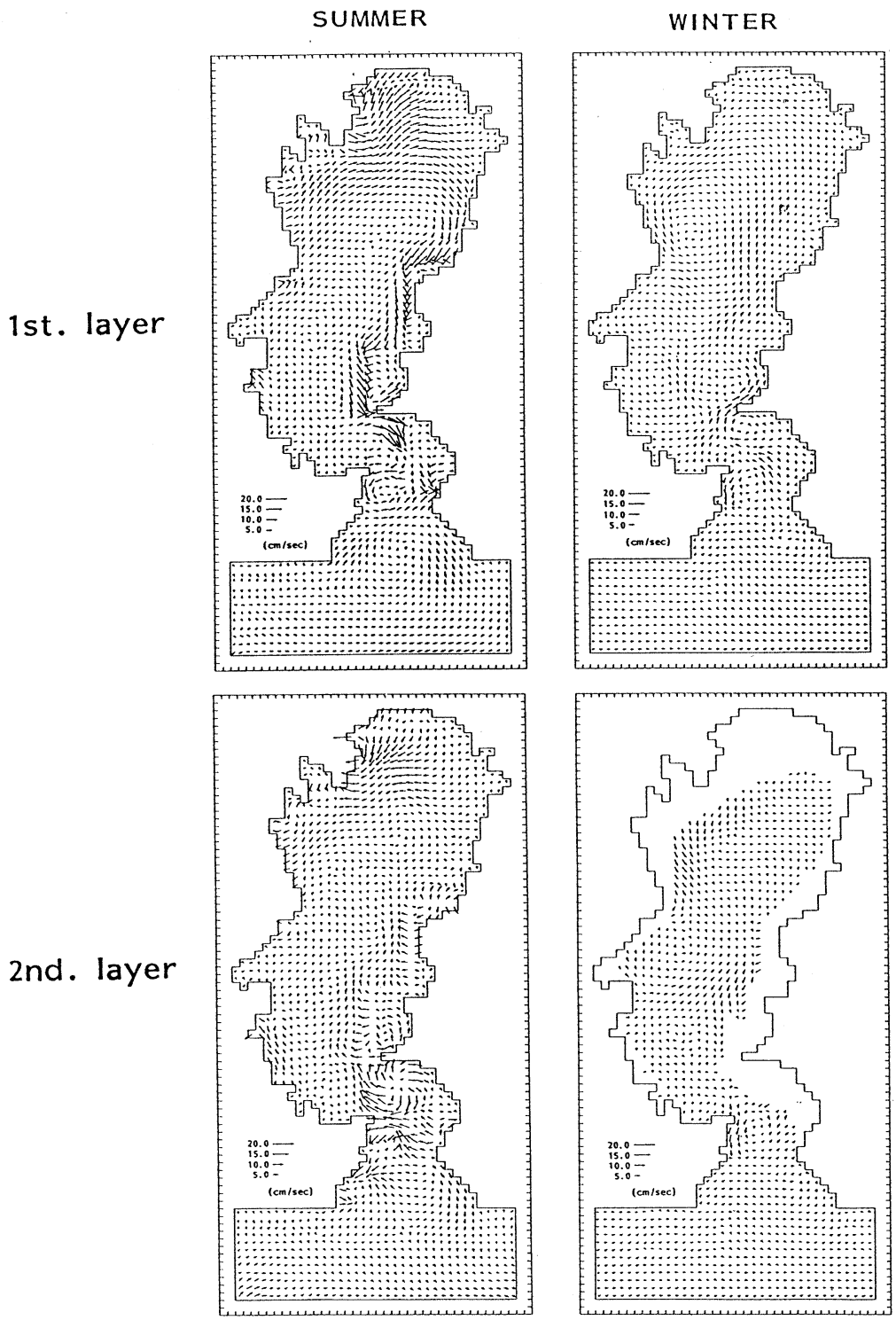

Fig. 6. Calculated residual flow in the upper (upper) and the middle (lower) layers in summer (left) and in winter (right).

the period of 3-4 days in summer and in winter. We carried out some numerical experiments with observed average wind in summer and in winter. However, we cannot reproduce the observed water temperature and salinity distributions under the constant wind blowing because the coastal upwelling is generated along the coast of Tokyo Bay by the northerly constant wind or southerly constant wind as discussed by MATSUYAMA *et al.* (1990). In the real field, the coastal upwelling phenomena are highly transient and are not steady state. We consider the time scale of 10-20 days in relation to the sedimentation process of particles in Tokyo Bay. Therefore, we take into account of only the tidal current and residual flow which consists of tide-induced residual current and density-driven current as the basic flow field in this numerical experiment of sedimentation in Tokyo Bay. The effect of wind to the movement of particles are included by the parameterization of wind into the wind wave in this numerical experiment which will be discussed later.

2.2 Sedimentation process

The Euler-Lagrange method is used to track the movement of particles in this numerical model. The position of particle X_{n+1} (x^{n+1}, y^{n+1}, z^{n+1}) at time n+1, which was X_n (x^n, y^n,z^n) at time n, can be calculated by the following equation:

$$X_{n+1}=X_n+v\Delta t+(\nabla v)v\Delta t^2+w_s\Delta t+R \quad (13)$$

where v denotes the calculated velocity vector including tidal current and residual flow; w_s, the sinking velocity of particle by the Stokes law ;

$$w_s = -\frac{g(\rho_p-\rho_w)}{18\mu r^2} \quad (14)$$

where g denotes the gravitational acceleration; ρ_p, density of particle; ρ_w, density of sea water; μ, ($=0.0115 cm^2 s^{-1}$), viscosity of sea water: r, diameter of particle. R is the dispersion due to the turbulence and is given by the following equation,

$$R_x \text{ and } R_y = \gamma\sqrt{2\Delta t D_h}, \qquad R_z = \gamma\sqrt{2\Delta t D_v} \quad (15)$$

where γ is the normal random number whose average is zero and whose standard deviation is 1.0; D_h ($=5 \times 10^5 cm^2 s^{-1}$) and D_v($=10 cm^2 s^{-1}$), the horizontal and vertical dispersion coefficient, respectively.

When particles reach the sea bottom, we judge whether it stops moving or removes by applying the critical tractive force theory (TSUBAKI, 1974):

$$F = \frac{\rho_w}{2} C_t U_b^2 \frac{\pi}{2} r^2 \quad (16)$$

$$R = \frac{\pi}{6} r^3 (\rho_p-\rho_w)\mu_s g \quad (17)$$

where F denotes the tractive force; R, the resistance force; C_t (= 0.4), drag coefficient of particle; μ_s (= 1.0), static friction coefficient of particle: U_b, the velocity just above the sea bed. We assume the velocity just above the sea bed is 0.2 times that of calculated velocity in the lowest layer of the numerical model and it is given by the following formula;

$$U_b = 0.2(U_t+U_r)+U_{wave} \quad (18)$$

where U_t denotes the calculated tidal velocity: U_r, calculated residual velocity and U_{wave} the water velocity due to wind wave and it is given by the following formula on the basis of small-amplitude wave theory;

$$U_{wave} = \frac{H_{wave} gT}{2L\cosh(2\pi H/L)} \quad (19)$$

where H denotes the water depth and H_{wave}, T and L wave height, wave period and wave length of dominant maximum wave in Tokyo Bay, respectively. The wave length depends on the water depth and the wave period and it is calculated as follows,

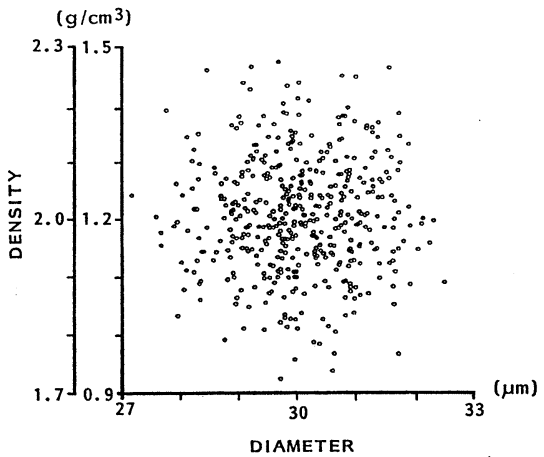

Fig. 7. Heavy and light groups of injected particles.

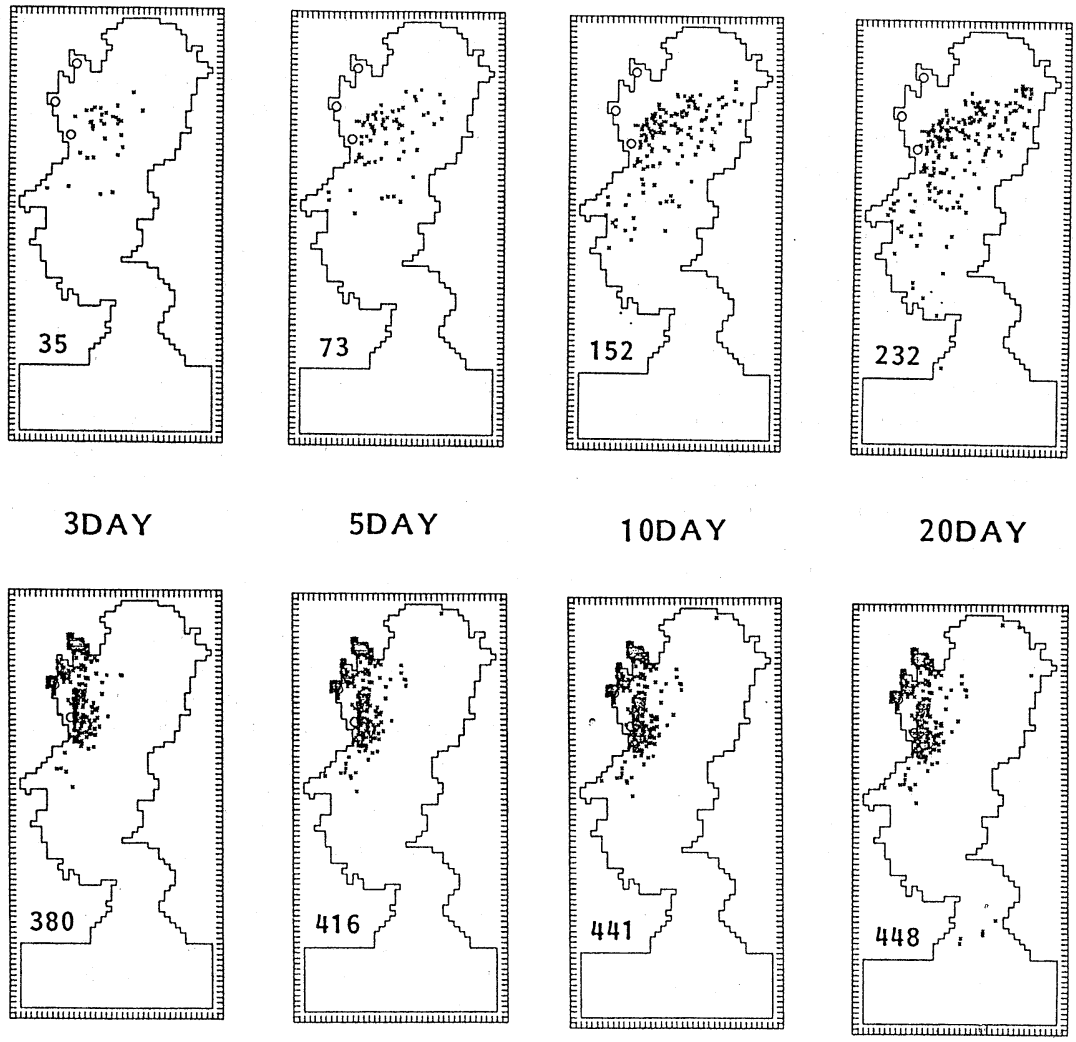

$$L = \frac{gT^2}{2\pi} \tanh \{2\pi (\frac{H}{gT^2})^{1/2} (1+(\frac{H}{gT^2})^{1/2}\} \quad (20)$$

The dominant wave height and wave period in Tokyo Bay were obtained by the field observation (Port Bureau of Tokyo Metropolitan, 1991). The used dominant maximum wave height and period in this numerical experiments are 80 cm and 3.0 sec, respectively and they are the same in summer and in winter. This is due to that the northerly wind is strong but the fetch is short in winter and the southerly wind is not so strong but the fetch is long in summer.

When R is larger than F, the particle stops moving and settles to the position where the particle reach the sea bottom and when F is larger than R, it removes from its position.

3. Results

Two groups of particles as shown in Fig.7 are injected from three river mouths which are

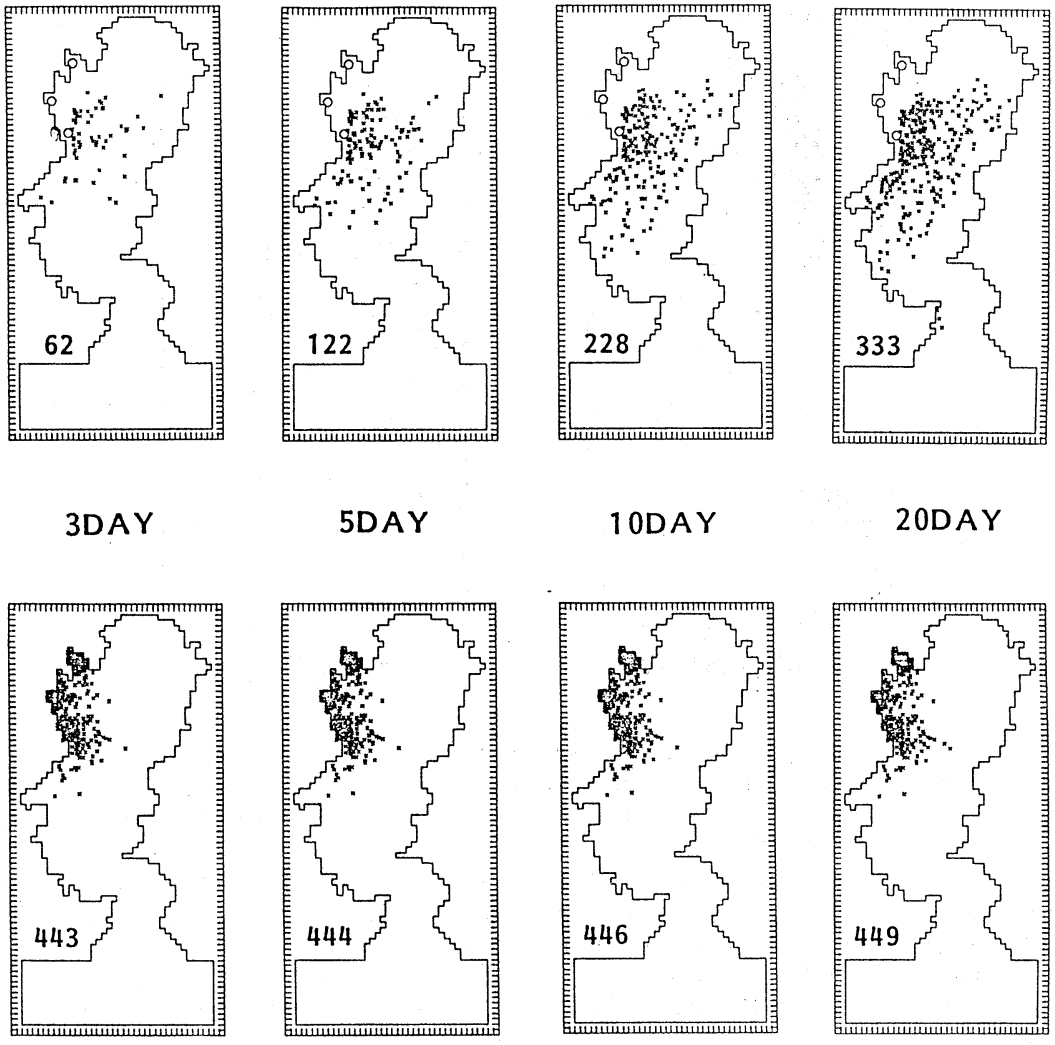

Fig. 8. Sedimentation patterns of light particles (upper) and heavy particles (lower) 3, 5, 10 and 20 days after the injection in summer (a) and in winter (b). Number means the number of settled particles.

shown in Fig.2. Heavy particles have the average diameter of 30 μm with the standard deviation of 1 μm and the average density of 2.0 g cm^{-3} with the standard deviation of 0.1 g cm^{-3} and light particles have the same average diameter and the average density of 1.2 g cm^{-3}. Such values are decided from the results of field observation in Tokyo Bay (R. ISHIWATARI, personal communication).

150 particles are injected from each river mouth and the total number of injected particles are 450. The results of numerical experiments are shown in Fig. 8 (a) and (b). Light particles settle in the central part of the bay while heavy particles settle near the river mouths in summer and in winter. Light particles can not settle near river mouth where the water depth is shallow and the current speed due to wind wave is large. On the oter hand, heavy particles can settle in the shallow part because the resistance

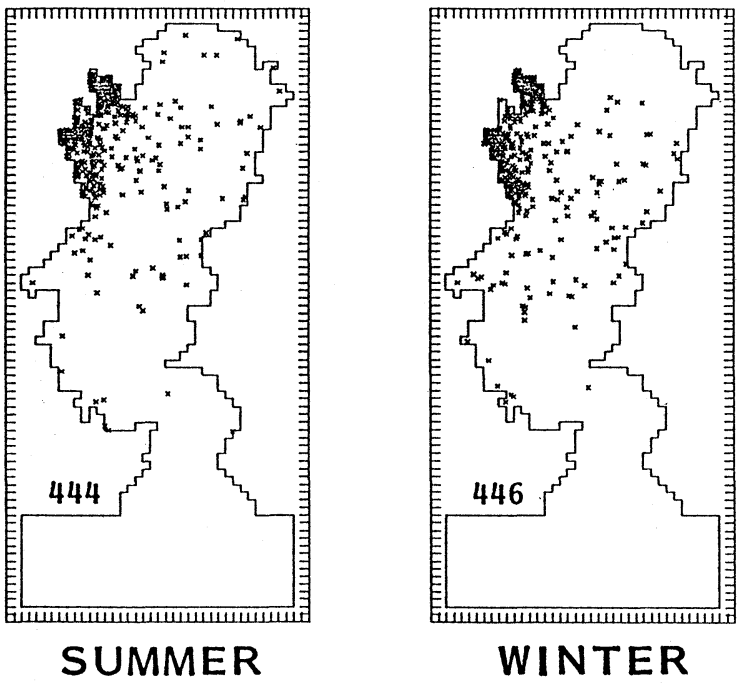

Fig. 9. Sedimentation patterns of light particles in the case of no wind wave 20 days after the injection in summer (left) and in winter (right). Number means the number of settled particles.

force R is large due to large particle density. The sedimentation pattern of light particles is simmilar to the circular shaped sedimentation pattern shown in Fig. 1 (b) and that of heavy particles to the fan shaped one shown in Fig. 1 (a).

The effect of wind wave is the largest in the difference of sedimentation patterns of light and heavy particles in Tokyo Bay because the velocities just above the sea bottom in Eq. (18) are $0.2 \times U_t \simeq 1.0$ cm s^{-1}, $0.2 \times U_r \simeq 0.4$–$1.0$ cm s^{-1} and $U_{wave} \simeq 2.0$ cm s^{-1} in the shallow part and $0.2 \times U_t \simeq 1.0$ cm s^{-1}, $0.2 \times U_r \simeq 0.4$-$1.0$ cm s^{-1} and $U_{wave} \simeq 0.02$ cm s^{-1} in the central part of the bay. The results of sedimentation pattern when the effect of wind wave is not included, are shown in Fig. 9. Light particles settle near the river mouth when the effect of wind wave is not included.

About half of light particles do not settle 20 days after the injection in summer while about 75 % settle in winter. The sinking velocity of particle shown in Eq. (14) and the resistance force shown in Eq. (17) are large and the tractive force is smaller in summer than in winter because the water density is smaller in summer. Such facts suggest that the settled number of particles is larger in summer than in winter while the calculated results show the oppositee results as shown in Fig. 8 (a) and (b). The difference of settled number of light particles 20 days after the injection between in summer and in winter is mainly due to the difference of speed of residual flow in summer and in winter because the speed of tidal current and that due to wind wave are the same in summer and in winter. The calculated speed of residual flow in the central part of the bay is 4–6 cm s^{-1} in summer and 2–3 cm s^{-1} in winter. The larger tractive force acts the particles in summmer than in winter and the settled number of light particles are smaller in summer than in winter.

4. Discussions

In these numerical experiments we change only the density of the particles without changing the diameter. We may obtain the same results if we change the diameter of particles without changing the density of particles because the sinking speed, tractive force and resistance force of particles depend on the density and diameter. Therefore we hope the chemical oceanographer to investigate the differences of average density or average diameter of particles to which riverine materials adhere in the near future.

In the real Tokyo Bay, particles may change its form from particulated state to dissolved state and vice verse. TAKEMATSU (1990) proposed another hypothesis that the fan shaped sedimentation is due to the inorganic particles and circular shaped one is due to the organic particles in Tokyo Bay. The rightness of his hypothesis has not been examined and we have to include such transformation of particles by the biochemical processes in the numerical model in the near future.

Acknowledgments

The authors express their sincere thanks to Dr. H. TAKEOKA of Ehime University, Prof. R. ISHIWATARI of Tokyo Metropolitan University and Dr. H. TAKADA of Tokyo University of Agriculture and Technology for their valuable discussions. A part of this study is defrayed by the Ministry of Education, Science and Culture, Japan.

References

Hydrographic Office of Maritime Safety Agency (1991): Observational results of water temperature and salinity in Tokyo Bay.

ISHIWATARI, R. (1988): Sedimentation process of land-derived organic matter in Tokyo Bay. Bulletin on Coastal Oceanography, **25**, 127–133 (in Japanese).

OONISHI, Y. (1978): Numerical simulation in the coastal sea. In "Science of Marine Enviroment" ed. by Y. Horible, Tokyo Univ. Press, Tokyo, 246–271 (in Japanese).

Port Bureau of Tokyo Metropolitan (1991): Wave Table in Tokyo Bay.

TAKEMATSU, N. (1988): Sedimentation pattern of riverine materials in the bay - concentric-fan-shaped sedimentation model. Bulletin on Coastal Oceanography, 25, 134–135 (in Japanese).

TSUBAKI, T. (1974): Hydraulics. Morikita Press, Tokyo, 210p. (in Japanese).

YANAGI, T., H. TSUKAMOTO, H. INOUE and T. OKAICHI (1983): Numerical simulation of drift cards dispersion. La mer, **21**, 218–224.

Y, T. and M. SHIMIZU (1991): Numerical experiment of sedimentation process in Tokyo Bay. Monthly Ocean, 23–4, 224–229 (in Japanese).

東京湾の堆積過程

柳　哲雄・清水　学

要旨：東京湾の表層堆積物の堆積パターンは，扇型パターンと円型パターンに大別される。前者はピレン・リン・銅などで，河口近傍に濃度最大域を有している。後者はアルキルベンゼン・炭素・カドニウムなどで，湾奥中央部に濃度最大域を有している。このような二つの堆積パターンが潮流・残渣流・密度分布・波浪による流れ・粒子の沈降速度を再現した3次元数値実験によりよく再現された。河川から流入した重い粒子は河口近傍ですみやかに堆積し，軽い粒子は河口近傍では堆積できず，流速の小さい湾奥中央部でのみ堆積する。したがって，重い粒子に吸着する諸物質は扇型パターンを，軽い粒子に吸着する諸物質は円型パターンを示すものと考えられる。

La mer 31: 103, 1993
Société franco-japonaise d'océanographie, Tokyo

学 会 記 事

1. 会員住所変更

畑　　幸彦　〒917 福井県小浜市学園町 1-1
福井県立大学生物資源学部

服部　　寛　〒005 札幌市南区南沢５条 1-1-1
北海道東海大学

福田　雅明　〒005 札幌市南区南沢５条 1-1-1
北海道東海大学

小林　和男　〒237 横須賀市夏島町 2-15
海洋科学技術センター

2. 受贈図書

Beitrage zur Meereskunde, Heft 63
Meeres wissenschaftliche Berichte, No. 4
Marine Science Reports, No. 4
水産学報, 16(4)
American Museum Novitates
Aquatic Living Resources, 5(4)
Israel Oceanographics & Limnological Research
日本学術会議月報, Vol. 34
広島日仏協会報, No. 120
なつしま, No. 123
NTT R & D, 42(3,4)
国立科学博物館研究報告, 18(4)
国立科学博物館専報, No. 25
東海大学紀要（海洋学部創設30周年記念号）
RESTEC, No. 30
海洋産業研究資料, 24(4,5)
日本航海学会誌, No. 115
日本航海学会論文集, No. 88
東海大学海洋学部業績集, No. 22
神戸海洋気象台報, No. 212
しおさい, No. 9
農業工学研究所年報, No. 4

日仏海洋学会役員・評議員

（1992-1993 年度）

顧　　問：ユーベル・ブロシェ　ジャン・デルサルト　ジャック・ローベル　アレクシス・ドランデール　ベルナール・フランク　ミシェル・ルサージュ　ローベル・ゲルムール　ジャック・マゴー　レオン・ヴァンデルメルシュ　オーギュスタン・ベルク　ユーベル・セカルディ
名誉会長：オリビエ・アンサール
会　　長：有賀祐勝
副 会 長：高木和徳　岡市友利
幹　　事：（庶務）　須藤英雄　有元貴文
（会計）　松生　洽　森永　勤
（研究）　関　文威　小池勲夫
（編集）　山口征矢　渡邊精一
監　　事：久保田穣　辻田時美
編集委員長：村野正昭
評 議 員：
青山恒雄　有賀祐勝　有元貴文　石井丈夫
石野　誠　石丸　隆　今脇資郎　宇野　寛
大塚一志　岡市友利　梶浦欣二郎　金成誠一
鎌谷明善　国司秀明　黒田一紀　小池勲夫
佐伯和昭　坂本市太郎　坂本　亘　杉森康宏
須藤英雄　関　文威　関根義彦　平　啓介
高木和徳　隆島史夫　高野健三　高橋正征
竹松　伸　谷口　旭　辻田時美　寺崎　誠
寺本俊彦　鳥羽良明　永田　豊　奈須敬二
西沢　敏　畑　幸彦　平野敏行　堀越増興
前田明夫　松生　洽　松村皐月　松山優治
丸茂隆三　村野正昭　森永　勤　柳　哲雄
山口征矢　和田　明　渡邊精一

平成５年度学会賞受賞候補者推薦委員会委員

青木三郎　阿部友三郎　石野　誠　今脇資郎
落合正宏　鎌谷明善　小池勲夫　高野健三
竹松　伸　谷口　旭　中村重久　松生　洽
村野正昭　柳　哲雄　山口征矢

日本学術会議だより No.28

「アジア学術会議(仮称)」の開催決まる

平成5年3月 日本学術会議広報委員会

「アジア学術会議(仮称)」の開催経費を含む日本学術会議の平成5年度予算が決まりましたので，その概要についてお知らせします。

平成5年度日本学術会議予算

日本学術会議の第15期活動計画の大きな柱である「学術研究の国際貢献の重視」の具体的方策の一環として，「アジア学術会議(仮称)」の開催が，平成5年度予算によって実現することとなりました。その内容は，学術研究が環境問題等の諸課題を克服し，人類の繁栄と世界の平和に寄与するとの認識に立って，本年秋に東京で，我が国と地理的・文化的に関係の深いアジア各国を代表する学術研究者が一堂に会して，各国における学術研究の現状，アジア地域における連携・協力のあり方などに関し意見を交換する場として開催するものです。我が国を含め10か国程度のアジア諸国から，代表者を招へいする予定です。

その他，平成5年度予算では，国際分担金の25団体に対する単価アップが認められ，国際会議の国内開催費については，アジア社会科学，植物科学，太平洋学術，電波科学，純粋・応用物理学，気象・水分，の6国際会議の開催を予定しています。また、世界各地で開催される学術関係国際会議への代表派遣や二国間交流に必要な経費が計上されております。

平成5年度予算概算決定額表は，下記のとおりであります。

(単位：千円)

事項	前年度予算額 A	平成5年度予算額 B	比較増△減額 C＝B－A	備考
日本学術会議の運営に必要な経費	1,042,482	1,095,827	53,345	対前年度比較 105.1%
審議関係費	248,789	265,525	16,736	○地球圏－生物圏国際協同研究計画(IGBP)シンポジウム，公開講演会等
国際学術交流関係費	198,514	221,254	22,740	
国際分担金	67,089	74,722	7,633	
国内開催	80,596	73,543	△ 7,053	
代表派遣	44,006	44,006	0	
二国間交流	6,823	6,823	0	
アジア学術会議	－	22,160	22,160	
会員推薦関係費	21,216	19,574	△ 1,642	
一般事務処理費	573,963	589,474	15,511	

日本学術会議第16期会員の推薦について

日本学術会議の会員は，従来，科学者を有権者とする直接選挙によって選出されていましたが，日本学術会議法の一部を改正する法律（昭和58年法律65号）により，第13期（昭和60年７月22日）から、学術研究団体を基盤とする推薦・任命制に改められました。来年７月で，この推薦制度も三期９年を経過することとなります。

この会員選出制度のあらましは，次のとおりです。

① 日本学術会議は，一定の要件を備える学術研究団体を，その申請により登録する。

② 登録学術研究団体は，その構成員である科学者のうちから，会員の候補者を選定し，及び会員の推薦に当たる推薦人を指名し，それぞれ，日本学術会議に届け出る。

③ 推薦人は，会員推薦管理会がその資格があると認定した会員の候補者のうちから，会員として推薦すべき者及び補欠の会員として推薦すべき者を決定し，日本学術会議を経由して内閣総理大臣に推薦する。

④ 内閣総理大臣は，上記③の推薦に基づいて，会員を任命する。

⑤ 学術研究団体の登録，会員の候補者の資格の認定その他会員の推薦に関する所要の事務は，日本学術会議に置かれる会員推薦管理会が行う。

以上の概要を第16期（平成６年７月－平成９年７月）の会員選出日程によると，次表のようになり，これに従って今後の事務処理が行われる予定になっています。

日本学術会議第16期会員選出手続日程

平成5年	5月31日(月)まで	学術研究団体の登録申請の締切り
	9月上旬	登録審査結果の通知
	不登録通知を受けた日の翌日から20日以内	不登録通知を受けた団体からの異議の申出受付
	9月上旬	関連研究連絡委員会についての意見聴取*
	10月下旬	〈団体関係〉異議の申出に対する決定
	11月30日(火)まで	関連研究連絡委員会の指定*
	12月上旬	会員の候補者の選定及び推薦人の指名の依頼
平成6年	1月31日(月)まで	会員の候補者の届出の締切り
	2月21日(月)まで	推薦人（予備者を含む）の届出の締切り
	3月20日(日)まで	会員の候補者の資格の認定等の通知
	3月下旬	推薦人に会議開催等の通知発送
	不認定通知を受けた日の翌日から20日以内	会員の候補者の資格の不認定通知を受けた学術研究団体又は会員の候補者からの異議の申出受付
	4月20日(水)まで	〈会員の候補者関係〉異議の申出に対する決定
	5月中旬から6月上旬まで	推薦人会議（会員及び補欠の会員として推薦すべき者を決定）
	6月中旬	日本学術会議を経由して内閣総理大臣へ推薦
	7月22日(金)	第16期日本学術会議会員の任命

注：＊は，日本学術会議会長が意見聴取し，指定する。

日学双書の刊行について

日本学術会議主催公開講演会及び公開シンポジウムの記録をもとに編集した，次の日学双書が刊行されました。

日学双書第15刊 「文明の選択－都市と農業・農村の共存を目指して－」
定価1,000円（消費税込み，送料240円）

日学双書第16刊 「子どもの人権を考える」
定価1,000円（消費税込み，送料240円）

日学双書第17刊 「首都機能の一極集中問題」
定価2,000円（消費税込み，送料310円）

（問い合わせ先）
〒106 東京都港区西麻布3-24-20
交通安全教育センター内
㈶日本学術協力財団
☎03-3403-9788

御意見・お問い合わせ等がありましたら，下記までお寄せください。
〒106 東京都港区六本木７-22-34
日本学術会議広報委員会 電話03(3403)6291

賛　助　会　員

旭化成工業株式会社	東京都千代田区有楽町 1-1-2　三井ビル
株式会社旭潜研	東京都北区栄町 9-2
阿部嘉方	東京都練馬区春日町 2-15-6
株式会社内田老鶴圃 内田悟	東京都文京区大塚 3-34-3
有限会社英和出版印刷社	東京都北区中里 2-7-7
株式会社カイジョウ	東京都西多摩郡羽村町栄町 3-1-5
(財)海洋生物環境研究所	東京都千代田区内神田 1-18-12　北原ビル内
株式会社川合海苔店	東京都大田区大森本町 2-31-8
三信船舶電具株式会社	東京都千代田区神田 1-16-8
株式会社 自然・情報環境研究所	横浜市栄区桂町 1-1, 3-401
昭和電装株式会社	高松市寺井町 1079
新日本気象海洋株式会社	東京都世田谷区玉川 3-14-5
全日本爬虫類皮革産業連合会	東京都足立区梅田 4-3-18
株式会社高岡屋	東京都台東区上野 6-7-22
株式会社鶴見精機	横浜市鶴見区鶴見中央 2-2-20
株式会社東京久栄技術センター	埼玉県川口市芝鶴ケ丸 6906-10
株式会社 東急フーズミート	東京都品川区東品川 4-10-21
株式会社西日本流体技研	長崎県佐世保市棚方町 283
日本アクアラング株式会社	神奈川県厚木市温水 2229-4
株式会社 日立造船技術研究所 バイオ研究センター	大阪市此花区桜島1-3-22
宮本悟	東京都中央区かきどき 3-3-5　かちどきビル　㈱本地郷
株式会社読売広告社	東京都中央区銀座 1-8-14
渡辺機開工業株式会社	愛知県渥美郡田原町神戸大坪 230
株式会社渡部計器製作所	東京都文京区向丘 1-7-17

応援します。
良い海苔づくり—

生海苔活性調整機

RS-2型

海苔の等級が数段あがる

※生海苔を活性化し、海苔製品の表面をなめらかに光沢よく仕上げます。

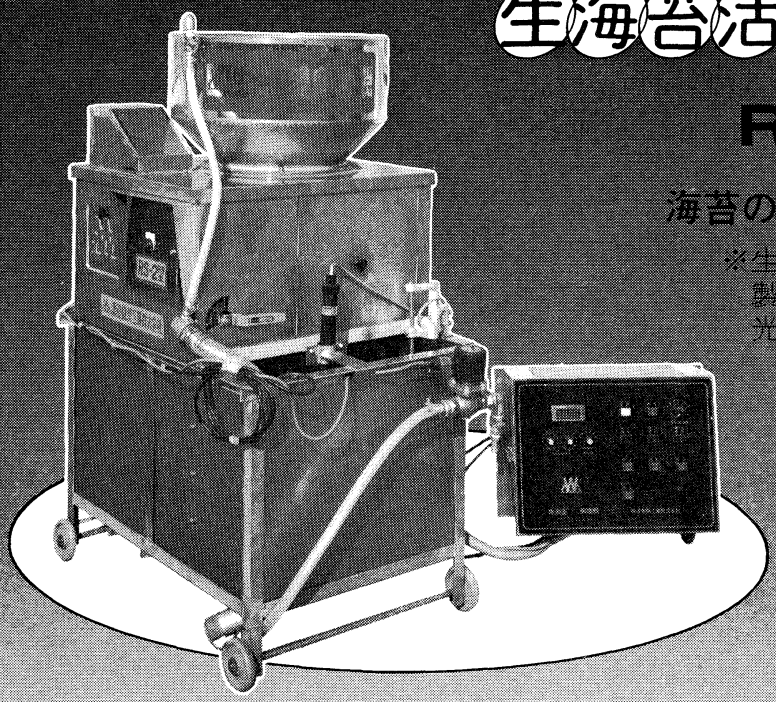

	RS-1型	RS-2型
高さ	770㎜	1,280㎜
幅	995㎜	990㎜
横	680㎜	780㎜
重量	65kg	160kg
モートル	40W 1台 100W 1台	40W 2台 60W 1台 100W 1台 150W 1台

渡辺機開工業株式会社
愛知県渥美郡田原町神戸大坪２３０
電話　０５３１２（２）１１２１（代　表）

投稿の手引

1. 「うみ」(日仏海洋学会機関誌; 欧文誌名 La mer) は，日仏海洋学会正会員およびそれに準ずる非会員からの投稿 (依頼稿を含む) を，委員会の審査により掲載する。
2. 原稿は海洋学および水産学両分野の原著論文，原著短報，総説，書評，資料などとする。すべての投稿は，本文，原図とも正副2通とする。副本は複写でよい。本文原稿用紙はすべてA4判とし，400字詰原稿用紙 (和文) に，または厚手白紙にダブル・スペース (和文ワープロでは相当間隔) で記入する。表原稿および図説明原稿は，それぞれ本文原稿とは別紙とする。
3. 用語は日，仏，英3カ国語の何れかとする。ただし，表および図説明の用語は仏文または英文に限る。原著論文 (前項) には約200語の英文または仏文の要旨を，別紙として必ず添える。なお，欧文論文には，上記要旨の外に，約500字の和文要旨をも添える。ただし，日本語圏外からの投稿の和文要旨については編集委員会の責任とする。
4. 投稿原稿の体裁形式は最近号掲載記事のそれに従う。著者名は略記しない。記号略号の表記は委員会の基準に従う。引用文献の提示形式は，雑誌論文，単行本分載論文(単行本の一部引用を含む)，単行本などの別による基準に従う。
5. 原図は版下用として鮮明で，縮尺 (版幅または1/2版幅) に耐えられるものとする。
6. 初校に限り著者の校正を受ける。
7. 正会員に対しては7印刷ページまでの掲載を無料とする。ただし，この範囲内であっても色彩印刷を含む場合などには，別に所定の費用を著者負担とすることがある。正会員の投稿で上記限度を超える分および非会員投稿の印刷実費はすべて著者負担 (10,000円/頁) とする。
8. すべての投稿記事について，1篇あたり別刷50部を無料で請求できる。50部を超える分は請求により，50部単位で作製される。別刷請求用紙は初校と同時に配布される。
9. 原稿の送り先は下記の通り。

〒108 東京都港区港南4-5-7 東京水産大学　村野正昭 気付
日仏海洋学会編集委員会

1993年5月25日 印刷
1993年5月28日 発行

うみ　第31巻 第2号

定価 ¥1,600

編集者　村野正昭
発行所　日仏海洋学会
財団法人 日仏会館内
東京都千代田区神田駿河台2-3
郵便番号：101
電話：03(3291)1141
振替番号：東京 5-96503
印刷者　佐藤一二
印刷所　有限会社英和出版印刷社
東京都北区中里2—7—7
郵便番号：114
電話：03(5394)4856

(本誌出版費の一部は平成5年度文部省科学研究費補助金「研究成果公開促進費」による.)
Publication of La mer has been supported in part by a Grant-in-Aid for Publication of Scietific Research Result from the Ministry of Education, Science and Culture, Japan.

Tome 31 N° 2

SOMMAIRE

第 31 巻 第 2 号

目 次